

Proton and Antiproton Production
in High Energy Heavy Ion Collisions at RHIC

Masahiro KONNO
(Doctoral Program in Physics)

Submitted to the Graduate School of
Pure and Applied Sciences
in Partial Fulfillment of the Requirements
for the Degree of Doctor of Philosophy in
Science

at the
University of Tsukuba

Abstract

Relativistic heavy ion collisions is a means to approach Quark-Gluon Plasma (QGP) state which is composed of deconfined and freely moving quarks and gluons. Currently, generating and exploring the QGP state is underway at Relativistic Heavy Ion Collider (RHIC) at Brookhaven National Laboratory. The PHENIX experiment is one of the experiments at RHIC.

Particle production in relativistic heavy ion collisions is a basic and important topic for both understanding the collision dynamics and search for the QGP state. It is usually divided into two parts in transverse momentum - soft and hard particle productions. Soft part ($p_T \lesssim 2$ GeV/c) means particle emission from a thermal source with collective flow, hard part ($p_T \gtrsim 2$ GeV/c) means hard scattering followed by jet fragmentation.

One of the remarkable findings at RHIC is particle-type dependences of hadron yields and emission patterns, especially its difference between baryons and mesons, at intermediate p_T (2-5 GeV/c). In central $\sqrt{s_{NN}} = 200$ GeV Au+Au collisions, there is a significant suppression in meson yields compared to expectations from peripheral Au+Au and scaled p+p results. In contrast, a large enhancement of baryons relative to mesons was observed at intermediate p_T . Moreover, in elliptic flow measurements, a baryon-meson difference was also found in its magnitude. This difference between baryons and mesons are explained by hydrodynamic flow, quark recombination models, and so on. Multiple mechanisms are thought to be involved for intermediate- p_T hadron production. However we do not know the exact relative contributions of those mechanisms at the moment.

The purpose of this thesis is to study hadron production mechanisms at intermediate p_T and final-state interactions between hadrons produced in relativistic heavy ion collisions. We have performed a systematic study of proton and antiproton spectra in Au+Au/Cu+Cu/p+p collisions at $\sqrt{s_{NN}} = 200/62.4$ GeV. The data set taken in the PHENIX experiment allows us to study the energy dependence and system size dependence of the baryon enhancement. The spectra have been measured at mid-rapidity ($|\eta| < 0.35$) over the range of $0.5 < p_T < 6$ GeV/c with particle identification by time-of-flight and threshold-type Cherenkov light emission methods. The p_T range of charged hadron identification has been extended by the high statistics data. Also the particle identification capability at high p_T has been enhanced by introducing an Aerogel Cherenkov counter in PHENIX. The identified hadron production can be studied up to 5 GeV/c for charged pions, and 7 GeV/c for (anti)protons. In this thesis, we present identified charged hadron p_T spectra ($\pi/K/p$ and their antiparticles), particle ratios, nuclear modification factors, chemical/kinetic freeze-out properties and their scaling properties between different collision systems.

In all collision systems (Au+Au, Cu+Cu), we confirm the baryon enhancement at intermediate p_T . We find that the baryon enhancement and freeze-out properties (kinetic freeze-out temperature, transverse flow velocity) can be scaled with the number of participant nucleons, which is corresponding to the system volume, between Au+Au and Cu+Cu collisions at the same collision energy $\sqrt{s_{NN}} = 200/62.4$ GeV even though the overlap region has a different shape. At lower energy 62.4 GeV, proton production seems to be more affected by baryon number transport process. Therefore antiproton would be a good indicator of the baryon enhancement.

Using a simple two-component model including soft (thermal emission with collective radial flow) and hard (jet fragmentation with quenching effect) hadron components, we can reproduce the measured p_T spectra, and identify crossover region from soft to hard hadron productions at intermediate p_T . We estimate the relative fraction of soft and hard components - soft and hard components become of equal size in this p_T region (2-4 GeV/c). The crossing point depends on collision centrality. It is shifted to higher p_T in more central collisions due to radial flow effect. Radial flow effect is significant in central Au+Au collisions compared to smaller systems. This effect pushes heavier particles like protons to higher p_T . We think that the baryon enhancement at intermediate p_T can be attributed to radial flow effect. We also discuss the relation between this radial flow picture and quark recombination picture. In a simple recombination picture, they are not inconsistent. The difference of chemical and kinetic freeze-out temperatures provides a hint for the duration time of hadronic stage.

At high $p_T \gtrsim 5$ GeV/c, p/π (\bar{p}/π) ratios in central Au+Au collisions approach the values in p+p collisions. And R_{CP} shows similar suppression for pions and (anti)protons, though they have different sensitivities to quark and gluon jets. The results indicate that hard-scattered partons (quarks and gluons) have similar energy loss when traversing the nuclear medium, and parton fragmentation function does not change.

Acknowledgments

I first would like to express my great gratitude to Prof. Y. Miake for his appropriate advices and continuous encouragement. I learned a lot of things from him in many aspects. I would like to thank Prof. S. Esumi for valuable advices and discussions. I am always taught from his many-sided ways of thinking, and of course his toughness. I would like to thank Prof. T. Chujo for many advices especially on data analysis. His elaborateness and constant work to anything is example for me.

I would like to express my warm appreciation to all the present and past members of the high energy nuclear physics group at University of Tsukuba. I would like to thank Prof. M. Inaba, Mr. S. Kato for their helps. I wish to express my thanks to Dr. S. Sato, Dr. A. Kiyomichi for many useful advices in life at Tsukuba and BNL. I would like to thank Dr. H. Masui, Dr. S. Sakai, Ms. M. Shimomura, Mr. S. Takagi, Mr. S. Kaminaga for their help, friendship and discussions. I also acknowledge Mr. Y. Nagata, Mr. M. Oka, Mr. K. Miki, Mr. Y. Ikeda, Mr. R. Tanabe and many other colleagues for their friendship.

I would like to express my thanks to all the members of the PHENIX collaboration for many useful advices and helps in detector work and data analysis. I wish to express my thanks to Dr. A. Enokizono, Prof. V. Greene, Dr. K. Homma, Dr. A. Taranenko (the Global-Hadron physics group convenors), Dr. E. Kistenev, Prof. R. Lacey, and many other people for their kind encouragement and many useful advices.

I acknowledge for all the members of the PHENIX-J for their friendship and valuable discussions during my stay at BNL. I would like to thank Prof. H. Hamagaki and Prof. K. Ozawa for their arrangement and support during stays at BNL.

Finally, I would like to express my great appreciation to my parents and brothers Masanori, Mikie, Hideki, and Tatsuya for their support and encouragement. I could never finish my thesis without their great help and understanding.

Contents

1	Introduction	1
1.1	Quantum Chromodynamics	1
1.2	Quark Gluon Plasma	3
1.3	Relativistic Heavy-Ion Collisions	3
1.3.1	p+p, p(d)+A, A+A Collisions	3
1.3.2	Collision Dynamics	4
1.3.3	RHIC Findings	7
1.3.4	Hadron Production at Intermediate p_T	11
1.4	Thesis Motivation	12
2	Experimental Setup	14
2.1	Relativistic Heavy-Ion Collider	14
2.2	PHENIX Detector Overview	16
2.3	Global Detectors	19
2.3.1	Beam Beam Counters (BBC)	19
2.3.2	Zero Degree Calorimeters (ZDC)	20
2.4	Central Arm Spectrometers	21
2.4.1	Central Arm Magnet	22
2.4.2	Drift Chambers (DC)	23
2.4.3	Pad Chambers (PC)	24
2.4.4	Electromagnetic Calorimeters (EMCal)	25
2.4.5	Time of Flight Detector (TOF)	26
2.4.6	Aerogel Cherenkov Counter (ACC)	27
3	Data Analysis	29
3.1	Event Selection	29
3.1.1	Data Sets	29
3.1.2	Minimum Bias Trigger and Efficiency	29
3.1.3	Centrality Determination	30
3.1.4	Participant-Spectator Model and Glauber Model	31

3.2	Charged Particle Measurement	35
3.2.1	Track Reconstruction	35
3.2.2	Track Association and Selection	35
3.3	Event and Track Selection Cuts	38
3.4	Quarility Assurance - run-by-run stability check	39
3.5	Particle Identification	39
3.5.1	Time of Flight Counter	39
3.5.2	Aerogel Cherenkov Counter	42
3.5.3	Particle Contamination	44
3.6	Background Subtraction	49
3.7	Fiducial Cut	52
3.8	Monte Carlo Correciton	54
3.8.1	Spectra Correction	54
3.8.2	Multiplicity-dependent Efficiency Correction	54
3.9	Invariant Cross Section	56
3.10	Weak Decay Feed-down	56
3.11	Systemtaitec Uncertainties	57
4	Results	61
4.1	Transverse Momentum Spectra	62
4.1.1	p_T spectra (ACC) – Au+Au 200 GeV	62
4.1.2	p_T spectra (TOF) – Au+Au 200 GeV	63
4.1.3	p_T spectra (ACC) – Cu+Cu 200 GeV	64
4.1.4	p_T spectra (TOF) – Cu+Cu 200 GeV	65
4.1.5	p_T spectra (TOF) – p+p 200/62.4 GeV	67
4.2	Mean Transverse Momentum	69
4.3	Particle Yield at Mid Rapidity	70
4.4	Particle Ratios	71
4.4.1	p/π ratios vs. p_T	71
4.4.2	p/π ratios vs. N_{part}	72
4.4.3	\bar{p}/p ratio vs. p_T	75
4.5	Nuclear Modification Factors	77
4.5.1	R_{AA}	77
4.5.2	R_{CP}	80
5	Discussions	84
5.1	Freeze-out Properties	84
5.1.1	Chemical Freeze-out – Statistical Model Fit	85

5.1.2	Kinetic Freeze-out – Blast-wave Model Fit	88
5.2	Hadron Production at Intermediate p_T	97
5.2.1	Proton and Antiproton Enhancement	97
5.2.2	Two-component Model	101
	Decomposition of p_T Spectra	101
	Fraction of Soft/Hard Components	106
	Soft/Hard Separation in Particle Ratios	109
	Soft/Hard Separation in Particle Yield	111
	Soft/Hard Separation in Elliptic Flow	112
	Summary of Two-component Model	114
5.2.3	Quark Recombination Picture	114
5.2.4	Jet Fragmentation and Jet Quenching	116
6	Conclusions	120
A	Kinematic Variables	122

Chapter 1

Introduction

In this chapter, the current relativistic heavy-ion physics is reviewed with major findings at RHIC. The motivation of this thesis is given.

1.1 Quantum Chromodynamics

In our current understanding, the fundamental elements of hadrons are quarks and gluons. They interact with each other via strong force which is described in Quantum Chromodynamics (QCD). And we know that quarks are confined inside a hadron. The question is: “Quarks can exist as an apparent degree of freedom?” Lattice QCD calculations predict a phase transition from hadronic matter to a deconfined state at high temperature and high energy density, in which quarks and gluons are freely moving over a large volume. This state is called Quark-Gluon Plasma (QGP). Many static properties of the high-temperature phase of QCD matter have been studied in detail by means of lattice calculations [1]. Among these are the equation of state (i.e. energy density $\epsilon(T)$ and pressure $p(T)$), quantities related to color confinement such as the potential $V_{q\bar{q}}(r)$ between a pair of heavy quarks, and quantities related to chiral symmetry breaking. The results of QCD calculations confirm that a dramatic rearrangement of the internal structure of hadronic matter occurs near critical temperature T_c , which is consistent with the idea that open-color states are free above T_c and chiral symmetry is restored, except for the small current masses of light quarks, which are not of QCD origin. Figure 1.1 shows a QCD-phase boundary that was obtained by Lattice QCD Monte Carlo calculations [2, 3]. The dashed line represents the lattice gauge theory results to larger values of chemical potential. Within uncertainties, the energy density along this line is constant and corresponds to $\epsilon_c \sim 0.6 \text{ GeV fm}^{-3}$, i.e. to the same value as that found from lattice calculations at $\mu_B = 0$. It is said that the QCD phase transition indeed sets in when the energy density reaches a certain critical value. Figure 1.1 also shows a compilation of chemical freeze-out parameters, extracted from experimental data that were obtained in a very broad energy range from GSI/SIS through BNL/AGS, CERN/SPS

and BNL/RHIC [4, 5]. At SPS and RHIC the chemical freeze-out parameters seem to reach the critical conditions obtained from lattice calculations. Figure 1.2 shows results from a lattice

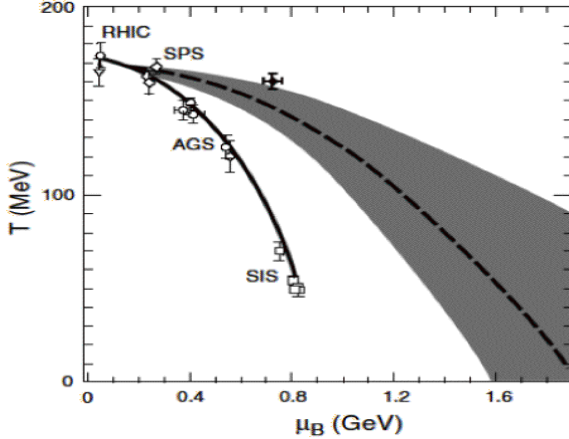


Figure 1.1: Lattice QCD Monte Carlo results on QCD-phase boundary [2, 3]. The filled point represents the endpoint of crossover transition. Open symbols: chemical freeze-out conditions obtained from a statistical analysis of experimental data [4, 5].

QCD calculation of the energy density (ϵ/T^4) as a function of temperature [6]. The sharp rise of the energy density at $T_c \sim 175$ MeV for two light quark flavors signals an increase of the effective number of degrees of freedom. The transition becomes the first order for three light flavors, but the order of the phase transition is still not clear for a realistic value of the strange quark mass. However, a sharp crossover is clearly present.

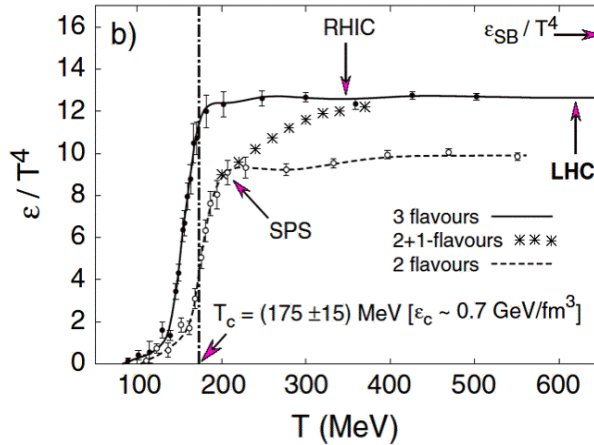


Figure 1.2: Energy density (ϵ/T^4) for 2- and 3-flavor QCD with light quarks [6].

1.2 Quark Gluon Plasma

The principle of asymptotic freedom states that the effective coupling constant α_s of QCD falls with increasing momentum transfer Q^2 , or equivalently with decreasing distance between particles. In a thermal medium, the characteristic momentum transfer between massless particles is of order the temperature T, and thus the effective coupling between quarks and gluons must become weak when T goes up. So we expected to form a plasma composed of weakly interacting quarks and gluons (QGP). Now the question is: “How the QGP can be detected?” The experimental search of QGP state has been based on various possible signals which can provide evidence of its formation. Through those signals, we try to determine if the created system is thermally equilibrated, and if it is not just hadron gas. It was expected that the search for the QGP would proceed by looking for its predicted properties, or by the discovery of anomalies or discontinuities as a function of some experimental observable, for example, collision energy $\sqrt{s_{NN}}$ in A+A collisions. Various experimental signatures/probes have been proposed with their sensitivity to expected properties of the QGP. For example, degrees of freedom, strangeness enhancement, J/ψ suppression (Debye screening), jet quenching can be listed as signatures. However, it was also realized that systematic studies and comparison of p+p, p(d)+A and A+A data are equally important to understand basic processes behind the phenomena observed in A+A collisions [7]. The importance is to distinguish the ordinary physics of relativistic heavy ion collisions from the signatures of production of a new phenomenon like QGP. The characterization of QGP properties is also based on those signals. Here the properties include: equation of state, order of the phase transition, transport properties, hadronization mechanisms, and so on. And it is of course important how to relate the QGP properties to observations in the laboratory.

1.3 Relativistic Heavy-Ion Collisions

Relativistic heavy ion collisions is the means to approach the QGP state. Currently, generating and exploring the QGP state is underway at RHIC (the Relativistic Heavy Ion Collider at BNL), and soon at LHC (the Large Hadron Collider at CERN). RHIC was constructed to investigate the properties of nuclear matter at high energy densities. The motivation for this research arose in the 1970’s from speculations about possible states of nuclear matter at high nuclear densities. Since 1980’s many experimental relativistic heavy-ion programs have been performed at AGS, SPS, and now being at RHIC.

1.3.1 p+p, p(d)+A, A+A Collisions

As said before, systematic studies of p+p, p(d)+A data are important both as a benchmark for the understanding of A+A collisions and as a means to explore physics in itself. Most of

the heavy-ion observables require p+p measurements of the same observables for comparison. Because it is necessary to identify the specific collective effects in A+A collisions and to separate them from phenomena present already in p+p collisions. For example, the following items can be listed as a part: (i) Slopes of transverse-mass distributions: comparison of slopes in A+A collisions with those in p+p allows one to determine the collective effects such as transverse flow present in A+A and absent in p+p. (ii) Particle yields and ratios: particle ratios are indicative of chemical equilibration achieved in A+A collisions and should be compared to those in p+p collisions. (iii) Ratios of momentum spectra: ratios of transverse momentum spectra at sufficiently high momenta allow one to discriminate between different partonic-energy losses of quarks and gluons. (iv) Jet fragmentation functions: model calculations of medium-induced parton-energy loss predict a modification of jet fragmentation functions.

In p(d)+A and A+A collisions, multiple scattering occurs at both hadronic and partonic levels. Multiple scattering influences many aspects of the dynamics of high energy nuclear collisions, in particular the initial parton scattering responsible for bulk particle production and rare hard processes. It depends on the geometry of A+A collision. Determination of the collision geometry is a key element in the study of heavy ion collisions. Experimentally, the number of forward neutrons and the total multiplicity in A+A collisions are used for determining an impact parameter. The impact parameter dependence of N_{coll} (number of binary nucleon-nucleon collisions) and N_{part} (number of participating nucleons) can be evaluated with a Glauber model (see Section 3.1 for centrality tagging and Glauber calculation).

1.3.2 Collision Dynamics

Static properties of QGP are evaluated and predicted by lattice QCD calculations, however the dynamical properties are still less known because the lattice gauge theory does not permit a direct calculation of quantities related to real-time evolution.

A phenomenological picture of collision is the following. Figure 1.3 shows a picture of space-time evolution of heavy-ion collisions. After an impact of the incoming nuclei, the kinetic energy of both nuclei would be partially dissipated in the overlapped region of colliding nuclei. The system is heated so that it undergoes a phase transition from normal nuclear matter to QGP state. The QGP is a deconfined state with chemical and thermal equilibration, which lasts over a short formation time ($\tau \sim 10$ fm/c). Then the system expands longitudinally and transversely, and cools, and hadronization occurs. Eventually it freezes out to a system of hadrons which are observable. Thus, hadrons produced in the collision are the most abundant and dominant source of information about the collisions. However they suffer from final-state interactions, which partially mask the early information.

When colliding two nuclei, a part of the initial kinetic energy (39 TeV in Au+Au at $\sqrt{s_{NN}} = 200$ GeV) is redistributed after the collision in terms of particle production and collective mo-

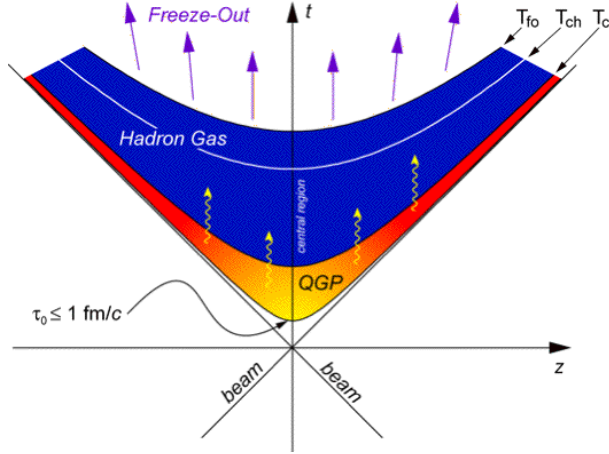


Figure 1.3: Schematic view of space-time evolution of heavy-ion collisions.

tion. The BRAHMS experiment measures the rapidity distribution of net-protons as shown in Figure 1.4, and determines how much kinetic energy appears to be retained [8]. The data indicates that in central Au+Au collisions, over 28 ± 3 TeV of energy is deposited in heating the newly created medium and collective motion. The PHOBOS experiment observes the creation of approximately ~ 5000 charged particles and thus ~ 7500 total particles including neutral particles [9]. The mean transverse momentum for pions is of order 400 MeV. If we translate this into three dimensions and multiply by the particle number, we obtain transverse energy of only about 4 TeV which is available for particle production (excitation) in heavy ion collisions. Thus, a large fraction of the incident energy translates into the longitudinal expansion. Indeed we can see a flat rapidity distribution of charged particles around midrapidity. So longitudinal boost invariance partly holds at midrapidity. Figure 1.5 shows the Bjorken energy density estimate

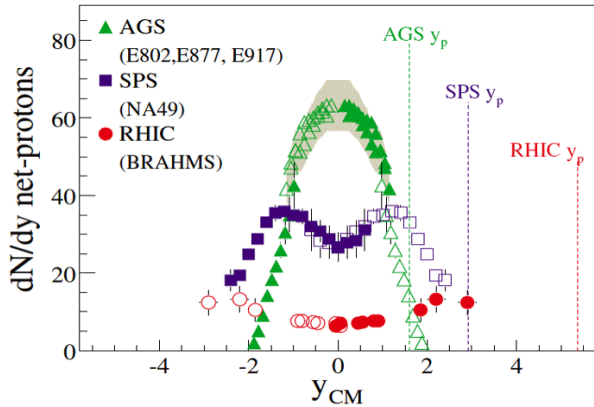


Figure 1.4: Rapidity distributions of net protons at AGS, SPS, RHIC [8].

$\epsilon_{Bj}\tau$, which is the transverse energy density divided by the transverse overlap area, multiplied by τ (formation time) [10]. If we take $\tau = 0.35$ fm/c as a reasonable time scale [11], then $\epsilon_{Bj}\tau$ is

$\sim 15 \text{ GeV/fm}^3$ in central 200 GeV Au+Au collisions. The values is much larger than the energy density ($\sim 0.6 \text{ GeV/fm}^3$) of the phase transition predicted by lattice QCD calculations.

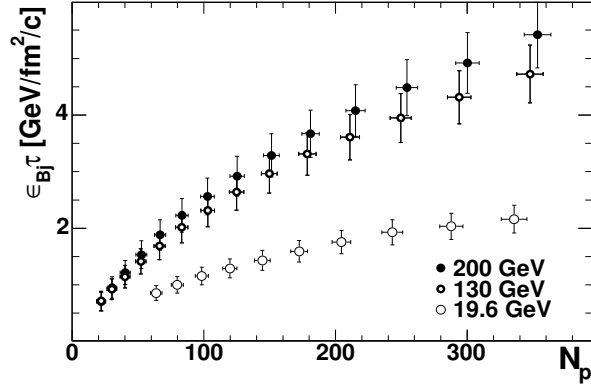


Figure 1.5: $\epsilon_{Bj}\tau$ at RHIC three energies (PHENIX) [12].

Various modeling tools have been developed to describe the collision dynamics including space-time evolution. Relativistic hydrodynamic calculation is one of them. The following items are frequently explained/discussed in those models.

- Initial conditions
- Thermalization
- Hydrodynamical expansion
- Propagation of hard probes through the matter (parton energy loss)

They try to extract basic thermodynamic and transport properties from the data, such as equation of state, viscosity, stopping power, heavy quark diffusion constant, and color screening length and so on.

1.3.3 RHIC Findings

The RHIC data taken so far are already providing various findings about the properties of medium created at RHIC. Major findings are shown below.

- High- p_T suppression

One of the discoveries at RHIC is that both neutral pion and charged hadron spectra at high $p_T > 2$ GeV/c in central Au+Au collisions are suppressed relative to the p+p or peripheral spectra normalized by the number of binary nucleon collisions (N_{coll}). Figure 1.6 shows R_{AA} (ratio of spectra in A+A to in p+p normalized by N_{coll}) as a function of p_T for π^0 , η , direct γ [13]. This suppression is described in terms of “jet quenching” effect (parton

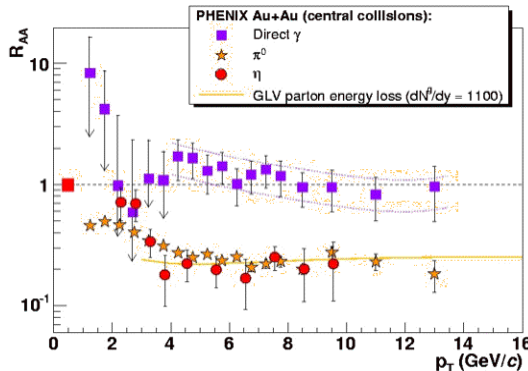


Figure 1.6: R_{AA} as a function of p_T for π^0 , η , direct γ in central Au+Au collisions at $\sqrt{s_{NN}} = 200$ GeV [13].

energy loss via gluon radiation) which is considered as an important probe for the early stage of heavy ion collisions where very hot, dense partonic matter (QGP) could exist. On the other hand, direct γ is not suppressed as expected because it should not loss the energy in the medium. At RHIC, the collision energy is high enough to occur hard scattering of partons (quarks and gluons) leading to jets of hadrons. Over the past years, a lot of work has been devoted to study the propagation of jets through QCD matter experimentally and theoretically. For example, angular multi-particle correlation studies in experiments, pQCD calculations including nuclear effects such as parton energy loss are going on in theory side. Also, clear back-to-back angular correlations between high- p_T particles seen in p+p and d+Au are absent in Au+Au data. This is another support for jet quenching [14]. In order to confirm that the observation of suppression is specific in Au+Au, a control experiment d+Au was carried out. The d+Au collisions are expected not to produce the hot-dense state. Hence the observed absence of high- p_T suppression in d+Au tells us that initial-state effects are small, so that the suppression observed in Au+Au collisions is most likely due to parton energy loss in the hot medium [15].

- Baryon enhancement

However the amount of the suppression depends on hadron species in the p_T range of 2-4 GeV/c. Protons were found not to be suppressed in this p_T range as shown in Figure 1.7. Proton to pion ratio is clearly higher around $p_T = 2$ -3 GeV/c in central Au+Au collisions, which has never seen in elementary collisions. The STAR experiment also shows that $\Lambda/K^0 > 1$ at $p_T = 2$ -3 GeV/c [16]. Baryons are enhanced compared to mesons. Clearly,

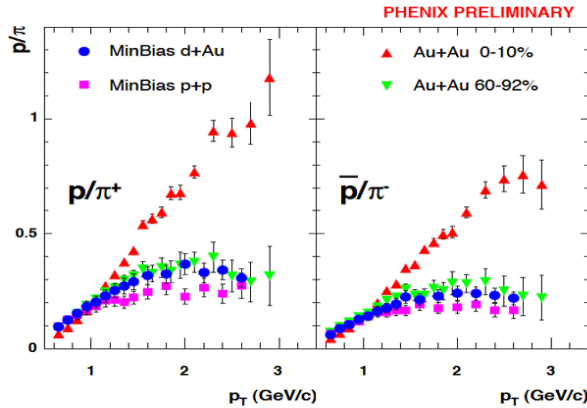


Figure 1.7: $p(\bar{p})/\pi$ ratio vs. p_T in Au+Au, d+Au, p+p collisions.

something is going on in this p_T region which has come to be called intermediate p_T . Quark recombination model has been proposed to explain this baryon enhancement. If light quarks have a thermal distribution like an exponential function, then the production of protons via recombination at intermediate p_T is favored over fragmentation from a power-law distribution. The p/π ratio is also enlarged because a proton of given p_T is produced by recombination of 3 constituent quarks of $p_T/3$, so there is no penalty compared to forming a pion from 2 quarks of $p_T/2$. This model requires the assumption of a thermalized partonic phase, which could be called QGP. Unfortunately, this model cannot explain all facets of the data at intermediate p_T . For example, from angular two-particle correlation study, baryons and mesons seem to form jet-like structure even at this p_T range [17].

- Thermalization

Relative particle abundances are compared to expectations from statistical models, as studied at SPS energies. Figure 1.8 shows various particle ratios of hadronic yields measured at midrapidity in central Au+Au collisions at $\sqrt{s_{NN}} = 200$ GeV. They are compared to results of a statistical model fit, which is based on a grand canonical ensemble with parameters such as temperature, chemical potential [18]. The agreement between data and the model looks good. We now consider that final state hadrons are emitted from a locally thermal source following a statistical distribution. The fitted baryon chemical potential $\mu_B = 28 \pm 3$ MeV is small compared to those at lower energies, indicating low net baryon

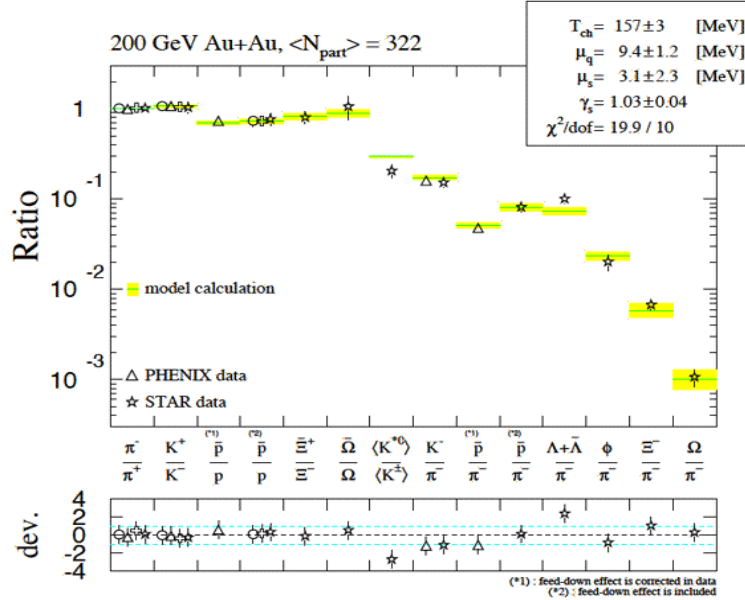


Figure 1.8: Comparison of fit results to the data in central Au+Au collisions at $\sqrt{s_{NN}} = 200$ GeV [18].

density in the medium. The chemical freeze-out temperature $T_{ch} = 157 \pm 3$ MeV appears to be close to the QCD phase transition temperature from lattice calculations.

- Hydrodynamic behavior

Figure 1.9 shows transverse momentum spectra for $\pi/K/p$ in Au+Au collisions at $\sqrt{s_{NN}} = 200$ GeV. At low p_T , the spectra for protons has a convex shape compared to other particle species. This observation indicates that the system is expanding with radial collective flow. The strength of radial flow in central collisions is larger than that in peripheral collisions. These features were already observed at SPS.

Large azimuthal anisotropy v_2 observed in heavy-ion collisions is another discovery at RHIC. v_2 is the strength of elliptic component of collective flow which is defined as the second moment of the fourier expansion of particle emission in azimuthal angle. The v_2 reflects the shape of initial overlap region of two nuclei, and the subsequent collective expansion process. Compared with collisions at lower energies, the values of v_2 are found to be larger, which suggest that thermalization is taking place much faster than expected from normal hadronic rescattering. Thus the large v_2 implies other ingredients (i.e. quarks and gluons) for thermalization than hadrons. Not only light hadrons but also decay electrons from D, B mesons show finite v_2 as large as 10% [20]. As shown in Figure 1.10, p_T dependence of v_2 provides important clues to understand the particle production. At p_T region below 1.5 GeV/c, the curves of $\pi/K/p$ particles are consistent with hydrodynamic calculation. A clear departure from the hydrodynamic behavior is observed at higher p_T . It

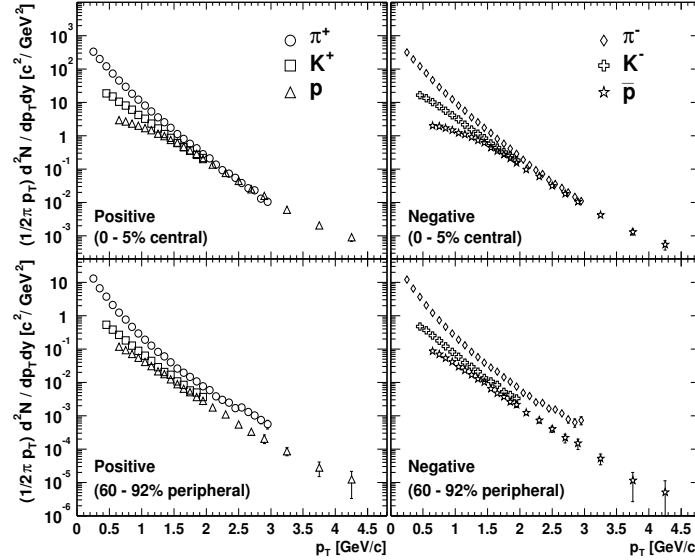


Figure 1.9: Transverse momentum spectra for $\pi/K/p$ in Au+Au collisions at $\sqrt{s_{NN}} = 200$ GeV (PHENIX) [19].

is believed that the v_2 values above 2 GeV/ c depend on an interplay between hydrodynamic process and hard process.

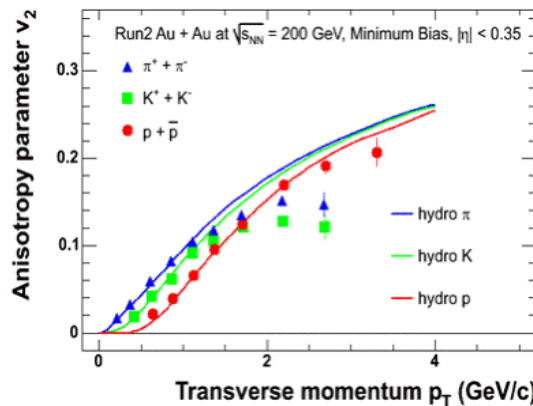


Figure 1.10: Elliptic flow strength v_2 vs. p_T in 200 GeV Au+Au collisions with hydro model lines [21].

Differential elliptic flow and radial flow patterns in Au+Au collisions at $\sqrt{s_{NN}} = 200$ GeV are remarkably well described at low p_T by ideal relativistic hydrodynamics calculations. This is one of the evidences suggesting that the matter produced at RHIC exhibits very small viscosity (i.e. very short mean free path), thus nearly perfect fluid properties, instead of behaving like a gas of free quarks and gluons. Moreover, v_2 values of mesons and baryons

are scaled with the number of constituent quarks (2 for mesons, 3 for baryons). The scaled v_2 shows a universal curve for mesons and baryons as in Figure 1.11. This curve indicates a quark-level elliptic flow, and the hadronization is happened through quark recombination process.

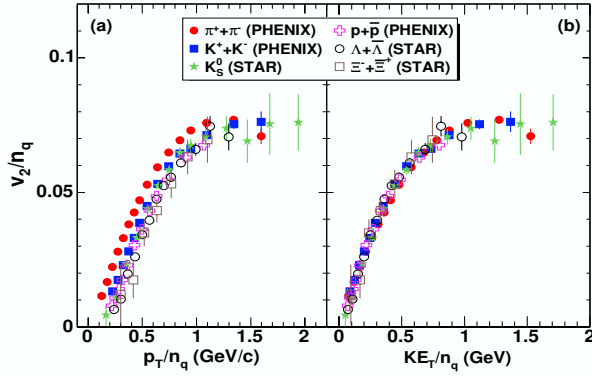


Figure 1.11: v_2/n vs p_T/n (KE_T/n) for identified particle species in minimum bias 200 GeV Au+Au collisions. n denotes the number of constituent quarks (2 for mesons, 3 for baryons) [22].

1.3.4 Hadron Production at Intermediate p_T

As mentioned in Section 1.3.3, one of the most remarkable observations in heavy ion collisions at RHIC is a large enhancement of baryons and antibaryons at intermediate p_T (2-5 GeV/c). In central Au+Au collisions at $\sqrt{s_{NN}} = 200$ GeV, there is a significant suppression in meson yields (π , K , etc.) compared to peripheral Au+Au or p+p results. In contrast, a large enhancement of baryons (p , \bar{p} , Λ , etc.) relative to mesons is observed at intermediate p_T [23, 24]. The (anti)proton to pion ratio is enhanced by almost a factor of 3 when one compares most central Au+Au events to peripheral or p+p events. On the other hand, in elliptic flow measurements, a baryon-meson difference is also found in its magnitude (v_2 as a function of p_T). We now recognize that these observations as a baryon-meson difference at intermediate p_T . In this p_T region, jet fragmentation process dominates the hadron production in p+p collisions. And we expect that the fragmentation is independent of collision system. Therefore the large baryon fraction observed at RHIC is one of the surprising findings. By performing a control experiment - d+Au collisions, in which only cold nuclear matter is produced, we found that the suppression of hadron yields is not caused by initial state interactions, but by final state interactions (i.e. jet quenching) [25]. We also found that the Cronin effect (enhancement from multiple scattering) has a particle-type dependence. The Cronin effect is larger for protons than those for pions, kaons. However this difference between baryons and meson is not enough to account for the baryon enhancement seen in Au+Au collisions [26].

The observed baryon enhancement is explained in some different ways:

- Strong radial flow which pushes heavier particles to larger p_T [27]
- Recombination of hard-scattered quarks with quarks from thermalized medium [28]
- Baryon junction mechanism [29]
- Medium modification of jet fragmentation [30]

The intermediate p_T region is considered a transition region from soft to hard hadron production mechanism. Here, soft part includes hydrodynamic flow [27], quark recombination [28], etc. Hard part includes jet fragmentation and its quenching. Multiple hadronization mechanisms and final-state interaction are involved at intermediate p_T . However the relative contributions of soft/hard parts are not yet fully understood. So the next step is answering the following questions of the baryon-meson difference at intermediate p_T : “What is the origin?”, “If multiple mechanisms are involved, what are their relative contributions?” In other words, we should know (i) what p_T hydrodynamic contribution exist up to, (ii) if quark recombination process is really necessary, (iii) if we can separate radial flow between hadronic and partonic phases.

1.4 Thesis Motivation

The purpose of this thesis is to study hadron production mechanisms at intermediate p_T (2-5 GeV/c) and final-state interactions between hadrons produced in relativistic heavy ion collisions. The main target is to find the origin of the baryon enhancement at intermediate p_T by focusing on (anti-)proton production. Since (anti-)proton is sensitive to collective flow due to its relatively large mass and indicative for baryon number transport especially at lower energies.

In the PHENIX experiment, the particle identification capability has been enhanced by the introduction of a new aerogel Cherenkov counter. (I have contributed to the R&D, construction, installation processes of the counter.) We can now study the identified charged hadron production at higher p_T than past (up to 5 GeV/c for charged pions, and 7 GeV/c for (anti)protons). We measure identified inclusive single particle spectra using the data taken at the PHENIX experiment. The spectra are measured at mid-rapidity ($|\eta| < 0.35$) over the range of $0.5 < p_T < 6$ GeV/c with particle identification by time-of-flight and threshold-type Cherenkov light emission methods. We perform a systematic study of proton and antiproton spectra in Au+Au/Cu+Cu/p+p collisions at $\sqrt{s_{NN}} = 200/62.4$ GeV. The data set allow us to study the energy dependence and system size dependence of the baryon enhancement. In addition to heavy ion data, we have obtained high statistics 200 GeV and 62 GeV p+p data. The p+p data provides baseline spectra to heavy ion data. It is important to quantify in-medium nuclear effects to hadron production in heavy ion collisions.

In the thesis, we present identified charged hadron p_T spectra, particle ratios, nuclear modification factors, freeze-out properties and their scaling properties between different collision

systems. From the results, we try to estimate the relative contributions of soft/hard components in the hadron production. And we try to answer the questions listed at the end of Section 1.3.4. The measurement could provide valuable inputs for understanding the hadronization and nuclear medium effects in the matter created in relativistic heavy ion collisions.

Chapter 2

Experimental Setup

In this chapter, the experimental setup is described. The RHIC facility and PHENIX detector are explained.

2.1 Relativistic Heavy-Ion Collider

The Relativistic Heavy Ion Collider (RHIC) at Brookhaven National Laboratory is a 3.8-km circumference accelerator composed of two identical, quasi-circular rings of superconducting magnets (~ 400 dipoles and ~ 500 quadrupoles) with six crossing points. RHIC can accelerate nuclei (protons) up to a maximum of 100 (250) GeV/c per nucleon. The center-of-mass energies in A+A and p(d)+A collisions, $\sqrt{s_{NN}} = 200$ GeV ($\sqrt{s} = 500$ GeV for p+p), are over an order of magnitude higher than those at CERN-SPS ($\sqrt{s_{NN}} = 17.3$ GeV). The achieved average A+A luminosity is $\sim 4 \times 10^{26}$ cm $^{-2}$ s $^{-1}$. There are four dedicated experiments at RHIC: PHENIX, STAR, BRAHMS and PHOBOS. The layout of RHIC accelerator complex is shown in Figure 2.1 [31].

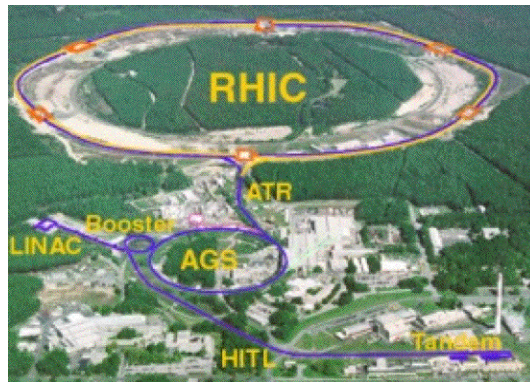


Figure 2.1: Layout of RHIC accelerator complex.

Table 2.1: Physics run summary table in PHENIX.

Run	Year	Species	$\sqrt{s_{NN}}$ [GeV]	$\int L dt$	N_{event}
01	2000	Au+Au	130	$1 \mu b^{-1}$	10 M
02	2001/2002	Au+Au	200	$24 \mu b^{-1}$	170 M
		p+p	200	$0.15 pb^{-1}$	3.7 G
03	2002/2003	d+Au	200	$2.74 nb^{-1}$	5.5 G
		p+p	200	$0.35 pb^{-1}$	6.6 G
04	2003/2004	Au+Au	200	$241 \mu b^{-1}$	1.5 G
		Au+Au	62.4	$9 \mu b^{-1}$	58 M
		p+p	200	$0.35 pb^{-1}$	6.6 G
05	2004/2005	Cu+Cu	200	$3 nb^{-1}$	8.6 G
		Cu+Cu	62.4	$0.19 nb^{-1}$	400 M
		Cu+Cu	22.5	$2.7 \mu b^{-1}$	9 M
		p+p	200	$3.8 pb^{-1}$	85 G
06	2006	p+p	200	$10.7 pb^{-1}$	230 G
		p+p	62.4	$0.1 pb^{-1}$	28 G

Heavy ion beams originate in a pulsed sputter source and are accelerated successively by Tandem van der Graaf accelerator, Booster Synchrotron, and Alternating Gradient Synchrotron (AGS), where they are accelerated to 10.8 GeV/nucleon, fully stripped of their electrons, and injected into RHIC. Acceleration and storage in RHIC utilize two Radio-Frequency (RF) systems, one at 28 MHz to capture AGS bunches and accelerate to top energy, the other at 197 MHz to provide a short collision diamond (25 cm) for efficient utilization of luminosity by the experiments. The synchrotron phase transition of RHIC lattice is at $T = 24.7$, meaning that all ions except protons pass through the beam instability at the transition. For light ions ($A < 100$), the luminosity is limited by beam-beam hadronic interactions, whereas for heavier ions the luminosity lifetime is limited by intra-beam (intra-bunch) scattering. The RHIC beams are brought into head-on collision at intersection regions. The final dipoles of the lattice are approximately 10 m from a collision diamond. Table 5.1.2 lists the beam species, energies, and integrated luminosity for the RHIC runs to date. Figure 2.2 shows the nucleon-pair luminosity L_{NN} in the past RHIC runs [32]. In the future, RHIC is planned to be upgraded to increase its luminosity to study hard and rare probes with low cross section or small branching ratio.

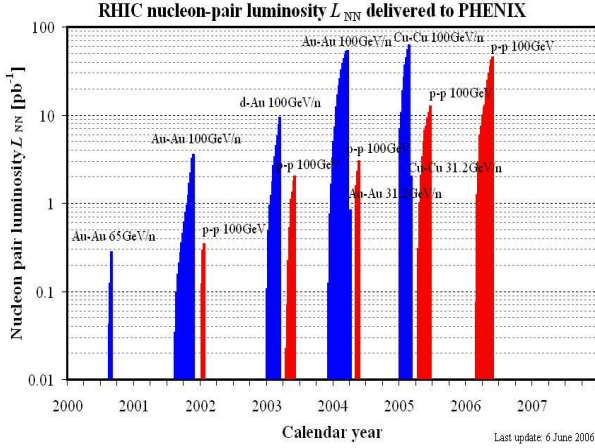


Figure 2.2: Nucleon-pair luminosity L_{NN} in the past RHIC runs. Note: L_{NN} is defined as $L_{NN} = A_1 A_2 L$.

2.2 PHENIX Detector Overview

The PHENIX (Pioneering High Energy Nuclear Interaction eXperiment) is one of the experiments at RHIC. The PHENIX detector is designed to measure hadrons, leptons and photons with good momentum and energy resolution. Another advantage is the ability to detect rare signals with potential physics interest (direct photons, lepton pairs, jet fragments, etc.) by using Level-1 and Level-2 triggers. The detector consists of a large number of detector subsystems. It is divided into:

- 2 central arm spectrometers for electron, photon and hadron measurements at mid-rapidity ($|\eta| < 0.35$, $\Delta\phi = \pi$).
- 2 forward spectrometers for muon detection ($|\eta| = 1.15 - 2.44$, $\Delta\phi = 2\pi$).
- Global detectors for trigger and centrality selection.

The cut view and top view of the PHENIX detector are shown in Figure 2.3 and 2.4. The midrapidity spectrometers have an axial magnetic field (strength 1.15 T·m), with tracking and momentum measurements supplied by a drift chamber (DC) and 3 layers of MWPC's with pad readout (PC). Charged hadron identification over a broad momentum range is provided by Time of Flight (TOF), Ring Imaging Cerenkov (RICH), and Aerogel Cherenkov Counter (ACC). Electrons and photons are measured in highly granular lead scintillator and lead glass calorimeters (EMCal). The combination of EMCal, RICH provides a hadron background rejection factor for electron measurements of $\sim 10^3$ over a wide momentum range. The forward muon arms have a radial magnetic field, with tracking based on drift chambers followed by a muon identifier consisting of alternating layers of steel absorber and streamer tubes. The PHENIX detector

subsystems are summarized in Table 2.2. In the following data analysis, the global detectors and a subsets of the central arm detectors are used. They are explained in the following sections.

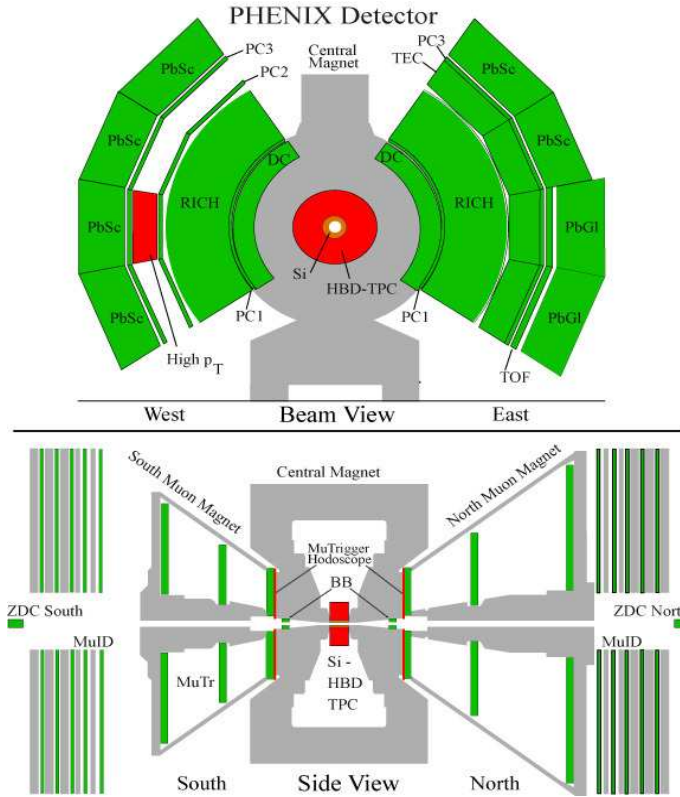


Figure 2.3: Cut view of PHENIX detector in 2005 (top: beam view, bottom: side view).



Figure 2.4: Top view of PHENIX detector.

Table 2.2: Summary of PHENIX detector subsystems.

Subsystem	$\Delta\eta$	$\Delta\phi$	Purpose and Special Features
Magnet: central (CM)	$ \eta < 0.35$	360°	Up to 1.15 T·m.
muon (MMS)	-1.1 to -2.2	360°	0.72 T·m for $\eta = 2$
muon (MMN)	1.1 to 2.4	360°	0.72 T·m for $\eta = 2$
Beam-beam (BBC)	$3.0 < \eta < 3.9$	360°	Trigger, start timing, z vertex, reaction plane
ZDC	± 2 mrad	360°	Minimum bias trigger.
Drift chambers (DC)	$ \eta < 0.35$	$90^\circ \times 2$	Good momentum and mass resolution, $\Delta m/m = 0.4\%$ at $m = 1\text{GeV}$.
Pad chambers (PC)	$ \eta < 0.35$	$90^\circ \times 2$	Pattern recognition, tracking for nonbend direction.
RICH	$ \eta < 0.35$	$90^\circ \times 2$	Electron identification.
TOF	$ \eta < 0.35$	45°	Good hadron identification, $\sigma \sim 120$ ps.
ACC	$ \eta < 0.35$	20°	High- p_T hadron identification, $n = 1.011$
PbSc EMCal	$ \eta < 0.35$	$90^\circ + 45^\circ$	For both calorimeters, photon and electron detection.
PbGl EMCal	$ \eta < 0.35$	45°	Good e^\pm/π^\pm separation at $p > 1\text{ GeV}/c$ by EM shower and $p < 0.35\text{ GeV}/c$ by ToF. K^\pm/π^\pm separation up to $1\text{ GeV}/c$ by ToF.
μ tracker: (μ TS)	-1.15 to -2.25	360°	Tracking for muons.
(μ TN)	1.15 to 2.44	360°	Muon tracker north installed for year-3
μ identifier: (μ IDS)	-1.15 to -2.25	360°	Steel absorbers and Iarocci tubes for
(μ IDN)	1.15 to 2.44	360°	muon/hadron separation.

2.3 Global Detectors

Event triggering is based on Beam-Beam Counters (BBC) and Zero Degree Calorimeters (ZDC). The minimum bias trigger efficiency is $\sim 93\%$ for 200 GeV Au+Au case.

The PHENIX data acquisition system is able to record ~ 500 MB/s to disk with event size of ~ 100 KB (i.e. event rate of ~ 5 kHz). The PHENIX on-line system takes signals from Front End Modules (FEM) on each detector subsystem. Processing of event data begins when Data Collection Modules (DCM) receive data via fiberoptic links from the FEM's. The DCM's format/zero-suppress the data and generate data packets. These packets go to Event Builders that assemble the events in final form. All of this is controlled by Master Timing System that distributes the RHIC clocks. A two-level trigger system has been implemented in the PHENIX experiment. Level 1 trigger system (LVL1) processes the reduced data from a part of detector subsystems in parallel and makes a decision on each beam crossing. For each accepted event the information from LVL1 is added to the detector data stream. The Level 2 trigger system (LVL2) makes a fast analysis of each accepted event and decides if its data have to be stored or to be discarded.

Event characterization (collision vertex, start timing, collision centrality) is also performed with these global detectors. The BBC timing resolution of 40 ps results in a vertex position resolution of 0.6 cm. Since the multiplicity of both forward neutrons in ZDC and charged particles in BBC are correlated with the collision geometry, they can also be used to measure the collision centrality (see Section 3.1.3).

2.3.1 Beam Beam Counters (BBC)

Beam-Beam Counters (BBC) measure the timing and energy deposit of leading charged particles from collisions. Two BBCs are placed 144 cm from the center of the intersection region on North and South sides, and surround the beam pipe. This corresponds to a pseudo rapidity range from 3.0 to 3.9 over the full azimuth. Each BBC is composed of 64 BBC elements (see Figure 2.5). A BBC element consists of an one-inch mesh dynode photomultiplier tube mounted on a 3 cm quartz Cherenkov radiator. The main roles of BBCs are: (i) to produce a signal for the PHENIX Level-1 trigger, (ii) to provide a start time of Time-of-Flight measurement, (iii) to measure a collision vertex point along the beam axis, (iv) to determine a collision centrality and (v) to determine an angle of the reaction plane on an event-by-event basis. The BBC is designed to operate under various collision species (dynamic range 1-30 MIPs), high radiation and large magnetic field (0.3 T).

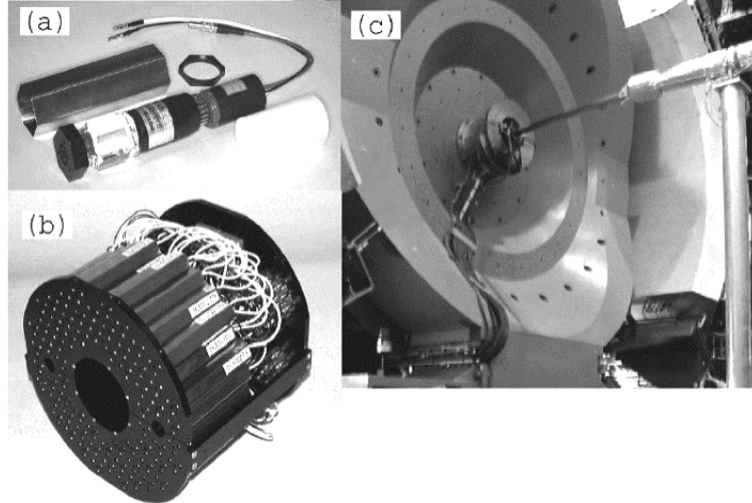


Figure 2.5: (a) Single Beam Beam counter. (b) A BBC array comprising 64 BBC elements. (c) BBC counter mounted on the PHENIX detector. The beam pipe is seen in the middle of the picture.

2.3.2 Zero Degree Calorimeters (ZDC)

Zero-Degree Calorimeters (ZDC) are compact tungsten/fiber hadronic calorimeters, and detect neutral beam fragments from collisions. Two ZDCs are used for triggering, luminosity monitoring, and centrality determination. The ZDCs are located 18 m downstream and upstream from the interaction point along the beam axis, with acceptance 2.5 mrad centered on the beam direction (see Figures 2.6 and 2.7). In front of the ZDCs, DX dipole magnets are installed. The energy flux into this acceptance in heavy ion collisions is dominated by non-interacting spectator neutrons. Charged particles emitted from collisions are deflected out of the ZDC acceptance by the magnets. The ZDC energy resolution is sufficient to discriminate individual beam velocity neutrons. The luminosity for Au + Au collisions has been measured with 10% precision using a Vernier scan of ZDC coincidence rates [33].

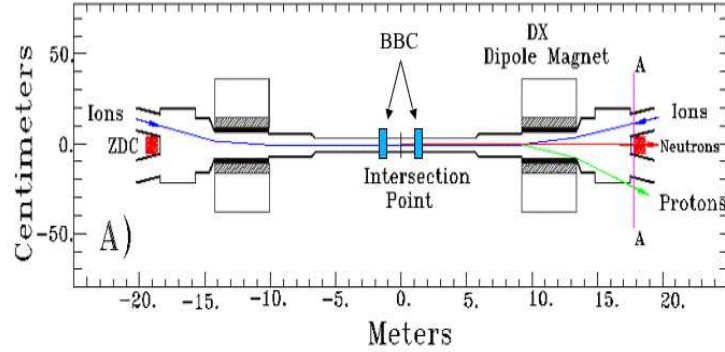


Figure 2.6: Location of ZDCs along the beam line.

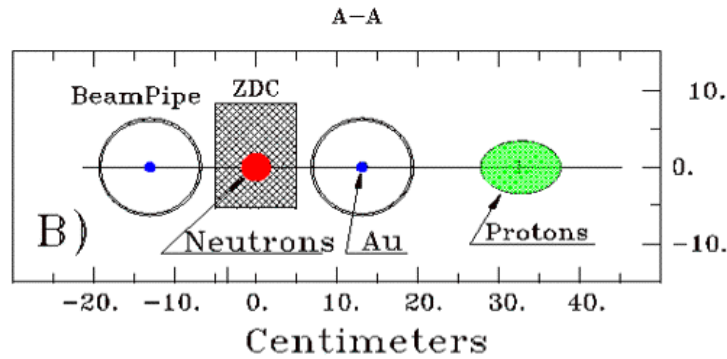


Figure 2.7: Cut view at A-A position of the above picture.

2.4 Central Arm Spectrometers

Each of west and east central arm spectrometers covers a pseudo-rapidity range of $|\eta| < 0.35$ and an azimuthal angle ϕ of 90 degrees. As shown in the upper panel of Figure 2.3, each of the spectrometers consists of layers of tracking and particle identification detectors. Particle identification (PID) is a vital part of the PHENIX detector. There are multiple subsystems dedicated for the PID. One is the Time-of-flight (TOF) subsystem using scintillation light emitted from plastic scintillator. And the other is the RICH subsystem using Cherenkov light emitted from radiator gas. Currently the RICH is using carbon dioxide gas (CO_2). As well as the TOF, Electromagnetic calorimeter (EMCal) provides flight time with larger acceptance coverage in azimuthal angle. EMCal is used also for measurement of neutral pion through two-gamma decay.

In the past, hadron identification capability of the PHENIX has holes in the momentum range: 2.5-5 GeV/c for π/K separation, >4 GeV/c for K/p separation. For further physics research, extension of the momentum range was desired. So an aerogel threshold Cherenkov

counter (ACC) was proposed to extend the momentum range. By the addition of ACC with the refractive index of 1.011, those gaps would be bridged, and hadron particle identification can be achieved seamlessly up to p_T of 7 GeV/ c . The construction and installation of ACC was completed in 2003/2004. The ACC has started taking data from Run-4 period in PHENIX.

2.4.1 Central Arm Magnet

The PHENIX magnet system is composed of three spectrometer magnets, Central Magnet (CM) and Muon Magnets (MMN and MMS), with warm iron yokes and water-cooled copper coils. Figure 2.8 shows the cutaway drawing of the PHENIX magnet showing CM and MM field lines. The CM is energized by two pairs of concentric coils and provides axially symmetric magnetic field parallel to the beam axis. The magnetic field for the central arms is axially symmetric around the beam axis. Its component parallel to the beam axis has an approximately Gaussian dependence on the radial distance from the beam axis, dropping from 0.48 T at the center to 0.096 T (0.048 T) at the inner (outer) radius of DC. The total field integral is about 1.15 Tesla-meters and that is minimized for the radius of $R > 2$ m (the radius of the DC). Charged particles bend in a plane perpendicular to the beam axis. The bending angles are accurately measured by DCs, from which the charged particle momenta can be determined.

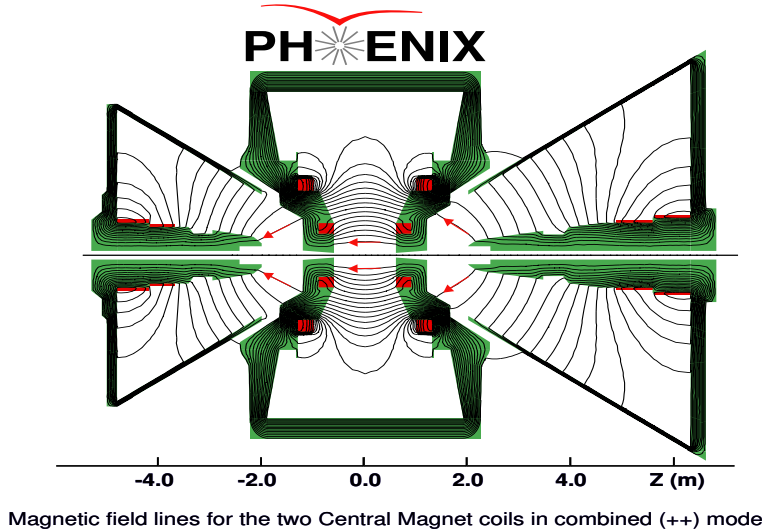


Figure 2.8: Central magnet both coils in (++) configuration with magnetic lines.

2.4.2 Drift Chambers (DC)

Drift chambers (DC) are used to measure charged particle trajectories in $r\phi$ plane and to determine their transverse momentum. The obtained tracking information is used to link tracks through outer subsystems. The following performances are obtained:

- Single wire efficiency: 95-96 %
- Track-finding efficiency: > 99 %
- Two track resolution: < 2 mm
- Single wire resolution: $\sim 165 \mu m$

The DCs are located from 2 to 2.4 m in radial direction, and have 1.8 m long along the beam direction. Each DC consists of two independent gas volumes as shown in Figure 2.9. A gas mixture of 50%Ar and 50%Ethan is chosen for the operation. Each DC covers 90° in azimuthal angle ϕ and consists of 40 planes of sensing wires subdivided into 80 drift cells, each cell spanning 1.125° in azimuth. The wire planes are arranged in six types of wire modules stacked radially in the following order, X1, U1, V1, X2, U2, V2. Each of the X, U, and V modules contains 12 and 4 sense wires, respectively. The X, U, V wire orientations are shown in Figure 2.10. The X1 and X2 wire modules run in parallel to the beam to perform precise track measurements in $r\phi$. U1,V1 and U2,V2 wire modules are placed after X1 and X2, respectively. They have stereo angles about $\pm 5^\circ$ relative to the X wires and measure the z coordinate of the track. The stereo angle is selected to match with the z resolution of pad chambers and minimize tracking ambiguities.

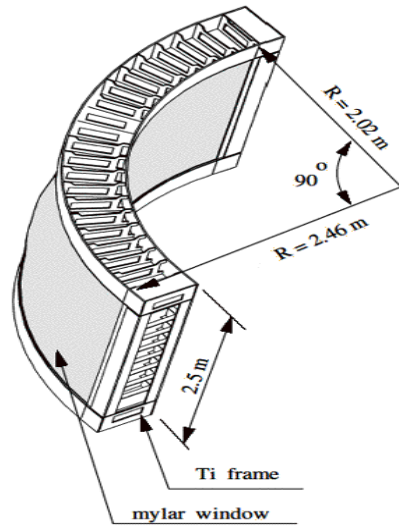


Figure 2.9: Schematic view of drift chamber frame.

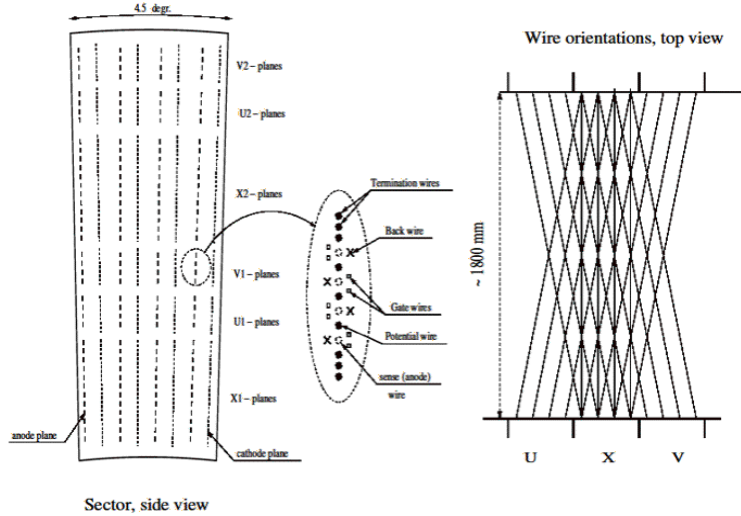


Figure 2.10: Left: Layout of wire position within one sector. Right: A schematic diagram of stereo wire orientation.

2.4.3 Pad Chambers (PC)

Pad chambers (PC) are multiwire proportional chambers that form three separate layers (PC1, PC2, and PC3) of the PHENIX tracking system. Each layer contains a single plane of wires inside a gas volume bounded by two cathode planes. One cathode is finely segmented into an array of pixels. Nine pixels are connected together electronically to form a pad (see Figure 2.11). The pad size of PC1 is $0.84 \text{ cm} \times 0.845 \text{ cm}$ which gives a position resolution of 1.7 mm along z and 2.5 mm in $r\phi$. The pad size for PC2 and PC3 is chosen such that they have similar angular resolution compared to PC1. PC1 determines a three-dimensional momentum vector for each track by providing the z coordinate at the exit of DC. The information from DC and PC1 provides direction vectors through outer subsystems. PC2 and PC3 are used to reject (i) particles produced from secondary interactions or particle decays, (ii) low-momentum primary tracks that curve around PC1 in the magnetic field and hit PC2 and PC3.

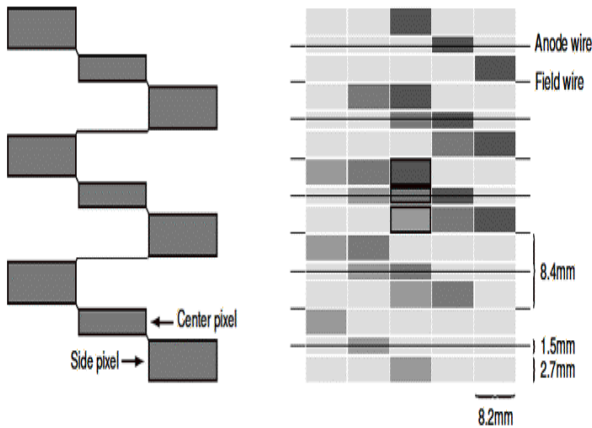


Figure 2.11: Left: Pad and pixel geometry. Right: A cell defined by three pixels.

2.4.4 Electromagnetic Calorimeters (EMCal)

Electromagnetic calorimeters (EMCal) is used to measure the spatial position and energy of electrons and photons. It covers the full central arm acceptance of $70^\circ \leq \theta \leq 110^\circ$ and $2 \times 90^\circ$ in azimuth. There are two types of calorimeters: Lead Glass (PbGl) Cerenkov calorimeters in E0/E1 sectors, Lead Scintillator (PbSc) sampling calorimeters in the other sectors. The Pb-scintillator electromagnetic calorimeter is a sampling calorimeter made of alternating tiles of Pb and scintillator consisting of 15,552 individual towers. Figure 2.12 shows a Pb-scintillator electromagnetic calorimeter module consisting of four towers. The Pb-scintillator electromagnetic calorimeter has a nominal energy resolution of $8.1\%/\sqrt{E(\text{GeV})} \oplus 2.1\%$. Low- p_T charged hadron identification is also possible from time-of-flight measurement (σ_{TOF} : 400-500 ps). Since the calorimeter has 0.85 units of hadronic interaction length, high- p_T charged hadrons also have a large probability of depositing a large fraction of their energy. So, it can be used to select a clean sample of high- p_T charged hadrons.

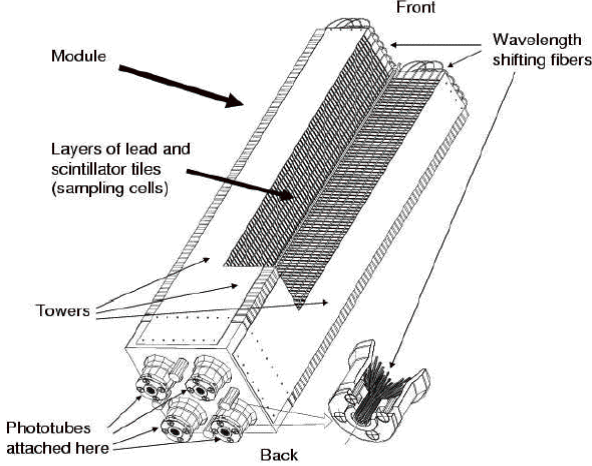


Figure 2.12: Interior view of a single Pb-scintillator calorimeter module.

2.4.5 Time of Flight Detector (TOF)

Time-of-Flight detector (TOF) provides the flight time measurement for charged hadrons. The TOF is located at a radial distance of 5.06 m from the interaction point, covering $\pi/4$ in azimuthal direction in the lower part of the east arm as shown in Figure 2.13. TOF contains 960 scintillator slats oriented along the $r\text{-}\phi$ direction. One TOF element consists of a plastic scintillator slat and PMTs equipped at the both ends of the scintillator. The Schematic diagram of the components of a single TOF panel are shown in Figure 2.14. TOF is designed to have a intrinsic timing resolution of ~ 100 ps in order to separate charged hadron in high momentum range: $3\sigma \pi/K$ separation up to 2.4 GeV/c, $3\sigma K/p$ separation up to 4.0 GeV/c. Using the following equation, particles are identified by their mass square value.

$$m^2 = p^2 \left(\left(\frac{T_{flight}c}{L} \right)^2 - 1 \right) \quad (2.1)$$

where L is the flight path length which is the distance between TOF and the vertex position in the magnetic field and T_{flight} is the flight time.

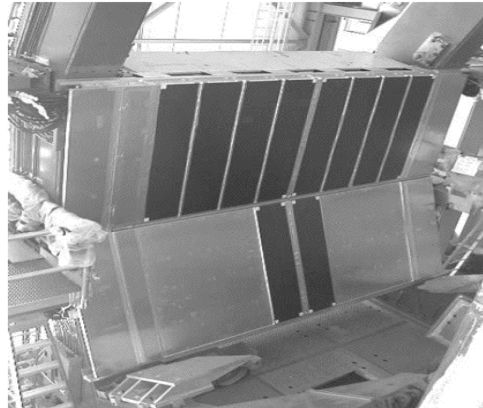


Figure 2.13: TOF detector mounted on the PHENIX East Arm.

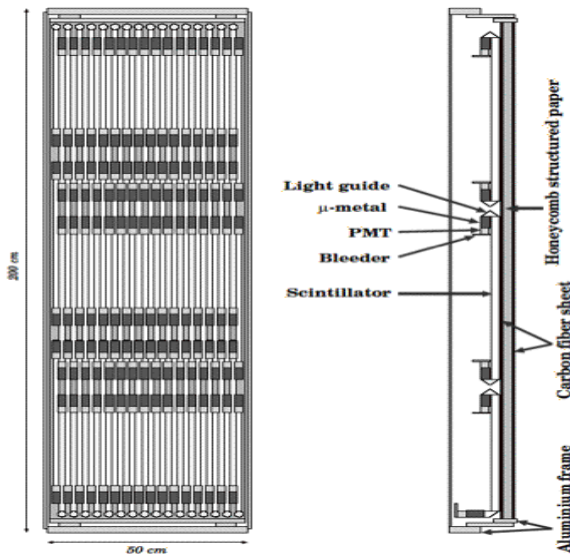


Figure 2.14: Schematic diagram of the components of a single TOF panel.

2.4.6 Aerogel Cherenkov Counter (ACC)

Aerogel Cherenkov Counter (ACC) is a particle identification detector for high- p_T charged hadrons. It was installed in 2003/2004 and started taking collision data from Run-4 period (see Figure 2.15). ACC uses Silica aerogel (refractive index of $n \sim 1.011$) as its Cherenkov radiator. The p_T reach of particle identification has been extended (up to 5 GeV/c for charged pions, and 6 GeV/c for (anti)protons) by the introduction of ACC in PHENIX. The acceptance of the aerogel counter is about 4 m^2 at a radius of $\sim 4.5 \text{ m}$ from the beam line between PC2 and PC3 at mid-rapidity (west arm W1 sector). The geometrical size of the detector is $\sim 390(z) \times 120(\phi) \times \sim 30(r) \text{ cm}^3$ ($\Delta\eta = 0.70$ and $\Delta\phi = 14 \text{ deg}$) (see Figure 2.16). The aerogel

counter is composed of 160 individual cells. The cells are stacked into an array (10 cells high (ϕ) by 16 cells wide (z)). To eliminate dead space, every other cells along z -direction are flipped in the radial direction. With this configuration, all the sensitive aerogel volumes are kept in one plane, which contributes to the uniform detector response. The occupancy of the cells is kept <10 % even in central Au+Au collisions. Each cell has aerogel volume ($22(z) \times 11(\phi) \times 12(r)$ cm 3), followed by an integration air cube viewed by two 3-inch PMTs. The beam test done at KEK-PS shows that the positional uniformity of light yield with this configuration is the best of all studied configurations. The prototype has achieved 97.2 % pion detection efficiency and 2.8 % proton fake rate (3.8 σ separation) at 2 GeV/ c , and provides enough photoelectron yield (~ 15 pe (n=1.011) per cell per charged particle with $\beta = 1$) to separate different particles. The readout electronics of ACC was developed based on that of PHENIX-RICH. It is designed to detect small signal like Cherenkov light.



Figure 2.15: Installation of Aerogel Cherenkov Counter.

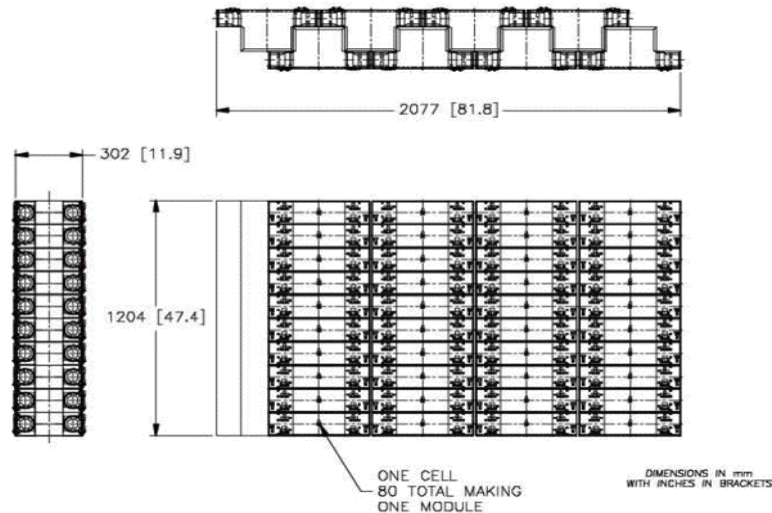


Figure 2.16: Schematic view of ACC cell array (half sector).

Chapter 3

Data Analysis

In this chapter, we describe the analysis details such as track selection, particle identification, Monte Carlo correction. The analysis is based on the experimental data taken in Run-4/Run-5 (2003~2005). The collision species and energies are: Au+Au/Cu+Cu/p+p at $\sqrt{s} = 200$ GeV. (Lower energy 62.4 GeV data were analyzed separately by other people.) Particle identification for charged hadrons is performed with ACC (Aerogel Cherenkov counter) and TOF (Time-of-Flight counter). The main observable is p_T spectra for charged pions and (anti-)protons at mid-rapidity. Particle ratios (\bar{p}/p , p/π) are also calculated. Using the p+p spectra, nuclear modification factor R_{AA} is calculated for Au+Au/Cu+Cu at $\sqrt{s_{NN}} = 200$ GeV.

3.1 Event Selection

3.1.1 Data Sets

Data sets used here are Minimum-bias triggered Au+Au/Cu+Cu/p+p collisions at $\sqrt{s_{NN}} = 200$ GeV. Those were taken in Run-4/Run-5 (2003~2005) by the PHENIX experiment. The magnetic field configuration are normal (++) and reverse (--) fields for inner and outer coils. The numbers of events are summarized in Table 3.1. We use the CNT nanoDST files which contains central arm detector information and event reconstruction information. For scanning the real data, we prepared several analysis offline codes. The codes are run under the PHENIX computing environment. The same code is used for single-particle Monte Carlo study to obtain correction factors of p_T spectra.

3.1.2 Minimum Bias Trigger and Efficiency

Event triggering is based on Beam-Beam Counters (BBC) located at $|\eta| = 3.0\text{--}3.9$. A coincidence between the north and south BBCs with minimum fired PMTs in each side is required. For 200

Table 3.1: Summary of data sets.

Run	Year	Species	$\sqrt{s_{NN}}$ [GeV]	B field setting	N_{event}
4	2003/2004	Au+Au	200	++/--	~ 440 M
5	2004/2005	Cu+Cu	200	++/--	~ 620 M
5	2005	p+p	200	--	~ 360 M

GeV Au+Au case, the minimum number is 2. In other cases, the minimum number is 1. This is called BBC Local Level-1 Minimum bias trigger at Level-1 stage. Various Level-2 triggers are also used for event monitoring and filtering. In offline analysis, a collision vertex position along the beam axis is required within $|z| < 30$ cm. The vertex position is determined by the time difference of the two BBCs. The resolution is ~ 0.6 cm. Based on a detailed simulation including BBC response and input dN/dy distributions, Minimum bias trigger efficiencies are estimated as in Table 3.2 [34]. For 200 GeV p+p case, the BBC trigger cross section is 23.0 ± 2.2 mb. If the total inelastic cross section is assumed at 42.0 mb, we obtain a fraction of $55 \pm 5\%$.

Table 3.2: Summary of Minimum bias trigger efficiencies.

Run	Species	$\sqrt{s_{NN}}$ [GeV]	MB Trigger Efficiency [%]
4	Au+Au	200	92 ± 3
5	Cu+Cu	200	94 ± 4
5	p+p	200	55 ± 5

3.1.3 Centrality Determination

The minimum bias data sample is subdivided into different centrality bins. The centrality is defined as a fraction of the total geometrical cross section. A collision centrality is determined from BBC (and ZDC) information. BBC measures charged particle multiplicity at forward rapidity. ZDC measures spectator neutrons. Since the multiplicities in BBC and ZDC are correlated with the collision geometry, they can be used to measure the collision centrality (impact parameter $|\vec{b}|$). Figure 3.1 (Left) shows the correlation between the energy sum of spectator neutrons (ZDC) and the charge sum of charged particles (BBC) in Run4 Au+Au collisions at $\sqrt{s_{NN}} = 200$ GeV. A centrality value are determined by calculating ϕ angle relative to the center on X-axis for given BBC and ZDC values. The figure illustrates the sorting way corresponding to percentile intervals of the cross section, with 0-5% indicating the most central collisions. For peripheral collisions, the spectator neutrons measured by ZDC are decreased. It is considered that intrinsic p_T from Fermi motion inside nuclei changes the direction, or they may be bound in deuterons or heavier fragments and thus swept away by the magnet. NA49 experiment also

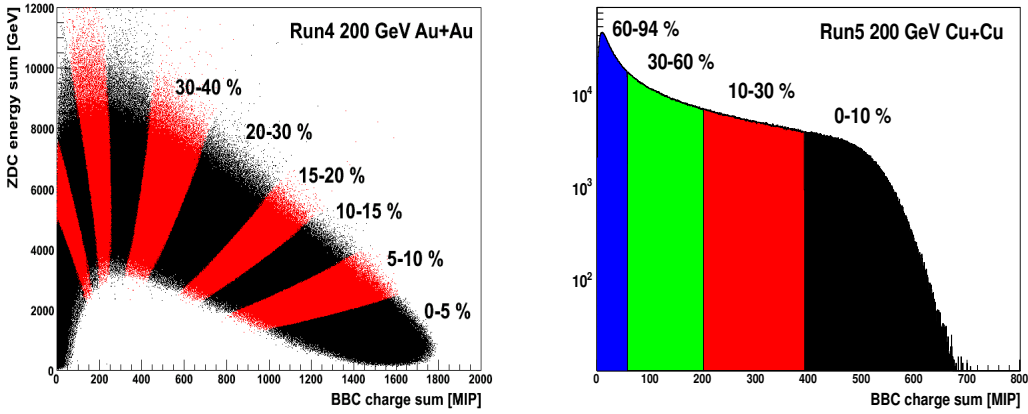


Figure 3.1: Left: ZDC energy sum vs. BBC charge sum in Run4 Au+Au collisions at $\sqrt{s_{NN}} = 200$ GeV, Right: BBC charge sum in Run5 Cu+Cu collisions at $\sqrt{s_{NN}} = 200$ GeV.

reported similar spectator neutron missing [35]. Figure 3.1 (Right) shows the charge sum of charged particles (BBC) in Run5 Cu+Cu collisions at $\sqrt{s_{NN}} = 200$ GeV. In this case, only BBC information is used for centrality determination. Before we start spectra measurements, we have finished centrality calibrations (Au+Au/Cu+Cu at $\sqrt{s_{NN}} = 200/62.4$ GeV) for common use in PHENIX.

3.1.4 Participant-Spectator Model and Glauber Model

Nucleons in heavy ion collisions can be separated into two groups : participant (the overlapped region) and spectators (the other part and keeps its longitudinal velocity). To evaluate the number of nucleon-nucleon binary collisions N_{coll} , the number of participating nucleons N_{part} , and the impact parameter b for each centrality class, we use a Glauber model Monte-Carlo simulation that includes the responses of BBC and ZDC. A participant is defined as a nucleon which has suffered at least one inelastic nucleon-nucleon collision. Systematic errors of the Glauber results are estimated by comparing results for different model assumptions. For example, in 200 GeV Au+Au case, (1) inelastic nucleon-nucleon cross section $\sigma_{NN} = 39$ mb ~ 45 mb, (2) Woods-Saxon parameters (radius: 6.38 fm \sim 6.65 fm, diffuseness: 0.53 fm \pm 0.55 fm), etc. The evaluated numbers are summarized in Tables 3.3 and 3.4 [36]. Figure 3.2 shows N_{coll} and N_{part} as a function of impact parameter for Au+Au and Cu+Cu collisions at $\sqrt{s_{NN}} = 200$ GeV. Binary-collision scaling has a strong bias towards central collisions. It is just due to nuclear overlap geometry. If we plot N_{coll} divided by $0.5N_{part}$ as a function of N_{part} (right figure), the Au+Au and Cu+Cu points are on the same line. Figures 3.3 and 3.4 show N_{part} and N_{coll} distributions for each centrality class in Au+Au/Cu+Cu collisions at $\sqrt{s_{NN}} = 200$ GeV. Even in the same centrality class, the distributions have a wide spread than expected. Because we

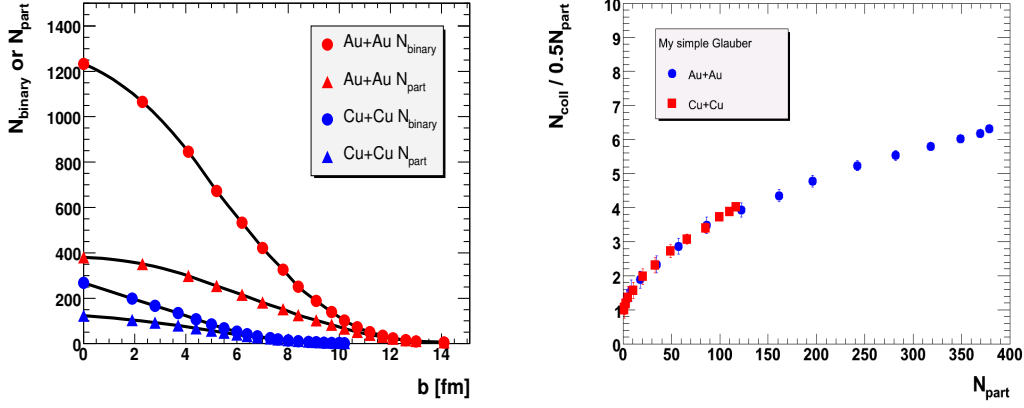


Figure 3.2: Left: N_{coll} and N_{part} as a function of impact parameter for Au+Au and Cu+Cu collisions at $\sqrt{s_{NN}} = 200$ GeV. Right: N_{coll} divided by $0.5N_{\text{part}}$ as a function of N_{part} .

select a centrality class by looking at particle multiplicities, and any multiplicity distributions have their statistical fluctuations. So we do not avoid mixing different centrality classes in N_{part} and N_{coll} under finite multiplicity condition.

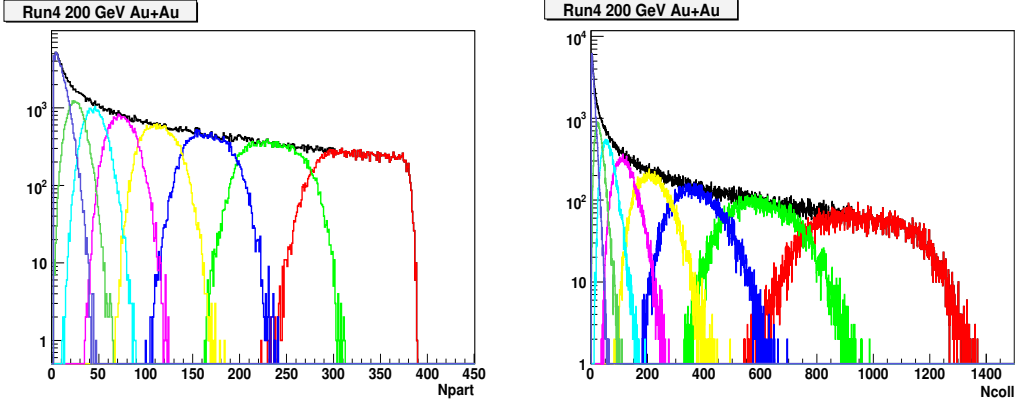


Figure 3.3: N_{part} (Left) and N_{coll} (Right) distributions for each centrality class in Au+Au collisions at $\sqrt{s_{NN}} = 200$ GeV.

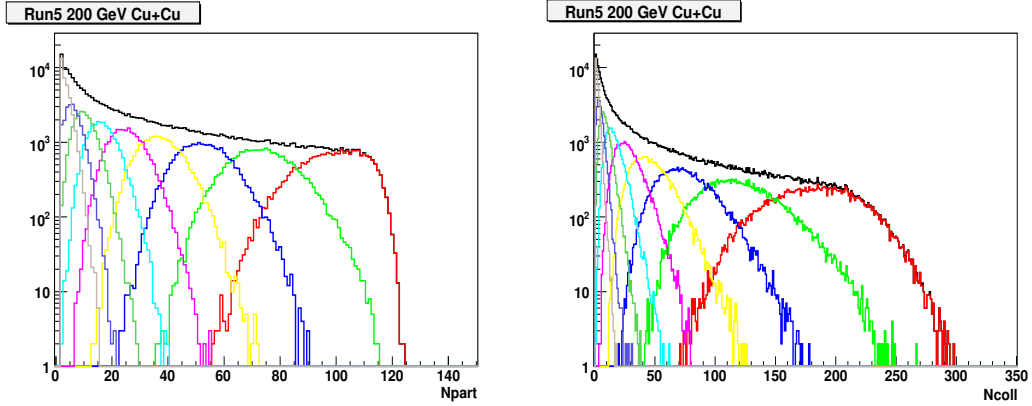


Figure 3.4: N_{part} (Left) and N_{coll} (Right) distributions for each centrality class in Cu+Cu collisions at $\sqrt{s_{NN}} = 200$ GeV.

Table 3.3: Average N_{part} , N_{coll} , b for each centrality in 200 GeV Au+Au collisions.

class [%]	$\langle N_{part} \rangle$	$\langle N_{coll} \rangle$	b [fm]
0- 10	325.2 ± 3.3	955.4 ± 93.6	3.2 ± 0.2
10- 20	234.6 ± 4.7	602.6 ± 59.3	5.7 ± 0.3
20- 30	166.6 ± 5.4	373.8 ± 39.6	7.4 ± 0.3
30- 40	114.2 ± 4.4	219.8 ± 22.6	8.7 ± 0.4
40- 50	74.4 ± 3.8	120.3 ± 13.7	9.9 ± 0.4
50- 60	45.5 ± 3.3	61.0 ± 9.9	11.0 ± 0.4
60- 70	25.7 ± 3.8	28.5 ± 7.6	11.9 ± 0.5
70- 92	9.5 ± 1.9	8.3 ± 2.4	13.5 ± 0.5

Table 3.4: Average N_{part} , N_{coll} , b for each centrality in 200 GeV Cu+Cu collisions.

class [%]	$\langle N_{part} \rangle$	$\langle N_{coll} \rangle$	b [fm]
0- 10	98.2 ± 2.4	182.7 ± 20.7	2.4 ± 0.1
10- 20	73.6 ± 2.5	121.1 ± 13.6	4.0 ± 0.2
20- 30	53.0 ± 1.9	76.1 ± 8.5	5.2 ± 0.3
30- 40	37.3 ± 1.6	47.1 ± 5.3	6.2 ± 0.3
40- 50	25.4 ± 1.3	28.1 ± 3.4	7.1 ± 0.4
50- 60	16.7 ± 0.9	16.2 ± 1.9	7.8 ± 0.4
60- 70	10.4 ± 0.6	9.0 ± 1.0	8.6 ± 0.4
70- 80	6.4 ± 0.5	4.9 ± 0.6	9.3 ± 0.5
80- 94	3.6 ± 0.3	2.4 ± 0.3	10.0 ± 0.5

Even though the N_{part} - N_{coll} relation is the same between Au+Au and Cu+Cu on the average values, the shape of overlapped colliding nuclei is different at same N_{part} as shown in Figure 3.5. Figure 3.6 (left) shows N_{part} distributions for Au+Au and Cu+Cu with same average $N_{part} \sim 117$. Cu+Cu system has a better accuracy in small N_{part} region due to small fluctuation of N_{part} itself. The right figure shows the number of binary collisions per nucleon. This reflects the nuclear thickness for each nucleon. In peripheral Au+Au collisions, the distribution is wider than in Cu+Cu collisions. A single binary collision is clearly seen for Au+Au.

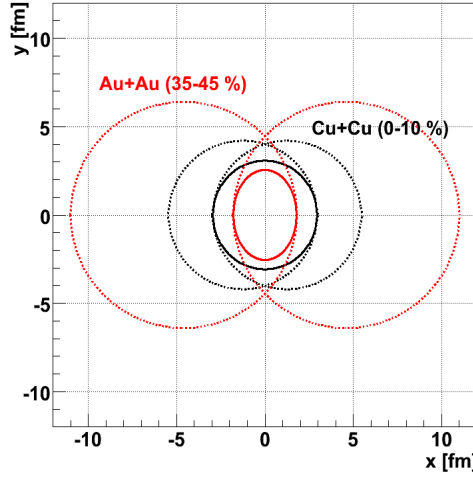


Figure 3.5: Schematic drawing of overlapped colliding nuclei for Au+Au and Cu+Cu at same $N_{part} \sim 100$.

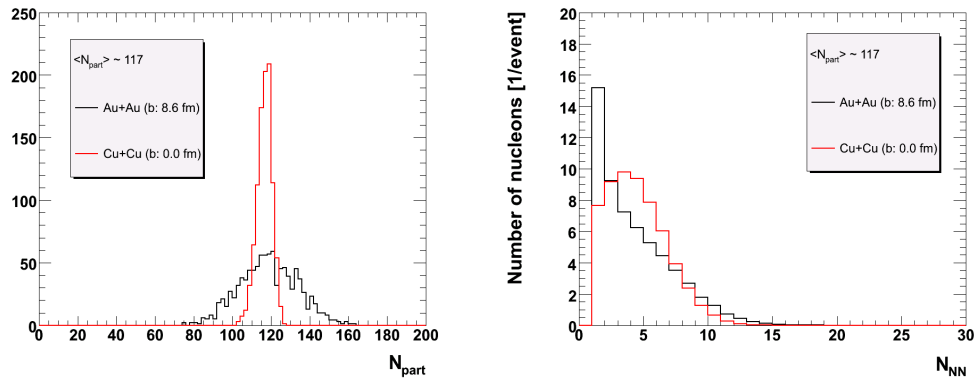


Figure 3.6: Left: N_{part} distributions for Au+Au and Cu+Cu with same average $N_{part} \sim 117$. Right: Number of binary collisions per nucleon for Au+Au and Cu+Cu with same average $N_{part} \sim 117$.

3.2 Charged Particle Measurement

3.2.1 Track Reconstruction

Charged particle tracks are reconstructed by using the hit information at DC and PC1. In the process of the reconstruction, tracks that traverse both X1 and X2 wires in DC are looked, then the remaining tracks that traverse X1 or X2 regions are looked (see Section 2.4.2). Based on a combinatorial Hough transform technique, tracks are found from the hit information of X1 and X2 wires. PC1 provides three-dimensional hit position to help pattern recognition. The reconstructed tracks are labeled by quality bits which are defined by the hit information at X1, X2, UV and PC1. This method gives the polar angle θ , azimuthal angle ϕ and bending angle α of the intersection at the DC reference radius ($R=220$ cm). Figure 3.7 shows a schematic illustration of these variables. Transverse momentum is proportional to the inverse of the bending angle α

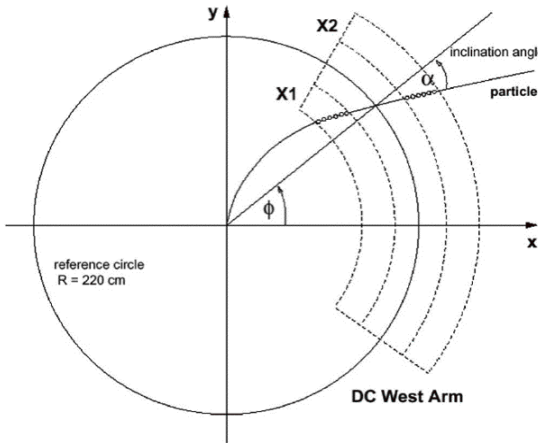


Figure 3.7: Illustration of the Hough transform variables for drift chamber track reconstruction.

for tracks emitted perpendicular to the beam axis.

$$p_T = \frac{K}{\alpha} \quad (3.1)$$

where $K=101$ mrad GeV/c is the field integral along the track trajectory. The flight path length is calculated from the reconstructed track trajectory. The DC tracking efficiency in a high multiplicity environment is estimated based on an embedding technique as explained in Section 3.8.2.

3.2.2 Track Association and Selection

Tracks reconstructed by DC-PC1 are associated with outer detectors. We find intersection points between the trajectory and outer detectors. Projected points are then matched to measured hit points. We subtract the projected position of each track from the track hit position. Then we

apply cuts on these residual distributions in both ϕ and z directions, in order to reduce the background of random track associations.

In order to do the same cut in both real and Monte Carlo (MC) data, we convert these residual distributions to normalized Gaussians and cut the same number of standard deviations in real and MC data. We obtain the mean and width of these distributions as a function of p_T for particle charge signs and north/south sides. We present a typical fitting procedure for $\Delta\phi$ distributions in Figures 3.8, 3.9, and 3.10. Double gaussian fitting is applied to decompose signal and random background parts. For Δz variable, there is a centrality (hit multiplicity in BBC region) dependence in mean and width (see Figure 3.11). The Δz resolution is worse in peripheral than in central because of lower multiplicity. We take this dependence by doing the correction for each centrality bin. We have the same corrections for the matching distributions (both $\Delta\phi$ and Δz) for TOF/PC2/PC3/EMC, and in MC similarly. After the determination of mean and width as a function of p_T , we convert these distributions to normalized Gaussians with mean=0 and sigma=1 and then reject all tracks falling outside 2 standard deviations from the mean ($\sigma_{position} \sim 8$ mm at $r = 5$ m).

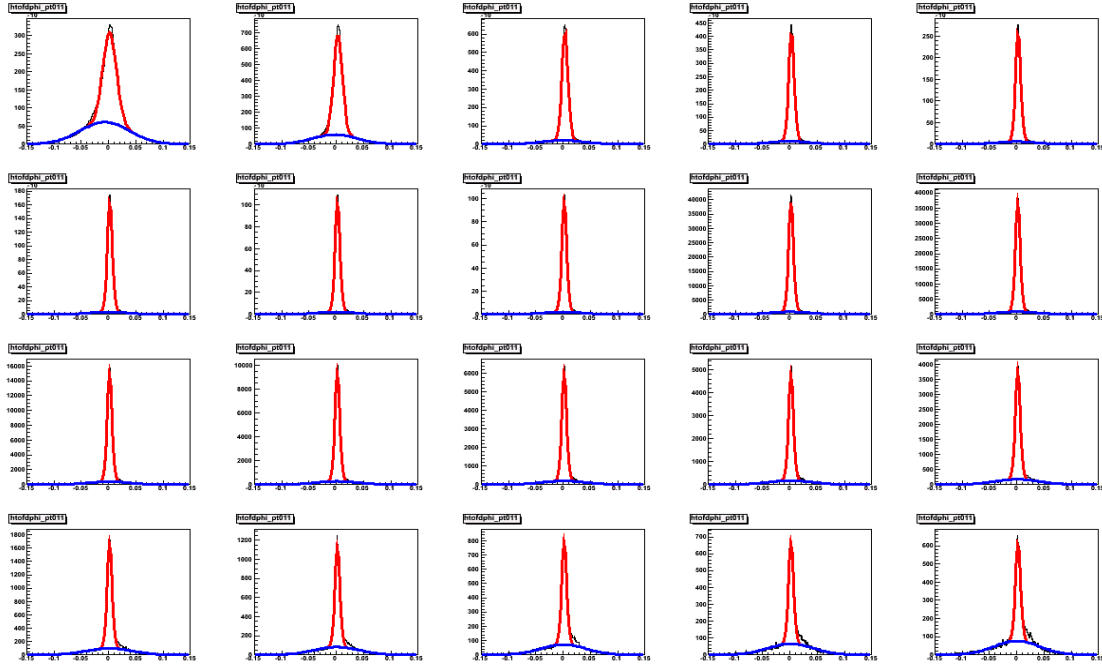


Figure 3.8: $\Delta\phi$ distributions (TOF) for each p_T range (0-4 GeV/c, 0.2 GeV/c step). Red line is signal, blue one is background.

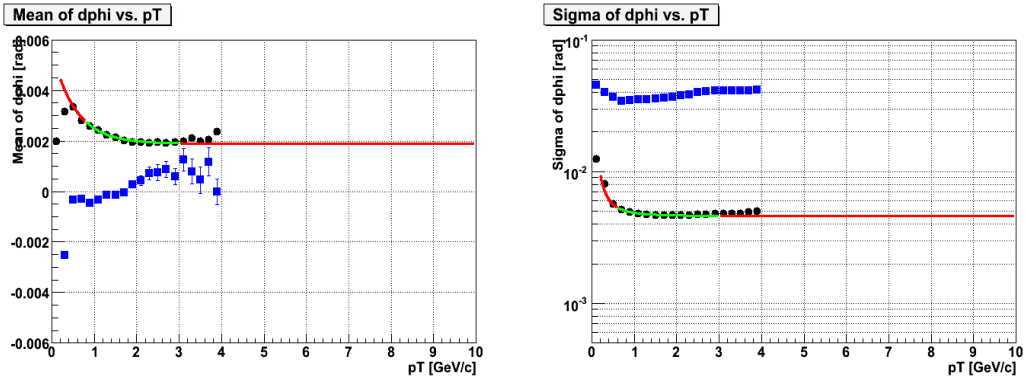


Figure 3.9: Mean (left) / Sigma (right) of TOF $\Delta\phi$ as a function of p_T . Black marker is signal, blue one is background. Red line is a parameterization.

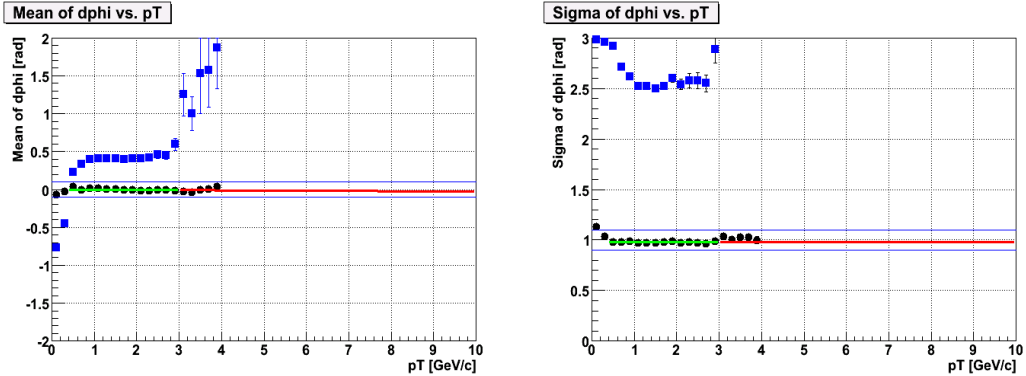


Figure 3.10: Normalized mean (left) / sigma (right) of TOF $\Delta\phi$ as a function of p_T . Black marker is signal, blue one is background. Red line is a constant-value fit.

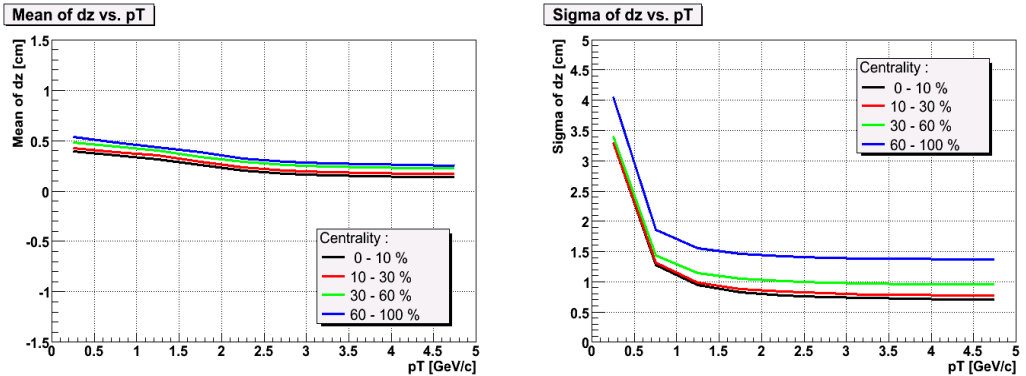


Figure 3.11: Mean (left) / Sigma (right) of PC3 Δz as a function of p_T for different centrality bins.

3.3 Event and Track Selection Cuts

The event and track cut conditions used in the analysis are summarized below. Most of the cuts are commonly used in the past identified charged hadron analyses in PHENIX. And we also used the same (or equivalent) cuts over the single-particle Monte Carlo simulation to obtain correction factors. The PHENIX common recalibrator called MasterRecalibrator is used to apply (re)calibrations for TOF (Time-of-Flight counter), ACC (Aerogel Cherenkov counter), and other detectors including track matching and centrality.

Common cuts for TOF and ACC analyses:

- Trigger : Minimum bias trigger (Non-physics bunch crossing events removed)
- BBC Z vertex cut : < 30 cm
- DC Z position cut : < 75 cm

ACC specific cuts:

- DC track quality : 31 or 61 or 62 or 63
- PC2/PC3/EMC Matching cut : 2σ in ϕ and z directions (with correction)
- PID cut : Requiring ACC information (Fire or Veto) with fixed N_{pe} threshold.
(6 pe (sum) unless otherwise specified. Overflow tracks are excluded (see Section 3.8.2).)
- Fiducial cut : (see text)

TOF specific cuts:

- DC track quality : 31 or 63
- TOF Matching cut : 2σ in ϕ and z directions (with correction)
- PC3 Matching cut : None
- PID cut : Use isPi, isK, isP variables (after PidrecalReco),
(2σ selection and 2σ veto of other particle types,
and requiring $m^2 > 0.6$ for (anti)proton.)
- TOF slat cut : None
- Eloss cut : β -dependent energy loss cut
- Fiducial cut : (see text)

3.4 Quarility Assurance - run-by-run stability check

We have checked the run-by-run detector stability by looking at m^2 distributions, raw p_T spectra and fiducial area in DC ϕ vs. charge/momentum space. Figure 3.12 shows a typical example of run-by-run quality check display. Figures 3.13 and 3.14 show the run-number dependences

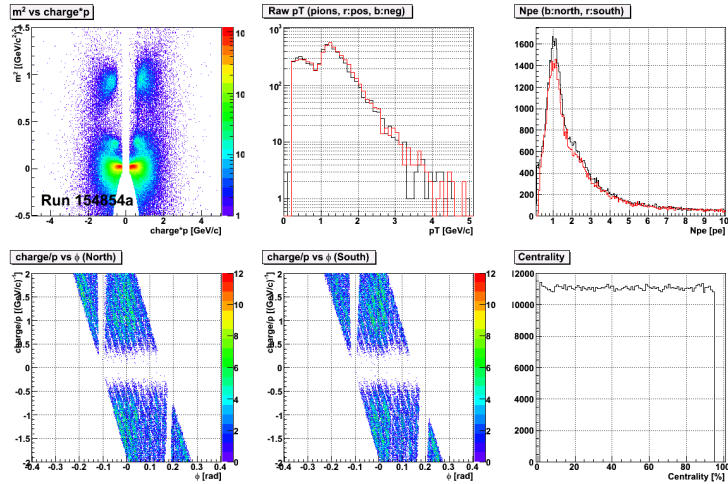


Figure 3.12: Run-by-run quality check (ACC) for Run 154854 (top left: m^2 vs. charge $\times p$, top middle: raw p_T distribution, top right: N_{pe} distribution, bottom left: charge/ p vs. ϕ (north), bottom middle: charge/ p vs. ϕ (south), bottom right: centrality distribution).

of mean and sigma of ACC- N_{pe} and the raw number of tracks per event (pions) for ACC and TOF. A switch in yield around Run 155800 corresponds to the change of magnetic field direction. We select run numbers to obtain uniform detector response. Run numbers which have a small statistics, or bad centrality distribution are also excluded in the analysis. With the run-by-run check, we made the good run number lists. Note that ACC in Run5 Cu+Cu (++) phase looks unstable. This is due to instability of drift chamber (W1 sector) in front of ACC. We applied very tight fiducial cut to remove this unstable region.

3.5 Particle Identification

3.5.1 Time of Flight Counter

The Time-of-Flight counter has a timing resolution of 120 ps. The overall timing resolution including BBC timing resolution is ~ 130 ps for Au+Au/Cu+Cu, and ~ 140 ps for p+p. Particle identification (PID) is based on particle mass calculated from measured momentum, time of flight and path length along the trajectory. It can be used for (anti)proton identification up to $p_T = 4$ GeV/c. The PID cut is 2σ selection and 2σ veto of other particle types. For the upper momentum cut off, we use 3 GeV/c, 2 GeV/c, and 4 GeV/c for pions, kaons, and protons, respectively. The

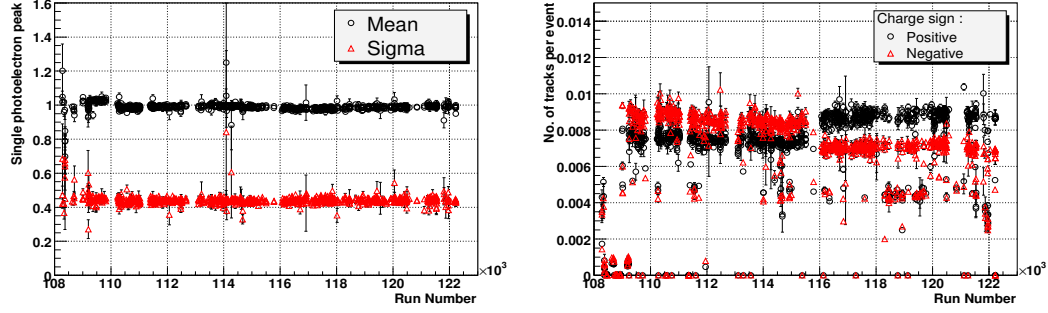


Figure 3.13: Left: Mean/Sigma of photoelectron peak (ACC) vs. Run Number, Right: Number of tracks per event (positive/negative, ACC) vs. Run Number.

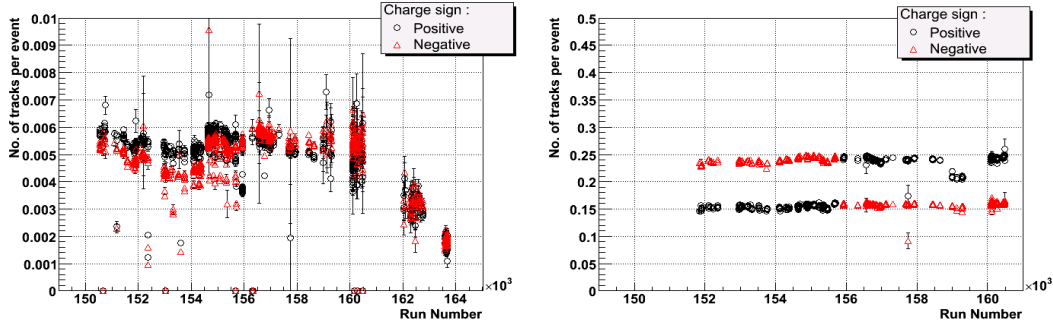


Figure 3.14: Left: Number of tracks per event (ACC) vs. Run Number (including Run5 Cu+Cu 62 GeV and 22 GeV phases), Right: Number of tracks per event (TOF) vs. Run Number.

main reason is to reduce other-particle contamination. For the lower momentum cut off, we use 0.5 GeV/c. Figure 3.15 shows mass squared vs. charge \times momentum distribution for TOF (real data, Minimum bias). Mean m^2 are fitted with a constant value for each particle species. Sigma m^2 values are parameterized with the following function:

$$\sigma_{m^2}^2 = \frac{\sigma_\alpha^2}{K_1^2} (4m^4 p^2) + \frac{\sigma_{ms}^2}{K_1^2} \left[4m^4 \left(1 + \frac{m^2}{p^2} \right) \right] + \frac{\sigma_{TOF}^2 c^2}{L^2} [4p^2(m^2 + p^2)] \quad (3.2)$$

where p is momentum, m is particle mass, σ_α is angular resolution in [mrad], σ_{ms} is multiple scattering term, σ_{TOF} is overall TOF resolution and K_1 is the field integral value. This parameterization is done for $\pi/K/p$ simultaneously (see Figures 3.16 and 3.17). In peripheral events, a deviation of m^2 mean is seen due to slightly wrong calibrations since TOF timing calibration was done for Minimum bias events. Taking care of this centrality dependence, we apply different PID boundaries for each centrality bin.

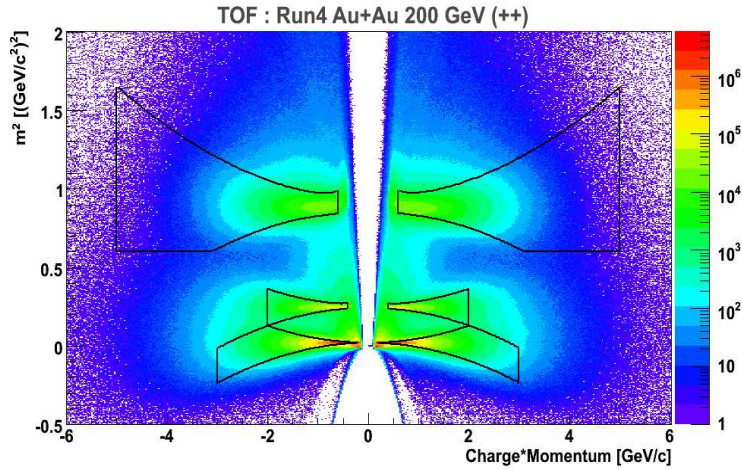


Figure 3.15: m^2 vs. charge \times p distribution (TOF, Real data) with PID boundaries.

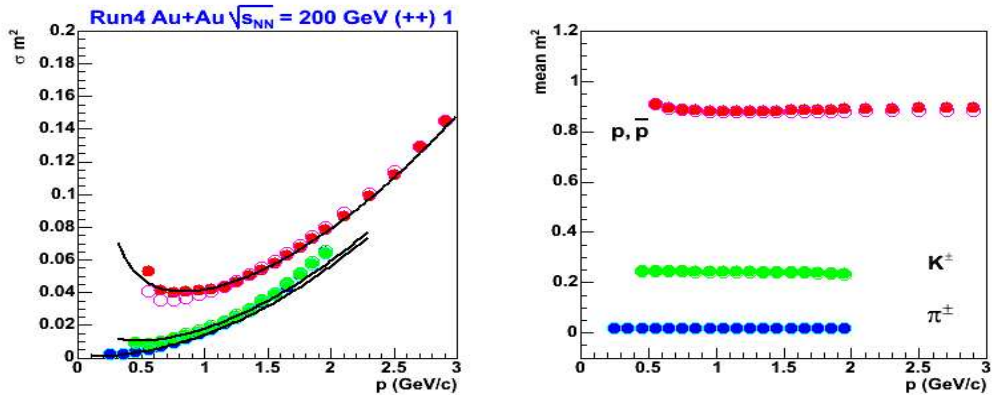


Figure 3.16: m^2 sigma (left) and mean (right) vs. momentum for real data (TOF).

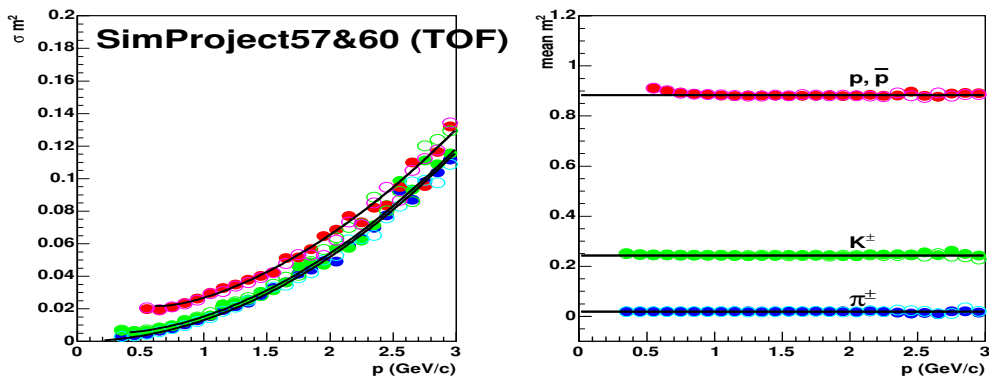


Figure 3.17: m^2 sigma (left) and mean (right) vs. momentum for MC data (TOF).

3.5.2 Aerogel Cherenkov Counter

The Aerogel Cherenkov counter has a refractive index of $n = 1.011$. This corresponds to 0.9 GeV/c, 3.3 GeV/c, 6.3 GeV/c threshold values in momentum for pions, kaons, and protons, respectively. The aerogel counter has 320 readout channels (from Run5, just half in Run4) in total. Calibration constants are single photoelectron peak and pedestal values for each channel. Both collision data and LED-calibration data are available for the calibration. The calibration constants can be touched through the recalibration module. On the other hand, the response in Monte Carlo (MC) is tuned to adjust mean and sigma values of the number of photoelectrons to that in real data (see Figures 3.18 and 3.19). Aerogel signal is required for either case, fire (for

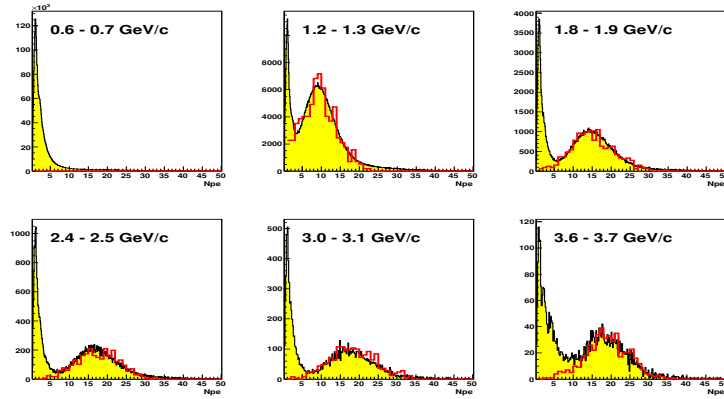


Figure 3.18: Momentum-sliced N_{pe} distributions (ACC). Red histograms are from MC pions.

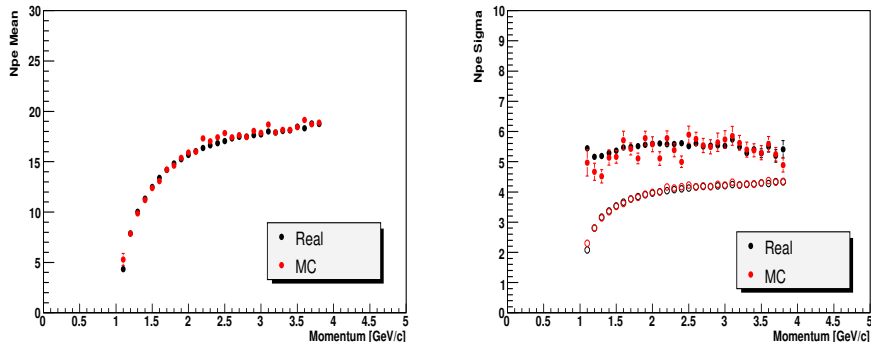


Figure 3.19: Left: Mean of N_{pe} vs. momentum ($N_{pe} \propto (1 - 1/(n\beta)^2)$), Right: Sigma of N_{pe} vs. momentum. Open symbols are square root of N_{pe}^{mean} .

pions) or veto (not fired, for protons) with the fixed number of photoelectrons (N_{pe}) threshold. The N_{pe} threshold is tested with changing the values. The purpose is to check the contamination like kaons to protons. The contamination is subtracted by looking at m^2 distribution from EMCAL. Figures 3.20 and 3.21 show N_{pe} as a function of momentum in Real and MC. Figure 3.22 shows time of flight (EMCal) vs. $1/p$ under ACC veto condition. A clear proton peak is seen up to high p_T .

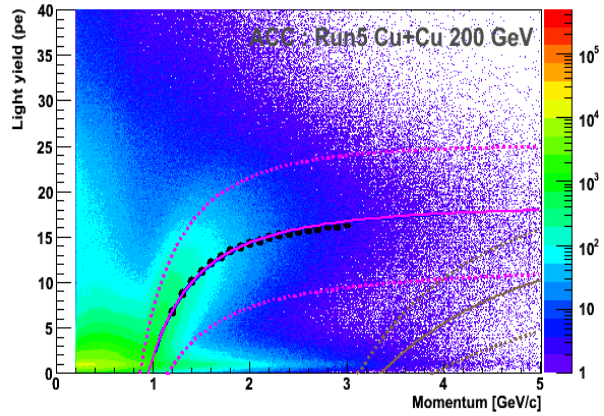


Figure 3.20: Number of photoelectrons as a function of momentum (ACC, Real data). The lines show expected response from fitting for pions and kaons.

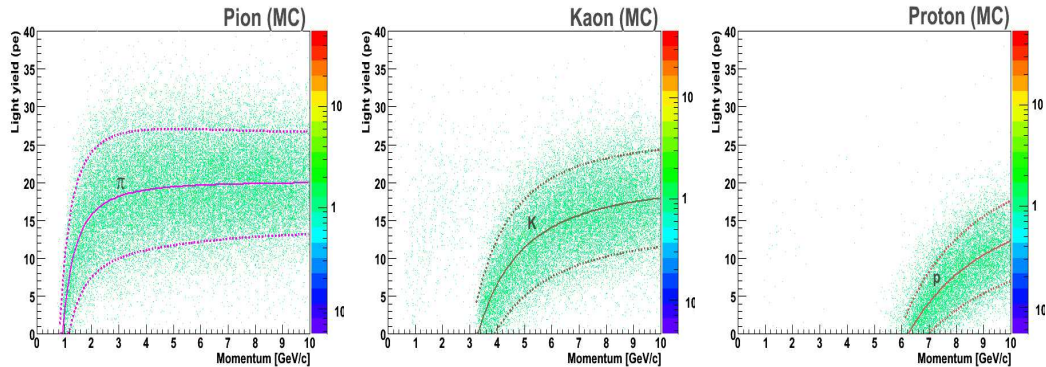


Figure 3.21: Number of photoelectrons as a function of momentum (ACC, MC). The lines are from fitting.

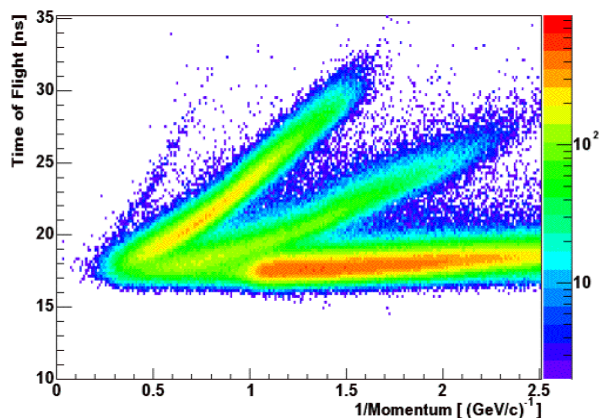


Figure 3.22: Time of flight (EMCal) vs. $1/p$ under ACC veto condition.

3.5.3 Particle Contamination

Particle contamination in TOF PID

To estimate the fraction of pion/kaon contamination in proton, mass squared distributions are fitted with triple gaussian function ($\pi/K/p$) for each p_T range (see Figure 3.23). Mean and sigma m^2 values of those gaussian functions are fixed at the extrapolated ones from low- p_T measurement and its expectations (see Section 3.5.1). Another fitting method is tried to reproduce actual distributions. When looking at m^2 distribution at high p_T , the distribution has a long tail on the right side of proton peak. This tail is a feed-down effect (like $\Lambda \rightarrow p + \pi$) [37]. The BG function (actually not BG, this is proton from weak decay with slightly different m^2) is introduced to take account of the tail (see Figure 3.24). The contamination ratio of pion+kaon to proton is estimated within 2σ of proton m^2 and $m^2 > 0.6 \text{ GeV}^2/\text{c}^4$ for combinations of fitting methods, charge signs, centrality classes.

$$\text{contamination ratio} = \frac{\text{pion}_{|\sigma|<2} + \text{kaon}_{|\sigma|<2}}{\text{pion}_{|\sigma|<2} + \text{kaon}_{|\sigma|<2} + \text{proton}_{|\sigma|<2}} \quad (3.3)$$

or,

$$\text{contamination ratio} = \frac{\text{pion}_{|\sigma|<2} + \text{kaon}_{|\sigma|<2}}{\text{pion}_{|\sigma|<2} + \text{kaon}_{|\sigma|<2} + \text{proton}_{|\sigma|<2} + \text{BG}_{|\sigma|<2}} \quad (3.4)$$

The ratios are plotted as a function of p_T in Figures 3.26 ~ 3.27. These values are used as correction factors to calculate final spectra.

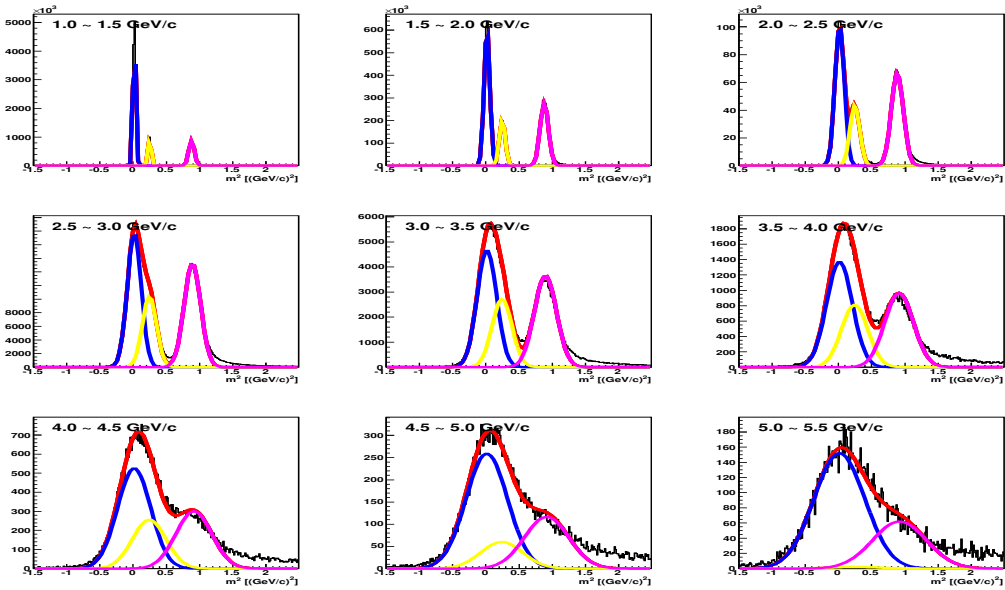


Figure 3.23: m^2 distributions with triple gaussian fitting (positive $\pi/K/p$) in Run4 200 GeV Au+Au MB. Blue: pions, yellow: kaons, magenta: protons, red: total.

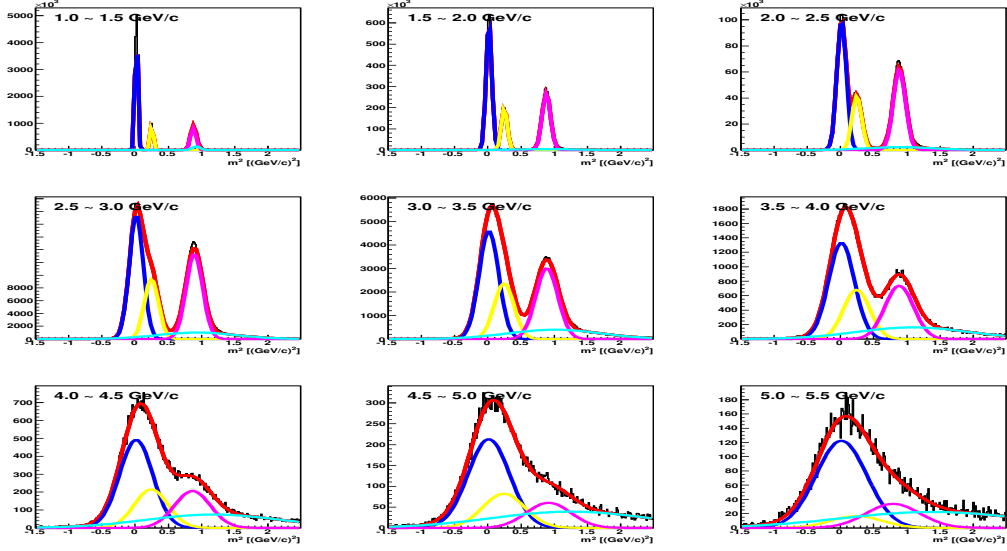


Figure 3.24: m^2 distributions with triple gaussian fitting (positive $\pi/K/p$) in Run4 200 GeV Au+Au MB. Gaussian BG tail is included. Blue: pions, yellow: kaons, magenta: protons, sky blue: BG (feed-down), red: total.

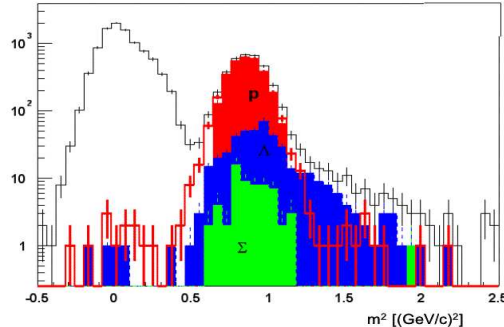


Figure 3.25: m^2 distributions for positive particles ($2.5 < p_T < 3.0$ GeV/c) [37]. The contribution of protons from feed-down decays is shown.

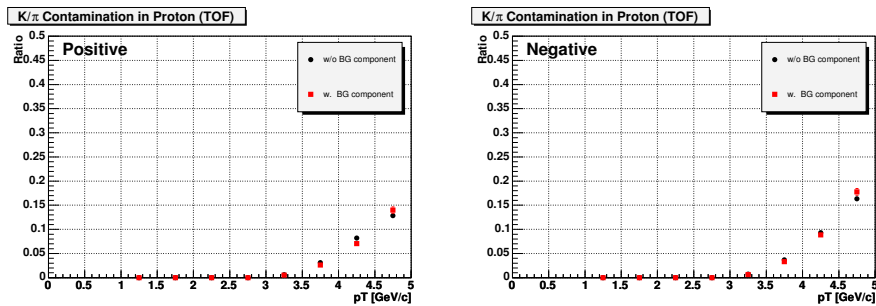


Figure 3.26: Pion/Kaon contamination ratio in proton as a function of p_T for each fitting method (left: positive, right: negative) (Run4 200 GeV Au+Au).

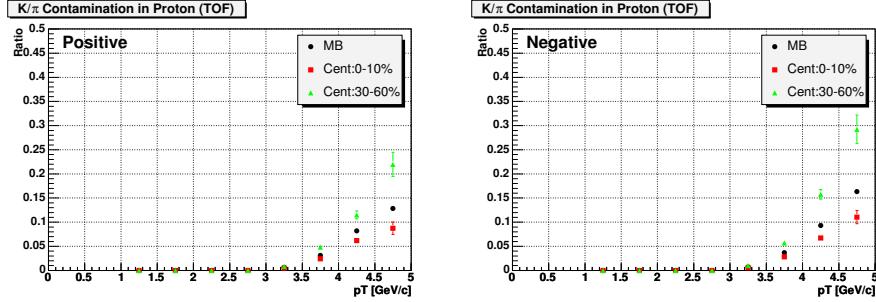


Figure 3.27: Pion/Kaon contamination ratio in proton as a function of p_T for each centrality class (left: positive, right: negative) (Run4 200 GeV Au+Au).

Particle contamination in ACC PID

To estimate the fraction of kaon contamination in proton, mass squared distributions (EMCal behind ACC) are fitted with double gaussian function (kaon and proton) for each p_T range (see Figure 3.28). Mean and sigma m^2 values of those gaussian functions are fixed at the extrapolated ones from low- p_T measurement and its expectations. All the fittings are done in the condition of ACC-Veto. So, pion component is suppressed and mostly invisible for all p_T range. Only in top-left figure (1.0-1.5 GeV/c), pion peak can be seen. Two fitting methods are tried to reproduce actual distributions. One method is with background (BG) component. As in TOF, the BG (feed-down) function is introduced to take account of the tail (see Figure 3.29). Since significant bend as a function of momentum for antiproton m^2 mean is seen, peak position of antiproton m^2 at high p_T has some uncertainties. We try fitting with introducing mean of antiproton m^2 as an additional free parameter. This is the other fitting method. The contamination ratio of kaon to proton is estimated within 2σ of proton m^2 for combinations of fitting methods, charge signs, centrality classes.

$$\text{contamination ratio} = \frac{\text{kaon}_{|\sigma|<2}}{\text{kaon}_{|\sigma|<2} + \text{proton}_{|\sigma|<2}} \quad (3.5)$$

or,

$$\text{contamination ratio} = \frac{\text{kaon}_{|\sigma|<2}}{\text{kaon}_{|\sigma|<2} + \text{proton}_{|\sigma|<2} + \text{BG}_{|\sigma|<2}} \quad (3.6)$$

The ratios are plotted as a function of p_T in Figures 3.30 ~ 3.31. These values are used as correction factors to calculate final spectra.

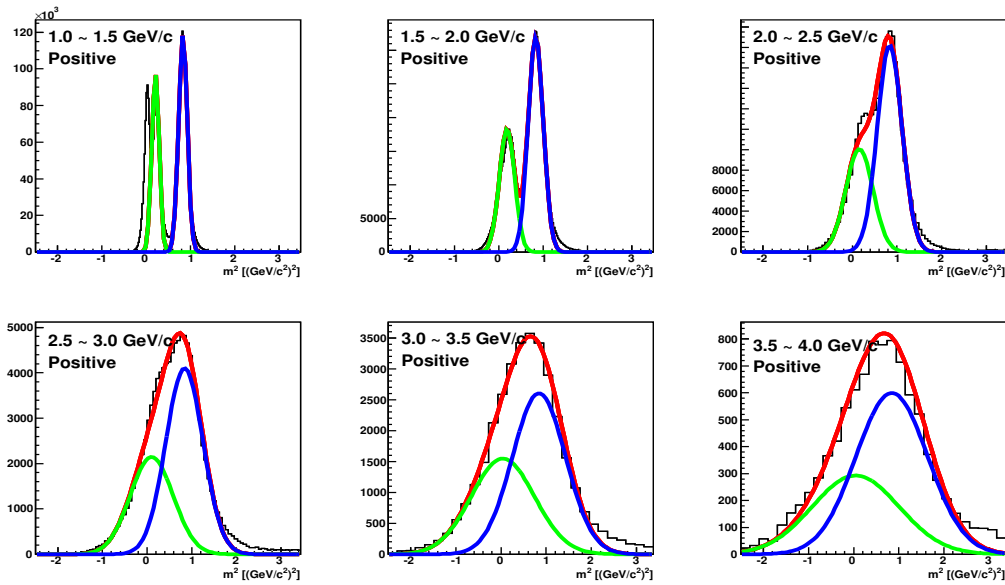


Figure 3.28: Mass squared distributions (positive) under ACC-Veto condition with double gaussian fitting (Run4 200 GeV Au+Au). Green: kaons, blue: protons, red: total.

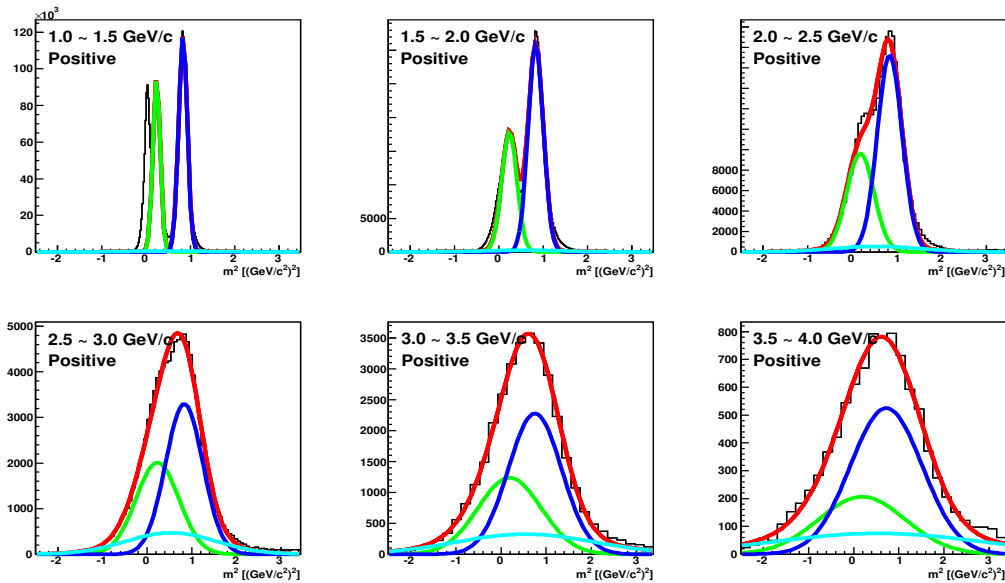


Figure 3.29: Mass squared distributions under (positive) ACC-Veto condition with double gaussian fitting (Run4 200 GeV Au+Au). Gaussian BG tail is included. Green: kaons, blue: protons, sky blue: BG (feed-down), red: total.

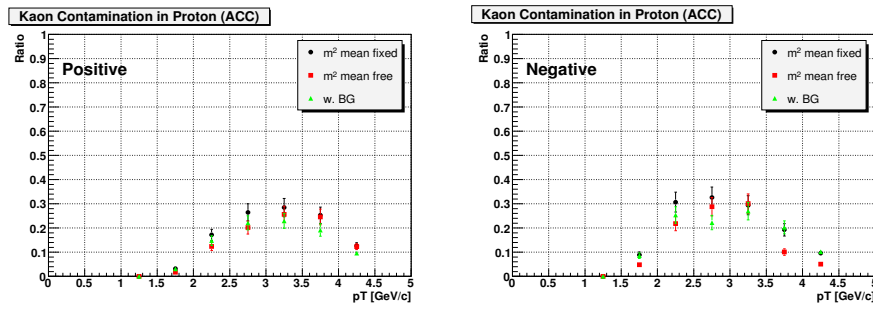


Figure 3.30: Kaon contamination ratio in proton (ACC-Veto) as a function of p_T for each fitting method (left: positive, right: negative) (Run4 200 GeV Au+Au).

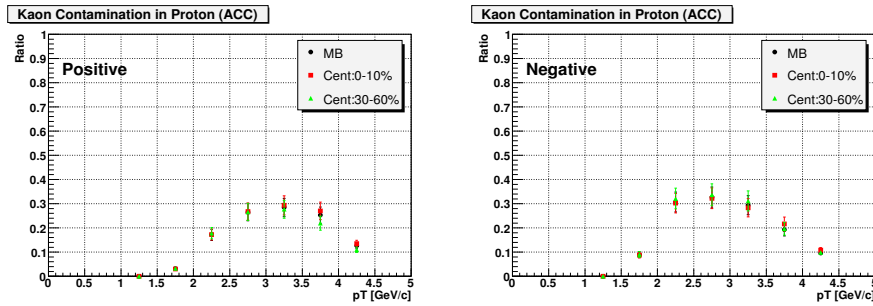


Figure 3.31: Kaon contamination ratio in proton (ACC-Veto) as a function of p_T for each centrality class (left: positive, right: negative) (Run4 200 GeV Au+Au).

3.6 Background Subtraction

At high p_T , S/N ratio of charged track association is decreased due to several backgrounds. Background (BG) components are, for example, decayed hadrons, electrons/positrons from photon conversion, or random track association. A sketch of tracks is shown in Figure 3.32 (left). Those are mis-reconstructed as higher- p_T track than actual one [38]. The point to be kept in mind is that p_T spectra is steep in any case, so BG produced at low- p_T can affect high- p_T part more significantly. To subtract such BG components, residual bending in ϕ direction can be used [38]. Due to fringe magnetic field, decayed products or electrons/positrons are bended in ϕ direction. Actual track at high p_T has a straight line to outer detectors. Its matching residual is sitting around zero with tracking resolution. Positive and negative BG has opposite bending direction. Monte Carlo study was also done to confirm the shape of residual distribution (see Figure 3.32 (right)).

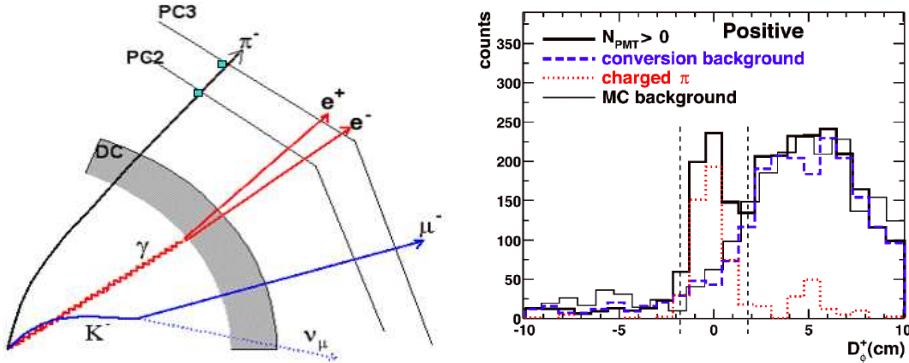


Figure 3.32: Left: Sketch of tracks with photon conversion, particle decay. Right: $\Delta\phi$ distribution with background electrons from MC simulation.

Background Subtraction in TOF

S/N ratio at high p_T is estimated by using TOF residual matching distributions. The residual distributions are fitted with double gaussian function to separate signal and background parts after applying all other cuts (see Figure 3.33). Then, S/N ratio is estimated within 2 sigma range with the fitted results. S/N ratios are plotted as a function of p_T in Figure 3.34. In case of Proton-ID, the S/N ratio is better compared to No-PID case. The S/N ratios are used as correction factors to calculate final spectra.

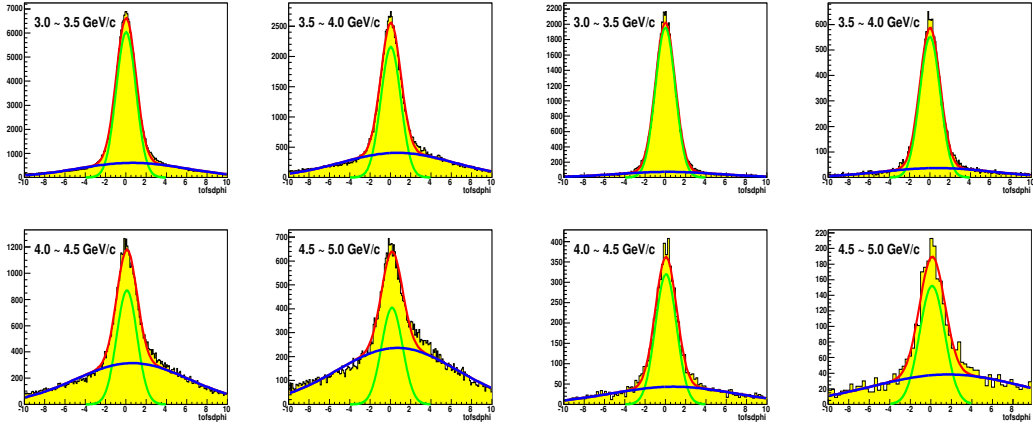


Figure 3.33: Track matching residual distributions (normalized TOF $\Delta\phi$, positive) for each p_T range (Run4 200 GeV Au+Au) (left: No-PID, right: Proton-ID).

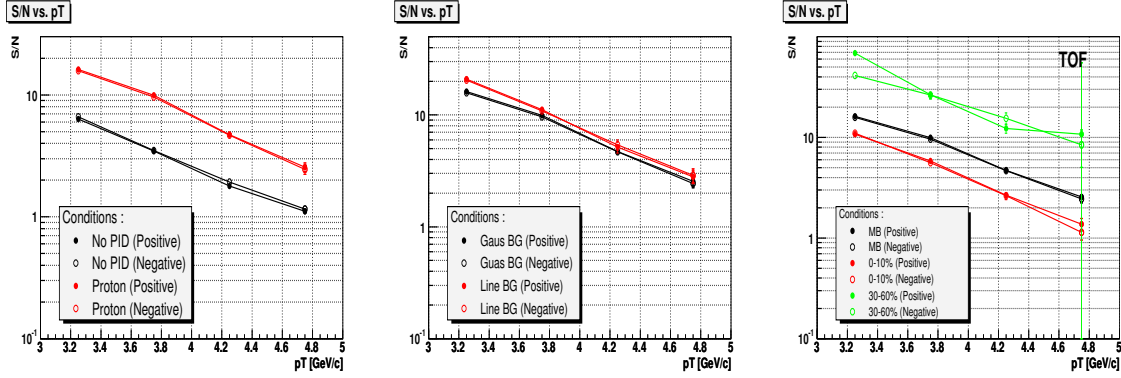


Figure 3.34: S/N ratio as a function of p_T (Run4 200 GeV Au+Au) (left: PID condition, middle: BG fitting function, right: centrality class).

Background Subtraction in ACC

PC2/PC3 matching residual distributions are fitted with double gaussian function or “gaussian + straight line” function to separate signal and background parts after applying all other cuts. Then, S/N ratio is estimated within 2 sigma range with the fitted results for combinations of cut conditions (No-ACC-Cut/ACC-Fired/ACC-Not-Fired), charge signs, and centrality classes (see Figures 3.35 ~ 3.36). In case of ACC-Not-Fired, the S/N ratio is worse compared to the other two cases because of not confirming signal by itself. S/N ratios are plotted as a function of p_T in Figure 3.37. The S/N ratios are used as correction factors to calculate final spectra.

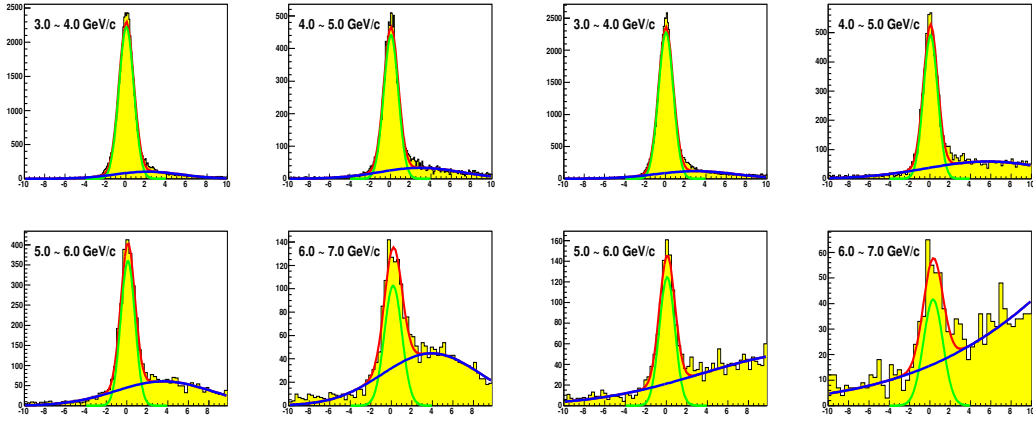


Figure 3.35: Track matching residual distributions $((\text{PC2 } \Delta\phi + \text{PC3 } \Delta\phi)/2$, positive, double gaus) for each p_T range (Run4 200 GeV Au+Au) (left: ACC-Fired, right: ACC-Not-Fired).

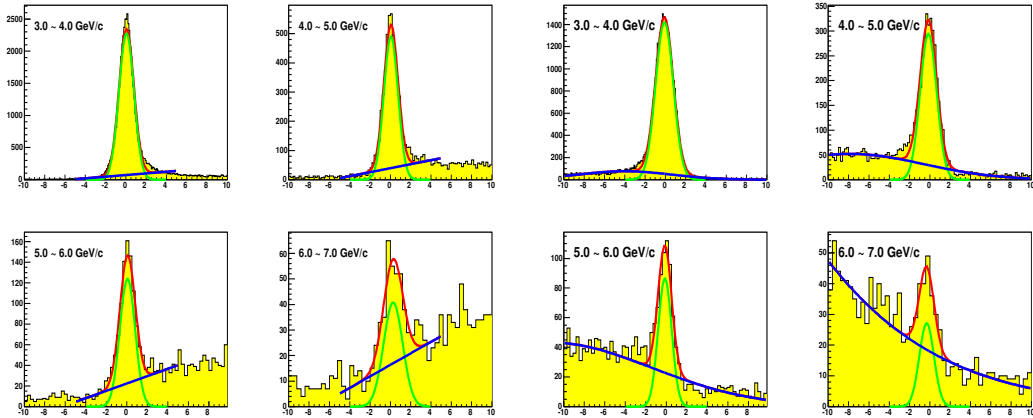


Figure 3.36: Track matching residual distributions $((\text{PC2 } \Delta\phi + \text{PC3 } \Delta\phi)/2)$ under ACC-Not-Fired condition for each p_T range (Run4 200 GeV Au+Au) (left: positive/gaus+line, right: negative/gaus+gaus).

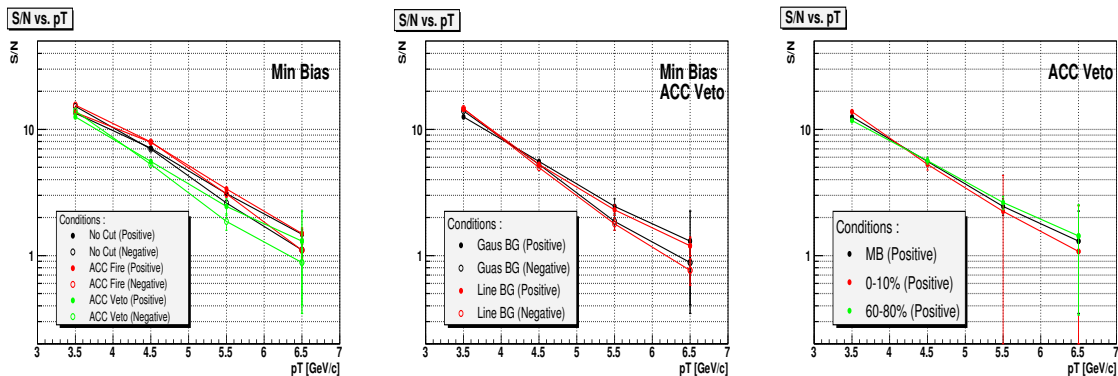


Figure 3.37: S/N ratio as a function of p_T (Run4 200 GeV Au+Au) (left: PID condition, middle: BG fitting function under ACC-Not-Fired, right: centrality class).

3.7 Fiducial Cut

Fiducial cut is introduced in order to keep uniform acceptance thorough the run duration and to match the fiducial area in real data with that in Monte Carlo (MC) simulation for acceptance corrections. The exactly same fiducial cut on DC ϕ and charge/ p space is applied in both real data and MC. The applied fiducial area is shown in Figures 3.38 ~ 3.40.

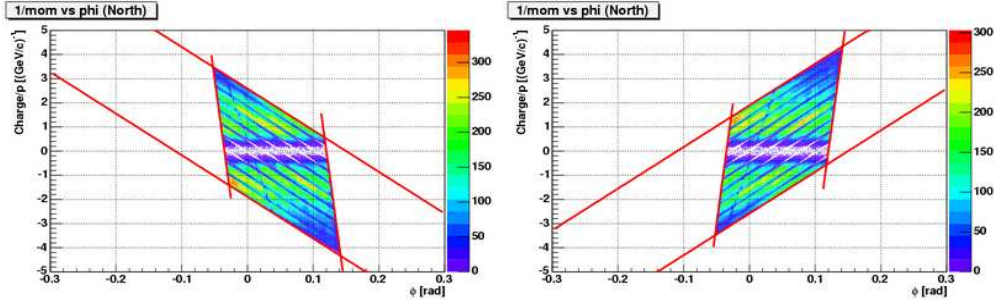


Figure 3.38: Charge/ p vs. ϕ plane (ACC North, Run4 real). Left: $++$ field, Right: $--$ field.

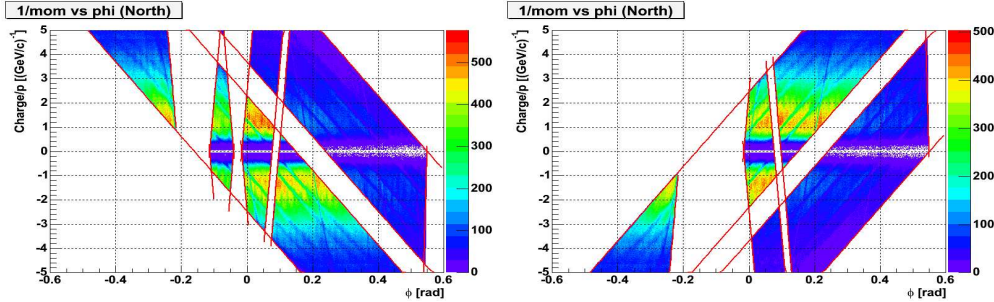


Figure 3.39: Charge/ p vs. ϕ plane (TOF North, Run4 real). Left: $++$ field, Right: $--$ field.

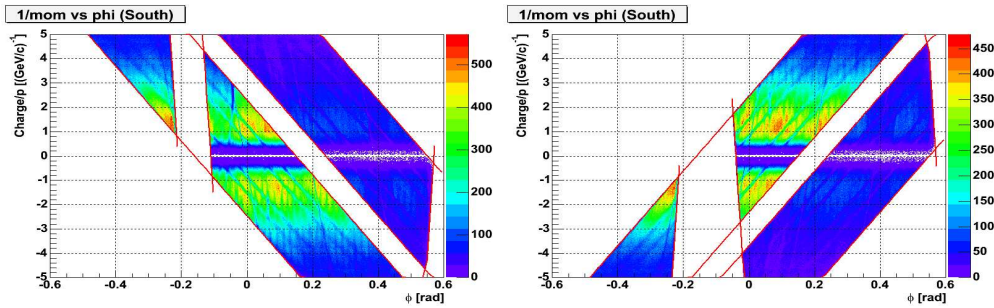


Figure 3.40: Charge/ p vs. ϕ plane (TOF South, Run4 real). Left: $++$ field, Right: $--$ field.

In Figures 3.41 ~ 3.42, y-z (ϕ -z) distributions in ACC (TOF) with a track momentum larger than 2 GeV/c are presented. Those are projected into y (ϕ) and z direction each, and compared with MC distributions. The notch in TOF E0 sector is a known lack, that is removed in MC. The agreement is roughly good and we do not have care anymore. The remaining difference is taken into account as systematic error. For ACC, to eliminate the edge of each cell which has a low detection efficiency, we apply very tight fiducial cut cell-by-cell, that is, a removal of the outer 2 cm area of the cell as shown in Figure 3.41.

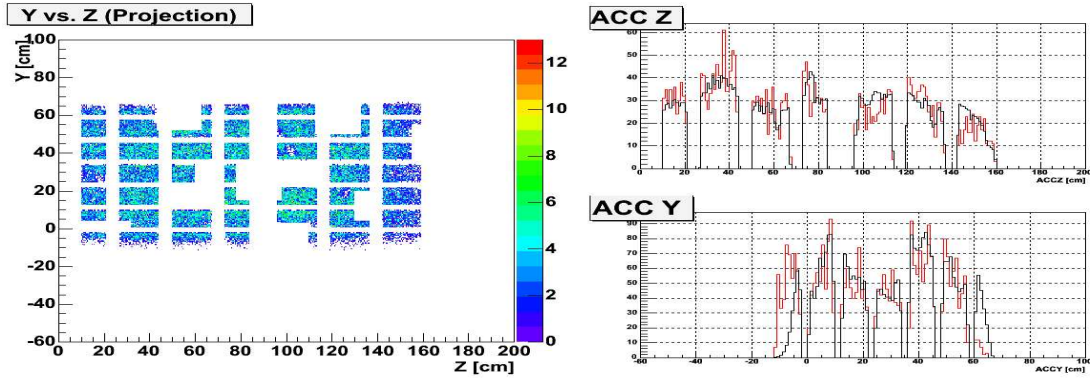


Figure 3.41: Radio graph and its projected distributions (Black: Run4 real, Red: MC) for ACC (++ field).

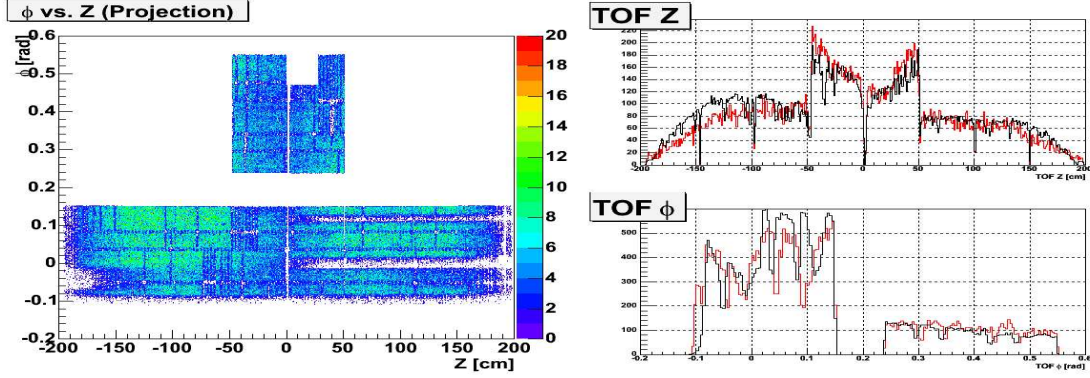


Figure 3.42: Radio graph and its projected distributions (Black: Run4 real, Red: MC) for TOF (++ field).

3.8 Monte Carlo Correciton

3.8.1 Spectra Correction

To evaluate correction factors, we use a single-particle GEANT Monte Carlo simulation including PHENIX event reconstruction process called PISA (PHENIX Integrated Simulation Application). Single-particle Monte Carlo files are prepared for $\pi/K/p$ species under each magnetic field configuration. The correction includes: geometrical acceptance, decay in flight, multiple scattering, tracking efficiency and momentum resolution. A correction factor can be calculated using INPUT p_T distribution and OUTPUT p_T distribution. The correction factor is estimated by dividing OUTPUT with INPUT for each p_T bin. Figures 3.43 and 3.44 show the evaluated correction factors as a function of p_T for ACC and TOF.

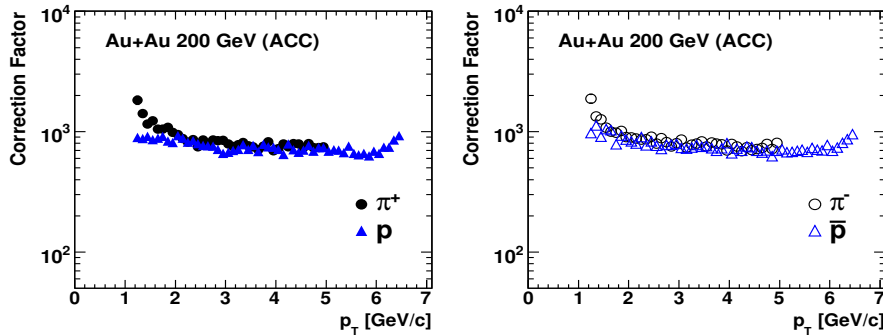


Figure 3.43: Correction factors as a function of p_T (ACC, Run4 200 GeV Au+Au).

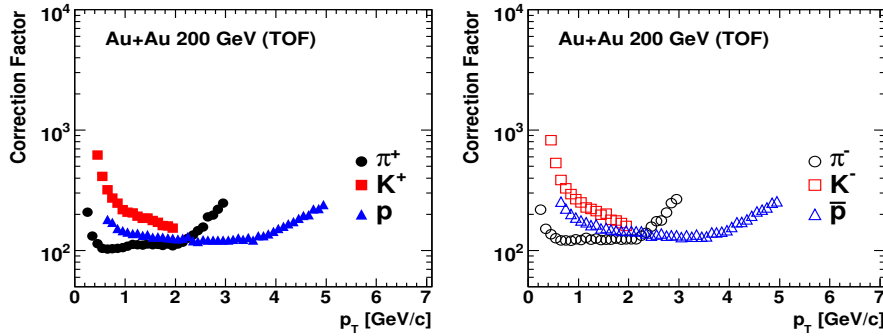


Figure 3.44: Correction factors as a function of p_T (TOF, Run4 200 GeV Au+Au).

3.8.2 Multiplicity-dependent Efficiency Correction

In high multiplicity environment like heavy ion collisions, tracking efficiency is reduced due to detector occupancy effect. To obtain multiplicity-dependent detector efficiency, we estimate the effect of detector occupancy by embedding single Monte Carlo (MC) track into real event. The multiplicity-dependent efficiency is calculated as $\epsilon_{embed} = N_{embed}/N_{single}$ where N_{embed} is the

number of single MC tracks which passed cuts (including PID and others) in embedding real event, and N_{single} is the number of single Monte-Carlo tracks which passed the cuts in single MC event. Multiplicity-dependent efficiencies as a function of centrality are calculated as shown in Figure 3.45. The p_T dependence on efficiencies are found to be small. For TOF, we use the numbers in Run2 200 GeV Au+Au analysis [37]. For Cu+Cu at 200 GeV, number-of-participants scaling is applied to adjust different centrality selection. Since ACC is a new detector from Run4, we estimate the efficiencies by the embedding method. Figure 3.46 (left) shows overflow rate as a function of centrality. Figure 3.46 (right) is 2D radiograph after excluding overflow tracks. Dark spots of this figure shows that overflow is coming from direct track passing in PMT.

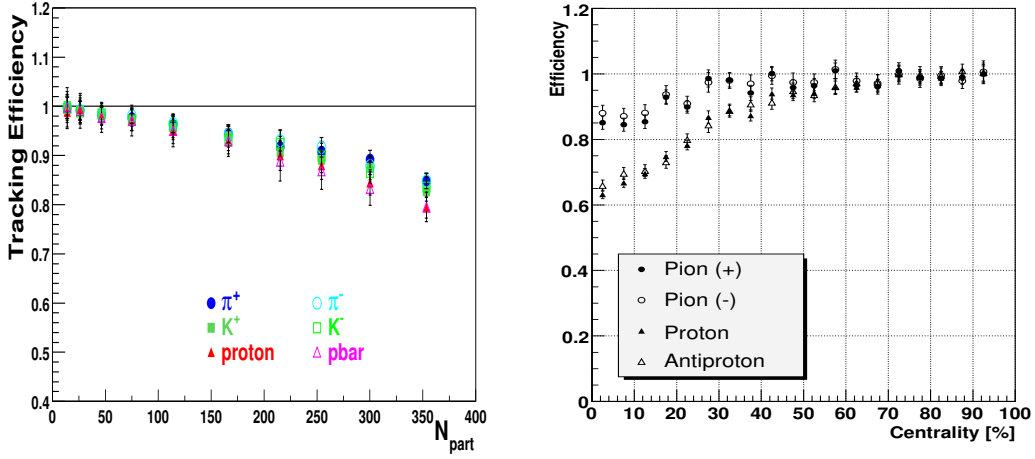


Figure 3.45: Multiplicity-dependent efficiency (left: TOF, right: ACC).

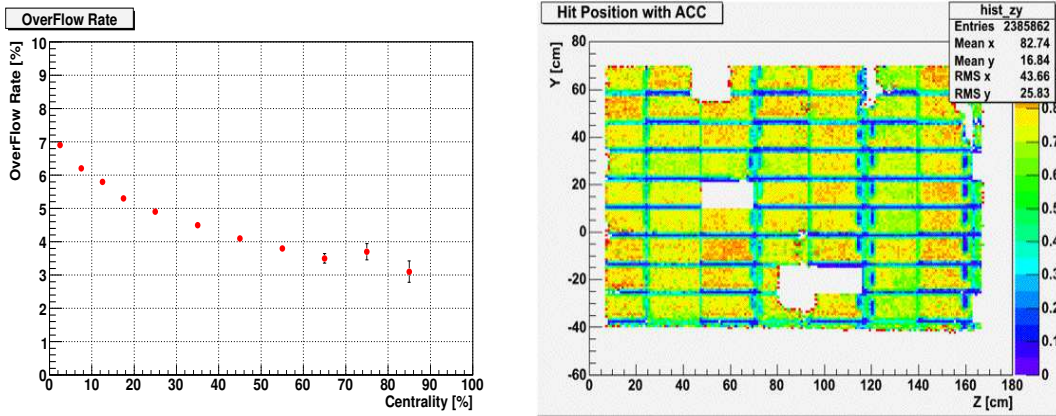


Figure 3.46: Left: Overflow rate as a function of centrality (Run4 200 GeV Au+Au). Right: 2D radiograph after excluding overflow tracks (Run4 200 GeV Au+Au).

3.9 Invariant Cross Section

Once all correction factors are determined as a function of p_T and centrality, they are applied to raw spectra to obtain final invariant yield and spectra.

In Run5 200 GeV p+p data, the BBC effective cross section is estimated at $\sigma_{BBC} = 23.0 \pm 2.2$ mb, and the trigger bias is estimated at 0.79 ± 0.02 [39]. We use these values in the p+p analysis to obtain invariant cross section.

3.10 Weak Decay Feed-down

Weak decays take place very close to a collision vertex. Since heavier particles take most of the decay momentum, these tracks are inseparable from tracks coming from the vertex of a collision. Indeed protons and anti-protons from weak decays (mainly from Λ and $\bar{\Lambda}$) can be reconstructed as tracks. Feed-down contribution from weak decays are estimated from lambda input p_T distribution and GEANT Monte Carlo simulation including PHENIX reconstruction process. The lambda input distribution is an effective distribution including higher resonance effect (Σ , Ξ). The data is taken from the STAR published paper [40]. Figure 3.47 shows the fraction of weak decay feed-down (anti)proton to measured (anti)proton as a function of p_T in 200 GeV p+p. In the thesis, no weak decay feed-down correction is applied to the results unless otherwise mentioned.

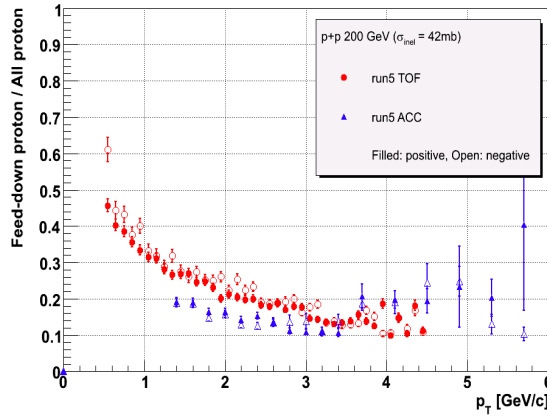


Figure 3.47: Fraction of weak decay feed-down (anti)proton to measured (anti)proton as a function of p_T in 200 GeV p+p.

3.11 Systematic Uncertainties

Evaluation of Systematic Uncertainties

Systematic uncertainties are evaluated by varying cut conditions in the data analysis. The same changes are applied in Monte Carlo to obtain the corresponding spectra. Some parts can be canceled when taking particle ratios. In the following, systematic uncertainties on TOF and ACC analyses are explained.

Systematic Uncertainties on TOF

Systematic uncertainties on p_T spectra, particle ratios are evaluated for TOF. The following cuts are changed for the systematic uncertainty study:

- PID Cut (σ in m^2) : $2\sigma/3\sigma$
- Fiducial Cut (narrow/wide) : w/wo additional cut of $|zed| < 50$ cm
- Track Matching Cut : $3\sigma/2\sigma$
- Magnetic field direction : $++/--$
- PID Contamination (from fitting methods in m^2)
- BG Subtraction at high p_T

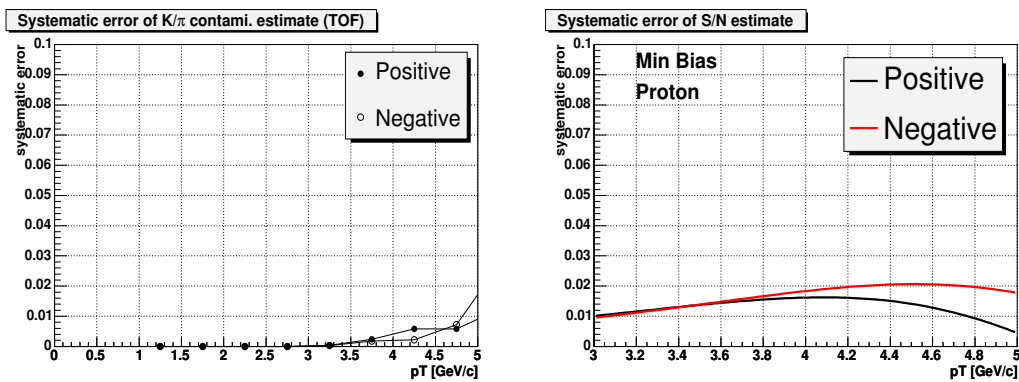
In Tables 3.5 and 3.6, the evaluated systematic errors on p_T spectra (particle ratio) obtained by the cut variation method are summarized as well as the occupancy correction errors. The total systematic errors are obtained by adding in quadrature each systematic uncertainty because they are independent. Figure 3.48 (left) shows the systematic error (from fitting methods) of pion/kaon contamination ratio in proton as a function of p_T . Figure 3.48 (right) shows the systematic error (from fitting methods) of S/N ratio in proton as a function of p_T .

Table 3.5: Systematic errors on p_T spectra (TOF, Run4 200 GeV Au+Au).

Errors	π^+	π^-	p	\bar{p}
PID Cut	3%	3%	3%	3%
Fiducial Cut	2%	2%	2%	2%
Track Matching	5%	5%	5%	5%
Magnetic field direction (+, -)	2%	2%	3%	3%
Occupancy correction	2%	2%	3%	3%
Pion/Kaon subtraction (>3 GeV/c, p_T dependent)	-	-	<1%	<1%
BG subtraction (>3 GeV/c, p_T dependent)	-	-	<2%	<2%
Total	<7%	<7%	<8%	<8%

Table 3.6: Systematic errors on particle ratio (TOF, Run4 200 GeV Au+Au).

Errors	p/π^+	\bar{p}/π^-	\bar{p}/p
PID Cut	5%	5%	2%
Fiducial Cut	3%	3%	2%
Track Matching	8%	8%	2%
Magnetic field direction (+, -)	2%	2%	3%
Occupancy correction	4%	4%	2%
Pion/Kaon subtraction (>3 GeV/c, p_T dependent)	<1%	<1%	<1%
BG subtraction (>3 GeV/c, p_T dependent)	<2%	<2%	<2%
Total	<11%	<11%	<5%

Figure 3.48: Systematic errors of kaon contamination ratio in proton (left) and S/N ratio (right) as a function of p_T (Run4 200 GeV Au+Au).

Systematic Uncertainties on ACC

Systematic uncertainties on p_T spectra, particle ratios are evaluated for ACC. The following cuts are changed for the systematic uncertainty study:

- PID Cut (N_{pe} threshold) : 10pe/6pe for pions, 4pe/3pe for protons
- Fiducial Cut (narrow/wide) : w/wo additional cut of $|zed| < 50$ cm
- Track Matching Cut : $3\sigma/2\sigma$
- Magnetic field direction : $++/- -$
- PID Contamination (from fitting methods in m^2)
- BG Subtraction at high p_T (from fitting methods in track matching residual)

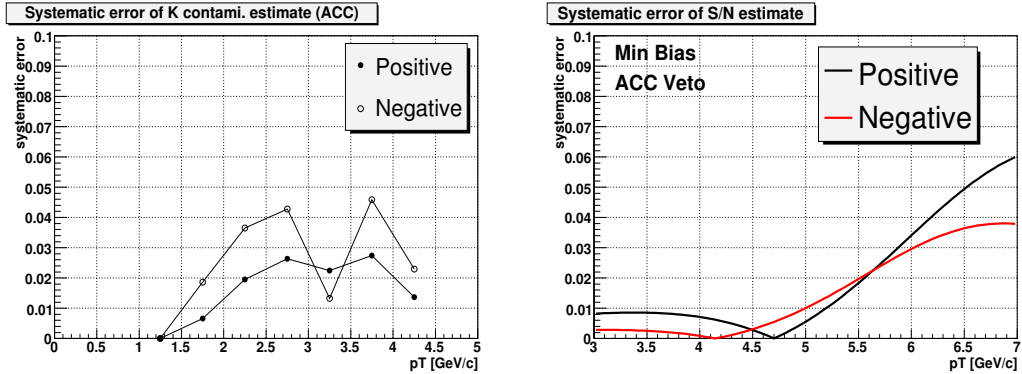
In Tables 3.7 and 3.8, the evaluated systematic errors on p_T spectra (particle ratio) obtained by the cut variation method are summarized as well as the occupancy correction errors. The total systematic errors are obtained by adding in quadrature each systematic uncertainty because they are independent. Figure 3.49 (left) shows the systematic error (from fitting methods) of kaon contamination ratio in proton (ACC-Not-Fired) as a function of p_T . Figure 3.49 (right) shows the systematic error (from fitting methods) of S/N ratio in proton (ACC-Not-Fired) as a function of p_T . Below $p_T = 5$ GeV/c, 1 % level is used for the errors.

Table 3.7: Systematic errors on p_T spectra (ACC, Run4 200 GeV Au+Au).

Errors	π^+	π^-	p	\bar{p}
PID Cut	4%	4%	4%	4%
Fiducial Cut	5%	5%	9%	9%
Track Matching	3%	3%	3%	3%
Magnetic field direction ($++,--$)	4%	4%	5%	2%
Occupancy correction	3%	3%	5%	5%
Kaon subtraction (2-5 GeV/c, p_T dependent)	-	-	<5%	<5%
BG subtraction (>3 GeV/c, p_T dependent)	<3%	<3%	<6%	<6%
Total	<9%	<9%	<15%	<14%

Table 3.8: Systematic errors on particle ratio (ACC, Run4 200 GeV Au+Au).

Errors	p/π^+	\bar{p}/π^-	\bar{p}/p
PID Cut	6%	6%	2%
Fiducial Cut	10%	10%	4%
Track Matching	1%	1%	1%
Magnetic field direction (+,+,- -)	3%	3%	5%
Occupancy correction	6%	6%	2%
Kaon subtraction (2-5 GeV/c, p_T dependent)	<5%	<5%	<2%
BG subtraction (>3 GeV/c, p_T dependent)	<5%	<5%	<3%
Total	<15%	<15%	<8%

Figure 3.49: Left: Systematic error of kaon contamination ratio in proton (ACC-Not-Fired) as a function of p_T (Run4 200 GeV Au+Au). Right: Systematic error of S/N ratio in proton (ACC-Not-Fired) as a function of p_T (Run4 200 GeV Au+Au).

Systematic Uncertainties on Nuclear Modification Factor

For nuclear modification factor R_{AA} , the following errors are included:

- Uncertainties of N_{coll} ($\sim >10\%$) from the Glauber calculation.
- Systematic errors on p_T spectra in p+p.
- Systematic errors on p_T spectra in Au+Au or Cu+Cu.

Chapter 4

Results

We have measured transverse momentum spectra ($\pi/K/p$ and their antiparticles), particle ratios (\bar{p}/p , p/π^+ , \bar{p}/π^-), and nuclear modification factors (R_{AA} , R_{CP}) with Run4 200 GeV Au+Au, Run5 200 GeV Cu+Cu, and Run5 200 GeV p+p data sets. Mainly, we focus on p/π ratio as a function of p_T and N_{part} to study scaling properties of those quantities between different collision systems (Au+Au, Cu+Cu) at different collision energies ($\sqrt{s_{NN}} = 200, 62.4$ GeV). The following results are shown.

- Transverse momentum (p_T) spectra
- Mean transverse momentum
- Particle yield (dN/dy) at mid rapidity
- Particle ratio: p/π^+ , \bar{p}/π^- , \bar{p}/p
- Nuclear modification factor (R_{AA} , R_{CP})

The particle identification is performed with Aerogel Cherenkov Counter (ACC) and Time-of-Flight detector (TOF). The cross checks are done in the overlapped p_T region between them. The p_T reach of particle identification is extended up to 6 GeV/c for (anti)protons by the introduction of ACC. But the statistics is still limited especially for calculating \bar{p}/p ratio and (anti)proton R_{CP} at high p_T . In the data analysis, we take into account background subtraction and particle contamination correction. These are done by using track matching residual distributions and mass squared distributions respectively. The spectra is fully corrected for 1) geometrical acceptance, 2) particle decay, 3) multiple scattering effects based on a single particle Monte Carlo simulation. The multiplicity dependence of tracking efficiency is also taken into account for each particle species by using the embedding method. Feed-down corrections from weak decays are not applied in all cases. We have done several detector calibrations, QA checks, and systematic error studies. Also, we compared the results with independent (or previous) measured results for PHENIX internal consistency check. The consistency is within about 10-20 %.

More than 60 % in centrality, some discrepancies between Run4 and previous Run2 results were seen. This is due to worse tracking resolution in z direction because of worse z-vertex resolution in most peripheral. Since the track matching tuning is done in Minimum Bias data, some difference could be seen in most peripheral. Now this part is fixed in the calibration stage.

4.1 Transverse Momentum Spectra

4.1.1 p_T spectra (ACC) – Au+Au 200 GeV

p_T spectra of charged pions and (anti)protons for different centralities in Au+Au collisions at $\sqrt{s_{NN}} = 200$ GeV are shown in Figures 4.1, 4.2. For comparison of the spectral shape, the data points are scaled vertically as quoted in the figures. The spectral shapes look similar when comparing them between different centrality bins, i.e., those are almost parallel to each other. In pion case, the spectra shows a concave shape than (anti)proton spectra.

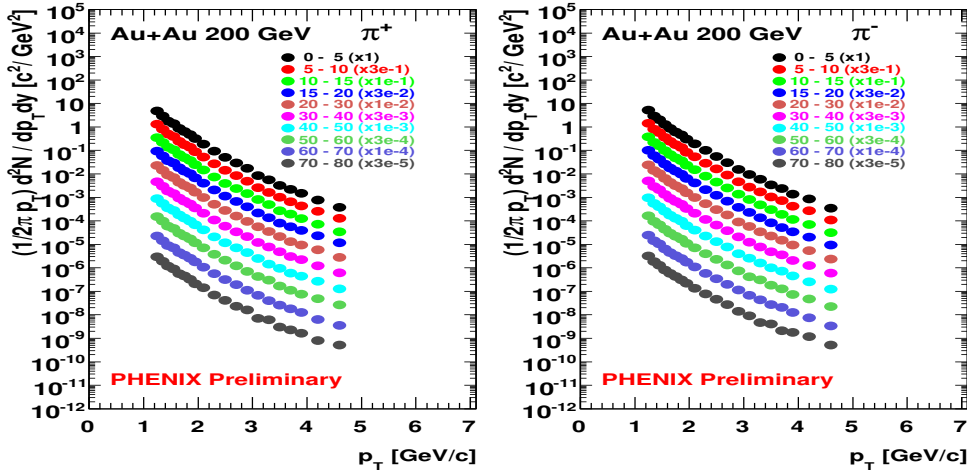


Figure 4.1: p_T spectra identified with ACC for charged pions for different centralities in Au+Au collisions at $\sqrt{s_{NN}} = 200$ GeV (left:positive, right:negative).

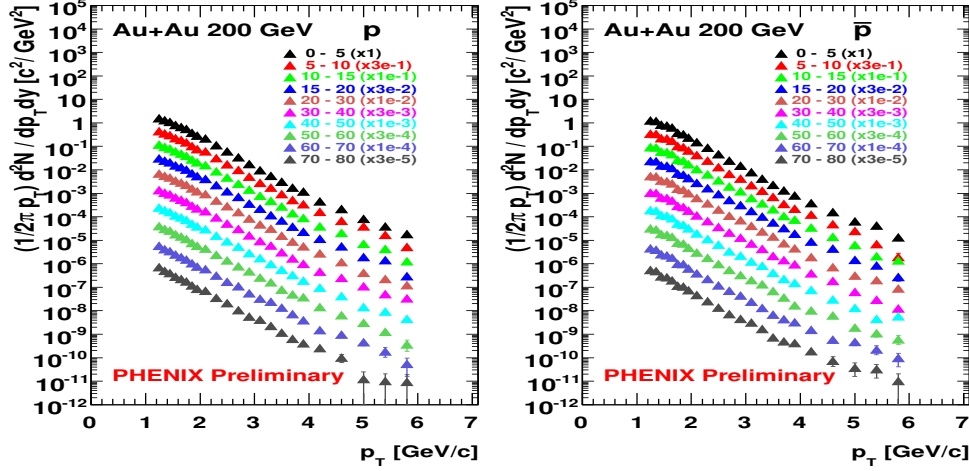


Figure 4.2: p_T spectra identified with ACC for protons and antiprotons for different centralities in Au+Au collisions at $\sqrt{s_{NN}} = 200$ GeV (left:positive, right:negative).

4.1.2 p_T spectra (TOF) – Au+Au 200 GeV

p_T spectra of $\pi/K/p$ for different centralities in Au+Au collisions at $\sqrt{s_{NN}} = 200$ GeV are shown in Figures 4.3~4.5. At low $p_T < 1$ GeV/c, pion shows a concave shape, kaon shows an exponential decreasing feature. A convex shape is clearly seen in (anti)proton spectra.

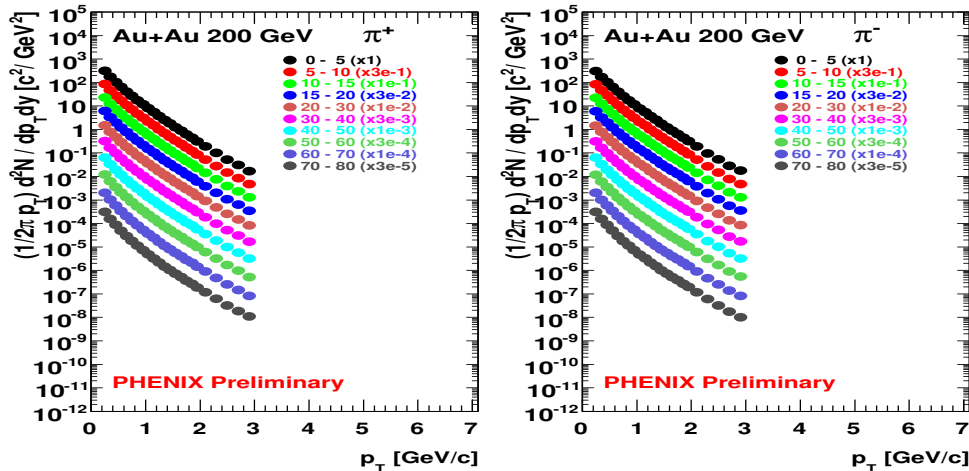


Figure 4.3: p_T spectra identified with TOF for charged pions for different centralities in Au+Au collisions at $\sqrt{s_{NN}} = 200$ GeV (left:positive, right:negative).

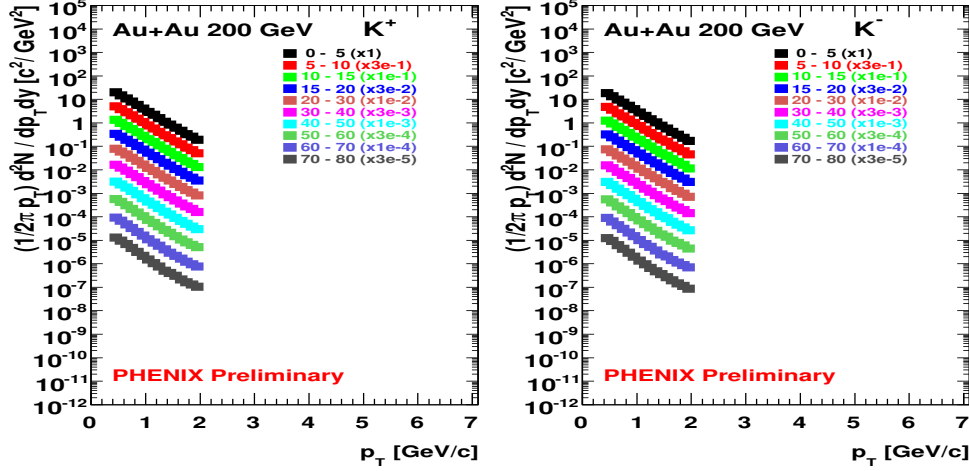


Figure 4.4: p_T spectra identified with TOF for charged kaons for different centralities in Au+Au collisions at $\sqrt{s_{NN}} = 200$ GeV (left:positive, right:negative).

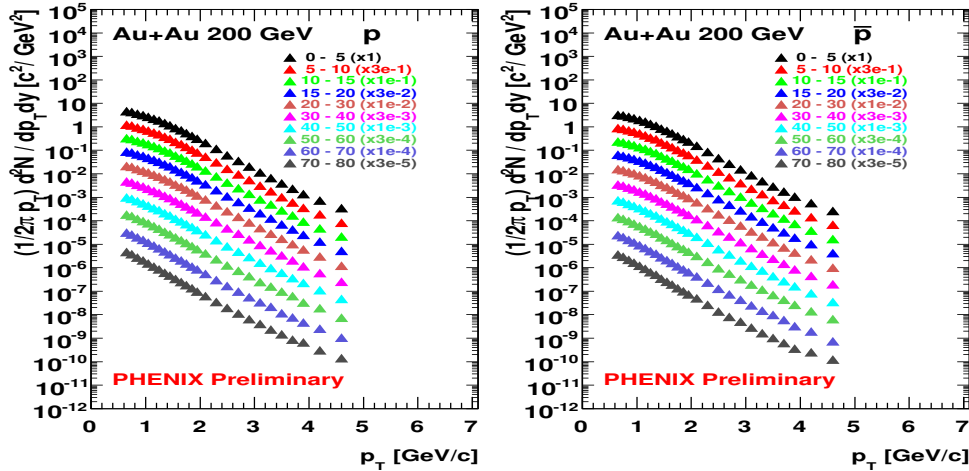


Figure 4.5: p_T spectra identified with TOF for protons and antiprotons for different centralities in Au+Au collisions at $\sqrt{s_{NN}} = 200$ GeV (left:positive, right:negative).

4.1.3 p_T spectra (ACC) – Cu+Cu 200 GeV

p_T spectra of charged pions and (anti)protons for different centralities in Cu+Cu collisions at $\sqrt{s_{NN}} = 200$ GeV are shown in Figures 4.6, 4.7. The particle identification is performed with ACC. The spectral shape in both pion and (anti)proton seem to be similar to those in Au+Au collisions. Comparisons between Au+Au and Cu+Cu systems are shown in the following sections in terms of mean transverse momentum and particle yields (see Sections 4.2, 4.3).

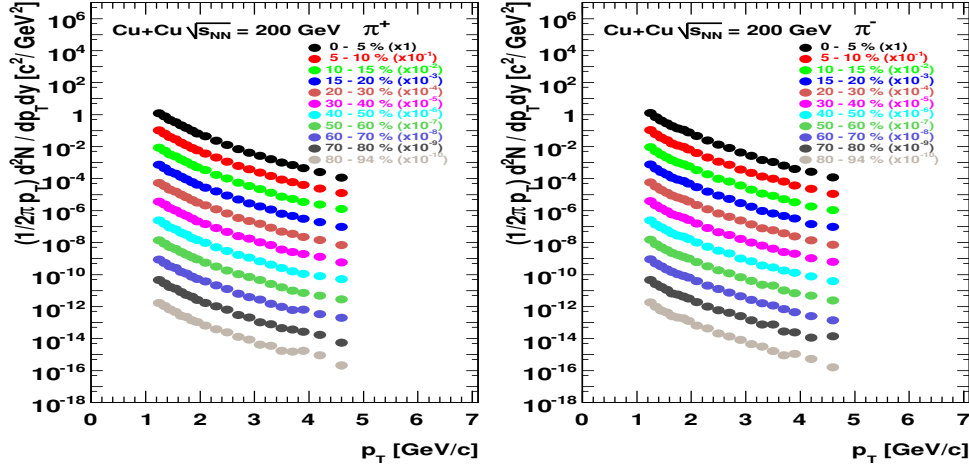


Figure 4.6: p_T spectra identified with ACC for charged pions for different centralities in Cu+Cu collisions at $\sqrt{s_{NN}} = 200$ GeV (left:positive, right:negative).

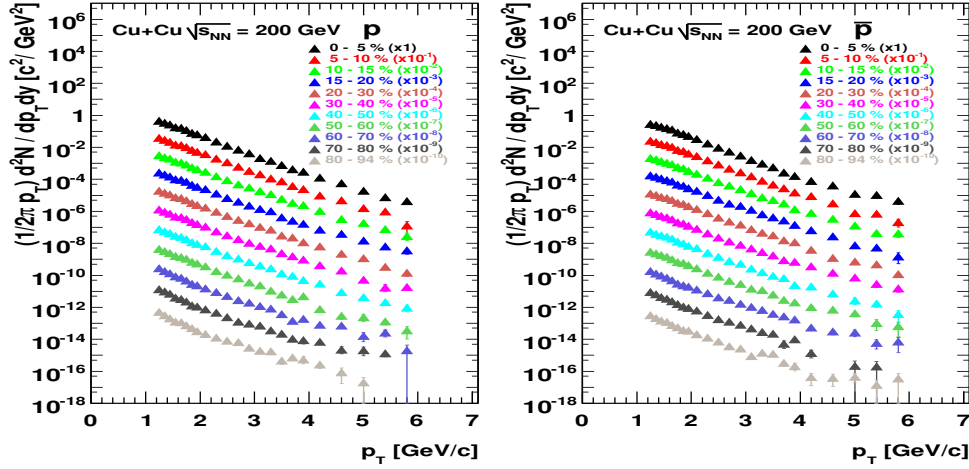


Figure 4.7: p_T spectra identified with ACC for protons and antiprotons for different centralities in Cu+Cu collisions at $\sqrt{s_{NN}} = 200$ GeV (left:positive, right:negative).

4.1.4 p_T spectra (TOF) – Cu+Cu 200 GeV

p_T spectra of $\pi/K/p$ for different centralities in Cu+Cu collisions at $\sqrt{s_{NN}} = 200$ GeV are shown in Figures 4.8 ~ 4.10. The particle identification is performed with TOF. The spectral shape in both $\pi/K/p$ are similar to those in Au+Au collisions. But the degree of convex shape in (anti)proton looks weaker. Cu+Cu collisions can provide better impact parameter resolution than peripheral Au+Au collisions. So a detailed system size dependence is shown in the following sections (see Sections 4.2, 4.3).

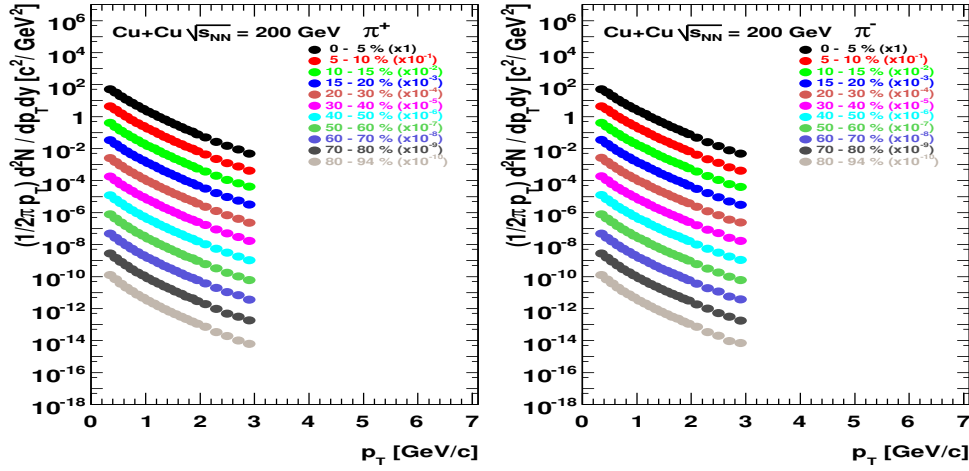


Figure 4.8: p_T spectra identified with TOF for charged pions for different centralities in Cu+Cu collisions at $\sqrt{s_{NN}} = 200$ GeV (left:positive, right:negative).

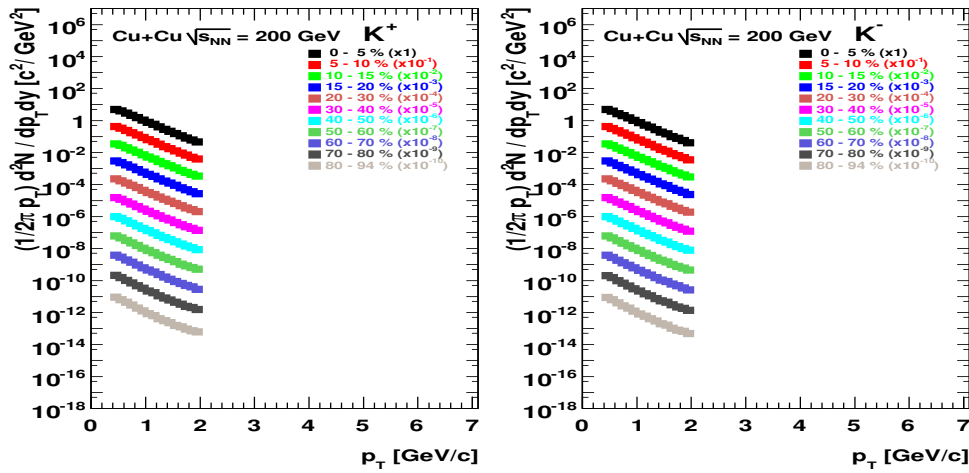


Figure 4.9: p_T spectra identified with TOF for charged kaons for different centralities in Cu+Cu collisions at $\sqrt{s_{NN}} = 200$ GeV (left:positive, right:negative).

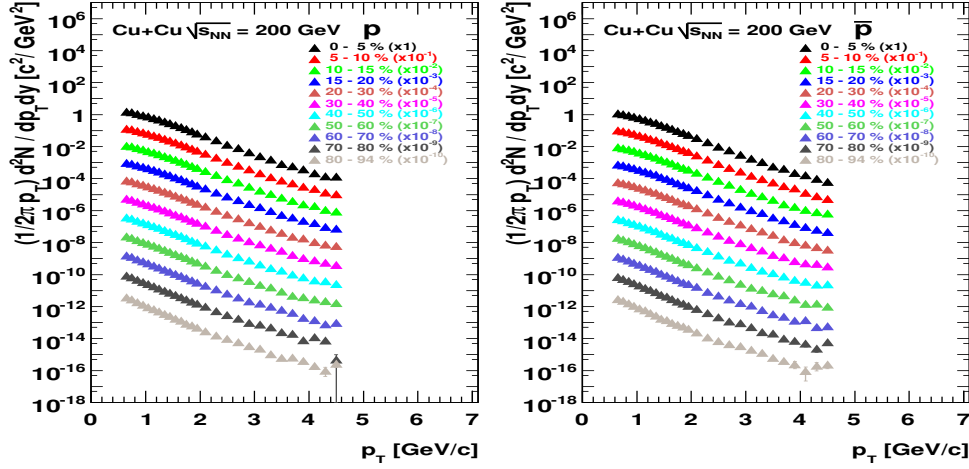


Figure 4.10: p_T spectra identified with TOF for protons and antiprotons for different centralities in Cu+Cu collisions at $\sqrt{s_{NN}} = 200$ GeV (left:positive, right:negative).

4.1.5 p_T spectra (TOF) – p+p 200/62.4 GeV

p_T spectra of $\pi/K/p$ in Minimum Bias p+p collisions at $\sqrt{s_{NN}} = 200/62.4$ GeV are shown in Figure 4.11 ~ 4.13. The particle identification is performed with TOF. The p+p spectra can be used as reference spectra to the measured spectra in Au+Au and Cu+Cu. Nuclear modification factors (R_{AA} , R_{CP}) are shown in the following section (see Section 4.5).

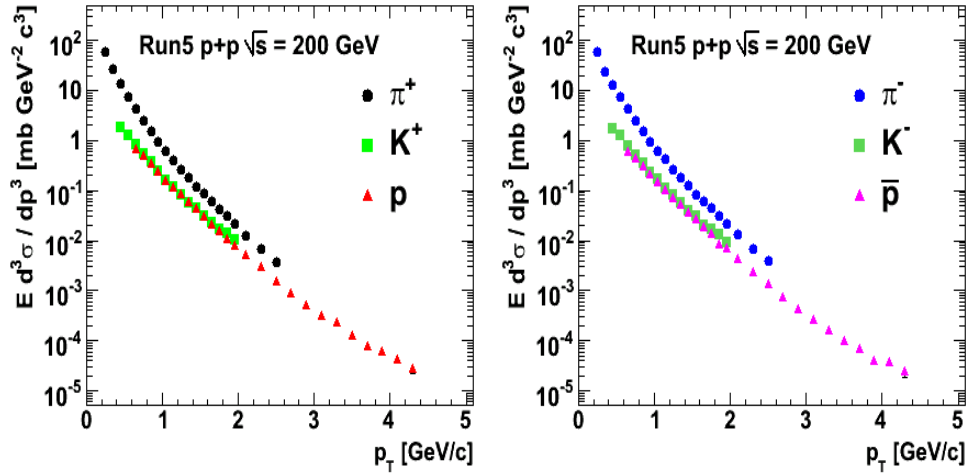


Figure 4.11: p_T spectra identified with TOF for $\pi/K/p$ in Minimum Bias p+p collisions at $\sqrt{s_{NN}} = 200$ GeV (left:positive, right:negative). The vertical axis is invariant cross section.

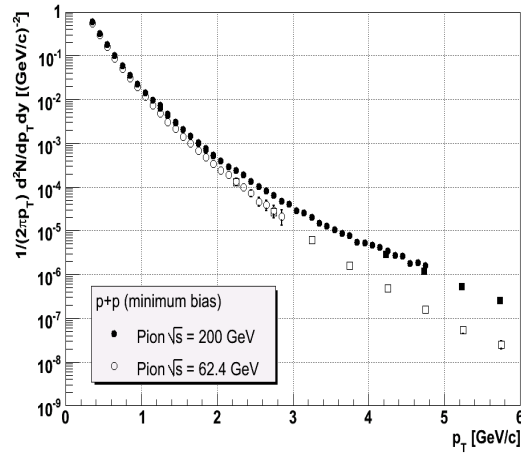


Figure 4.12: p_T spectra for pions in Minimum Bias $p+p$ collisions at $\sqrt{s_{NN}} = 200/62.4$ GeV.

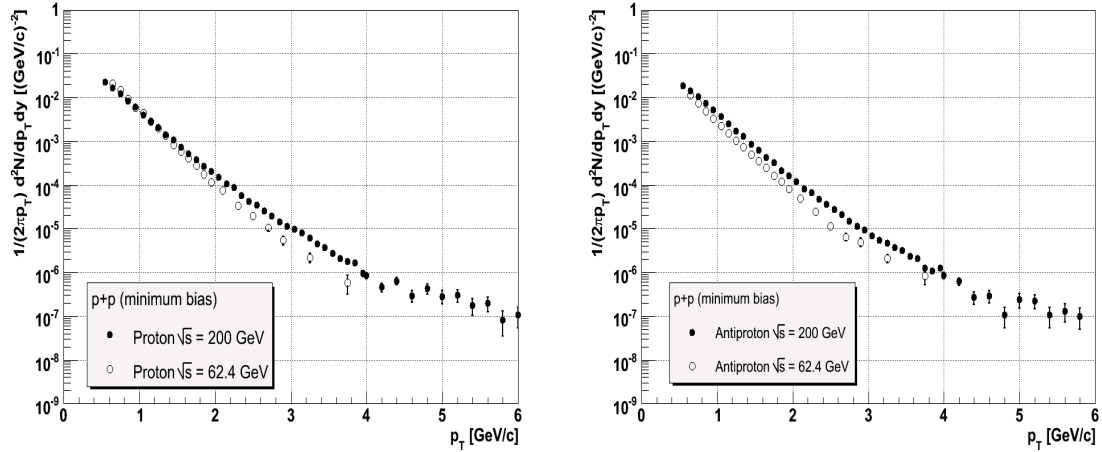


Figure 4.13: p_T spectra for protons (left) and antiprotons (right) in Minimum Bias $p+p$ collisions at $\sqrt{s_{NN}} = 200/62.4$ GeV.

4.2 Mean Transverse Momentum

Mean transverse momentum $\langle p_T \rangle$ is calculated for quantitative comparison of particle spectral shape especially at low p_T as shown in Figure 4.14. For extrapolation of p_T spectra at unmeasured low p_T , the following functions are used for different particle species: power-law function for pions, m_T exponential for kaons and (anti)protons.

$$\frac{1}{2\pi p_T} \frac{d^2N}{dp_T dy} = A \left(\frac{p_0}{p_0 + p_T} \right)^n \quad (4.1)$$

$$\frac{1}{2\pi m_T} \frac{d^2N}{dm_T dy} = A \exp\left(-\frac{m_T - m}{T}\right) \quad (4.2)$$

where A , p_0 , n , T are fitting parameters. We can see clear hadron mass and centrality dependences of $\langle p_T \rangle$. These dependences are consistent with radial flow picture. In this sense, radial flow more affects heavier particles than lighter ones. The strength of radial flow is larger in central collisions than in peripheral collisions. $\langle p_T \rangle$ is scaled with N_{part} between Au+Au and Cu+Cu collisions at both $\sqrt{s_{NN}} = 200$ GeV and 62.4 GeV. Those are smoothly connected to p+p values.

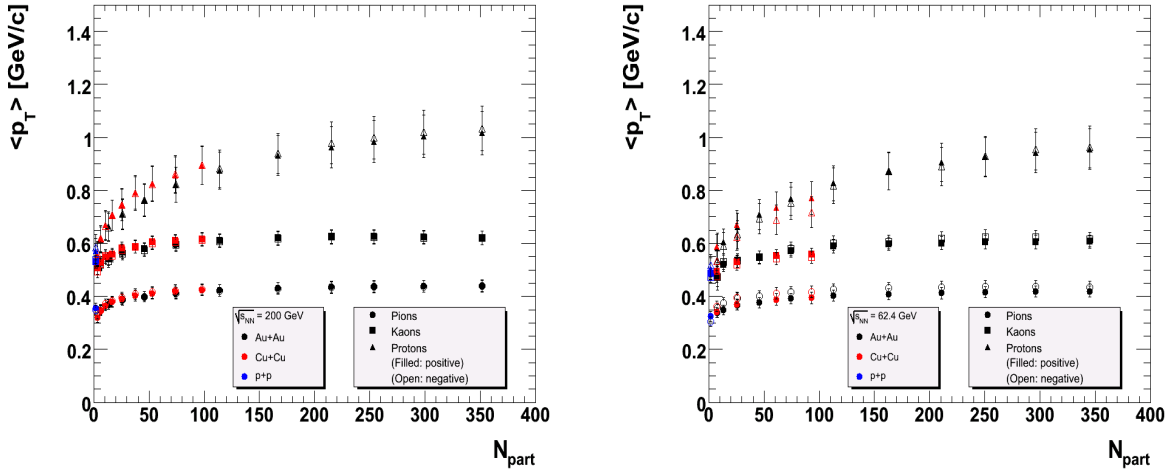


Figure 4.14: Mean transverse momentum as a function of N_{part} in Au+Au/Cu+Cu/p+p collisions at $\sqrt{s_{NN}} = 200$ GeV (left) and 62.4 GeV (right).

4.3 Particle Yield at Mid Rapidity

Particle yield per unit rapidity dN/dy is calculated for comparison of particle abundances at mid-rapidity as shown in Figure 4.15. The same functions in $\langle p_T \rangle$ calculation are used to evaluate dN/dy values. $dN/dy/(0.5N_{part})$ is plotted as the vertical quantity. dN/dy is expected to be scaled with the number of participants N_{part} since the low- p_T component of spectra is dominant in particle abundance and it is produced by soft coherent hadron production process. Actually N_{part} scaling is seen between Au+Au and Cu+Cu collisions at $\sqrt{s_{NN}} = 200$ GeV. But at 62.4 GeV, Au+Au values are lower than those in Cu+Cu. This may be caused by the difference of geometrical overlap shapes between the two systems (see Chapter 5).

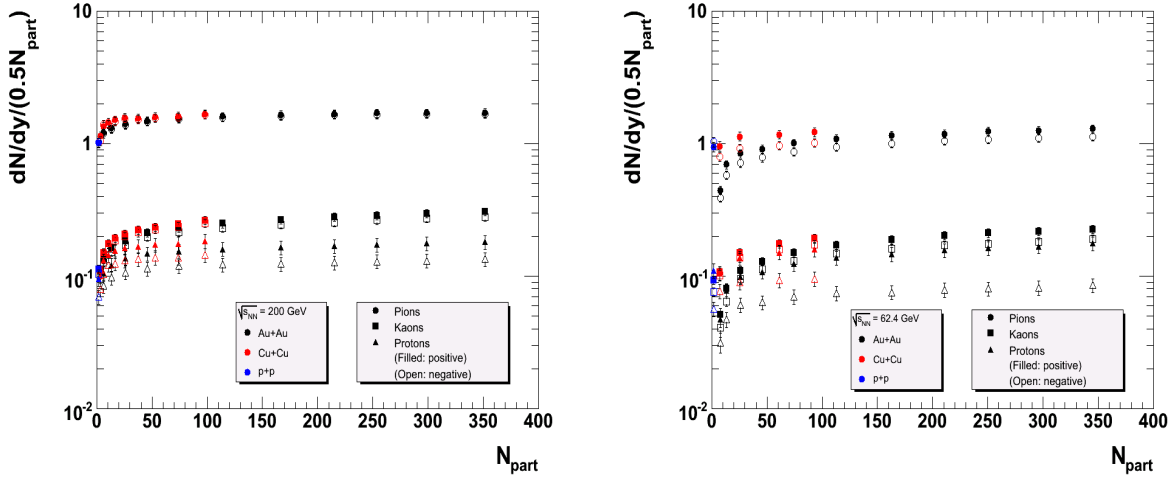


Figure 4.15: Particle yield dN/dy as a function of N_{part} divided by $0.5N_{part}$ in Au+Au/Cu+Cu/p+p collisions at $\sqrt{s_{NN}} = 200$ GeV (left) and 62.4 GeV (right).

4.4 Particle Ratios

4.4.1 p/π ratios vs. p_T

Particle ratios p/π^+ , \bar{p}/π^- as a function of p_T for different centralities in Au+Au/Cu+Cu collisions at $\sqrt{s_{NN}} = 200/62.4$ GeV are shown in Figures 4.16 \sim 4.18. Proton and antiproton enhancement is observed in all collision systems (Au+Au, Cu+Cu) in central to mid-central. We find that p_T dependence in Cu+Cu is similar to that in Au+Au.

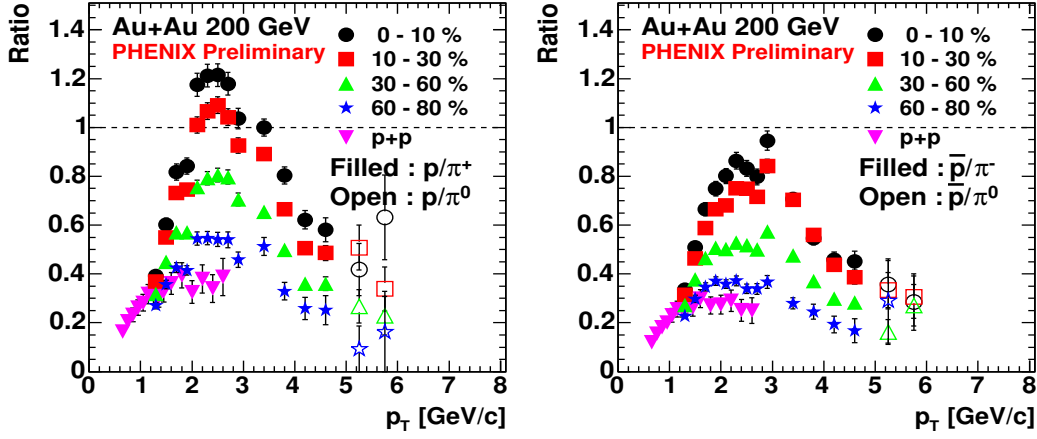


Figure 4.16: p/π^+ (left) and \bar{p}/π^- (right) ratios as a function of p_T for different centralities in Au+Au collisions at $\sqrt{s_{NN}} = 200$ GeV. The PID is done by ACC.

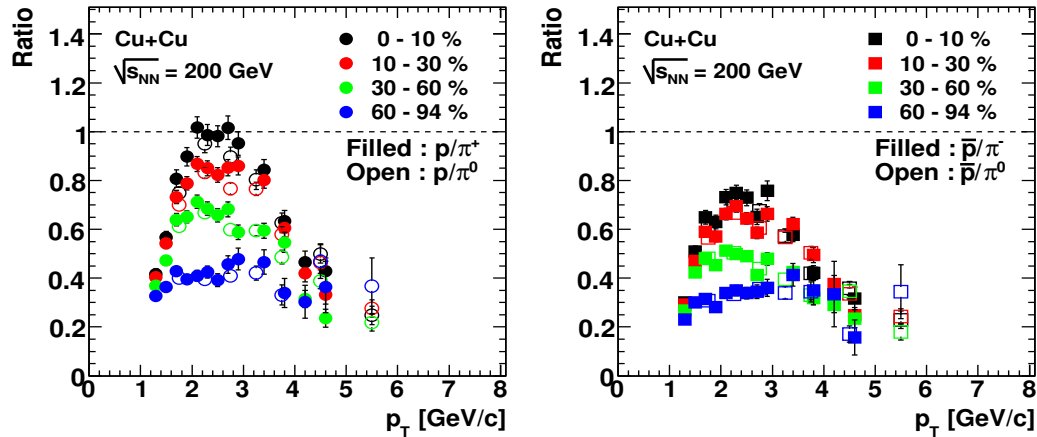


Figure 4.17: p/π^+ (left) and \bar{p}/π^- (right) ratios as a function of p_T for different centralities in Cu+Cu collisions at $\sqrt{s_{NN}} = 200$ GeV. The PID is done by ACC.

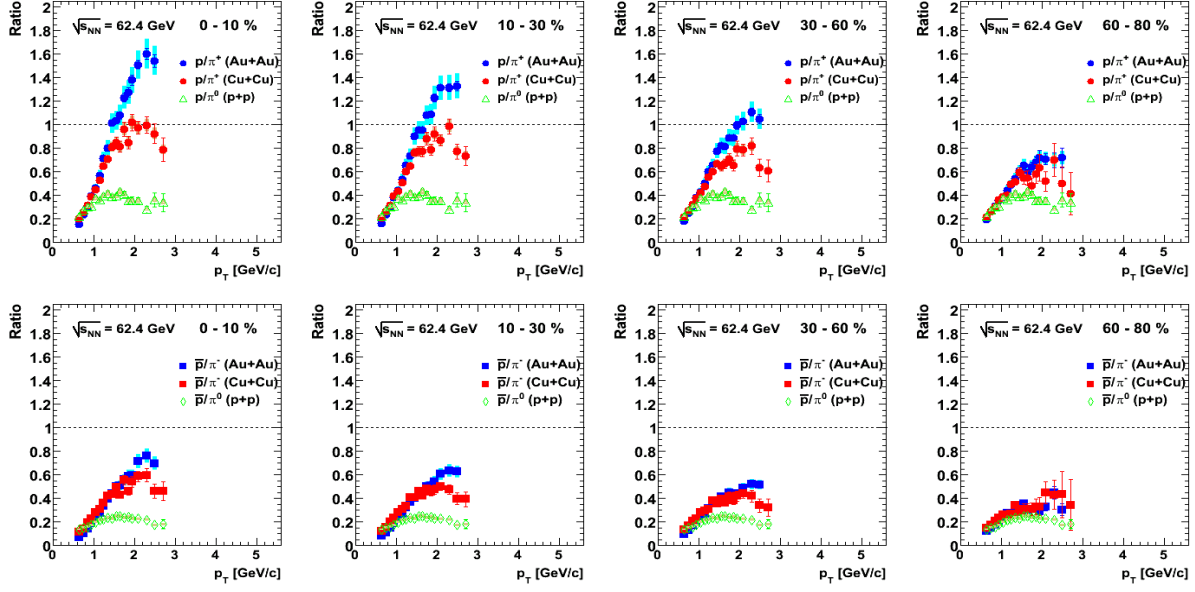


Figure 4.18: p/π ratios as a function of p_T for different centralities in Au+Au/Cu+Cu collisions at $\sqrt{s_{NN}} = 62.4 \text{ GeV}$ (upper: p/π^+ , lower: \bar{p}/π^-). The PID is done by TOF.

4.4.2 p/π ratios vs. N_{part}

For detailed comparison of the magnitude of p/π ratios (p/π^+ and \bar{p}/π^-) between different collision systems, we plot the p/π ratios as a function of $N_{part}^{1/3}$, which is corresponding to system size (the system volume is proportional to N_{part}), for each p_T interval (see Figures 4.19 ~ 4.23). Rectangular bands put on data points show systematic errors. The magnitude of p/π ratios are scaled with $N_{part}^{1/3}$ between Au+Au and Cu+Cu collisions at the same collision energy $\sqrt{s_{NN}} = 200/62.4 \text{ GeV}$.

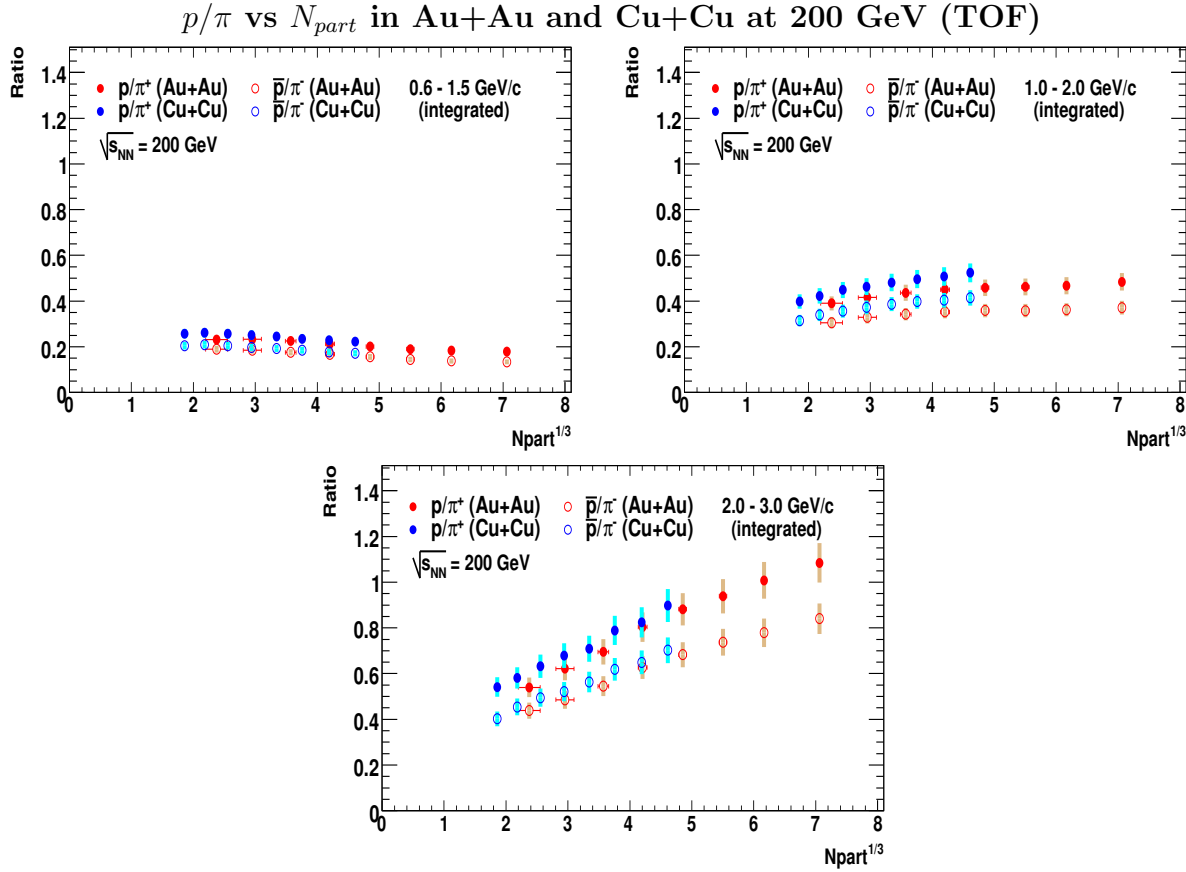


Figure 4.19: p/π ratios as a function of $N_{part}^{1/3}$ for different p_T regions (Au+Au and Cu+Cu at 200 GeV). The PID is done by TOF.

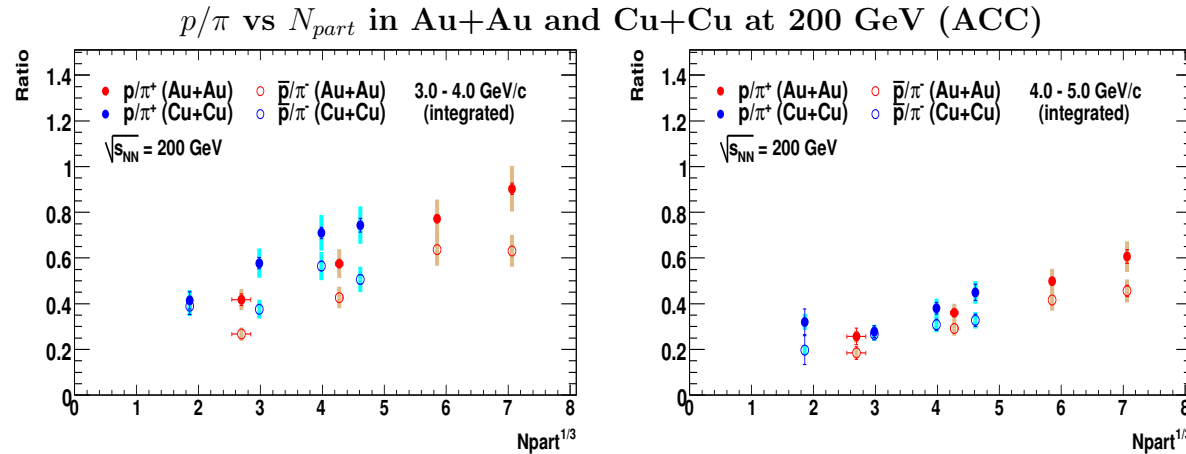


Figure 4.20: p/π ratios as a function of $N_{part}^{1/3}$ for different p_T regions (Au+Au and Cu+Cu at 200 GeV). The PID is done by ACC.

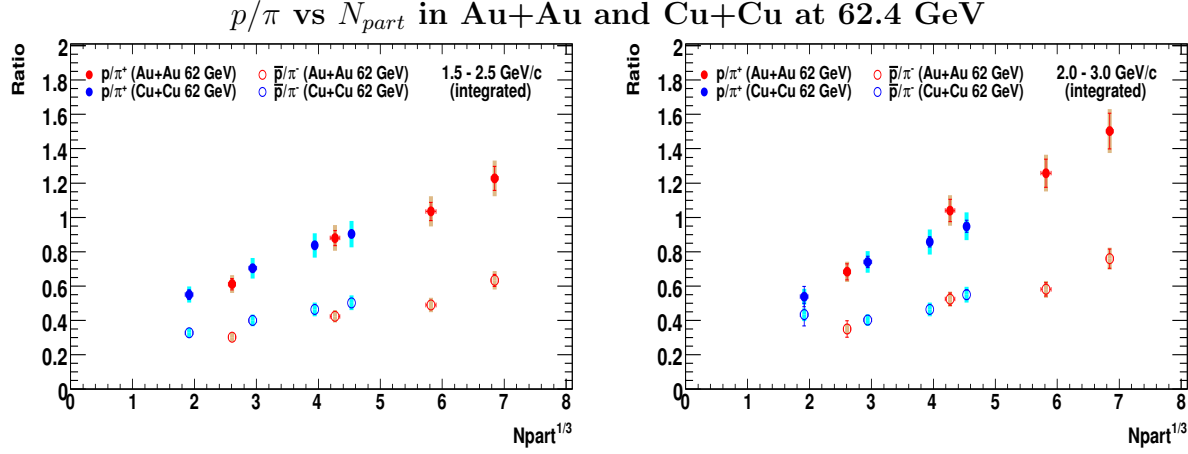


Figure 4.21: p/π ratios as a function of $N_{part}^{1/3}$ for different p_T regions (Au+Au and Cu+Cu at 62.4 GeV).

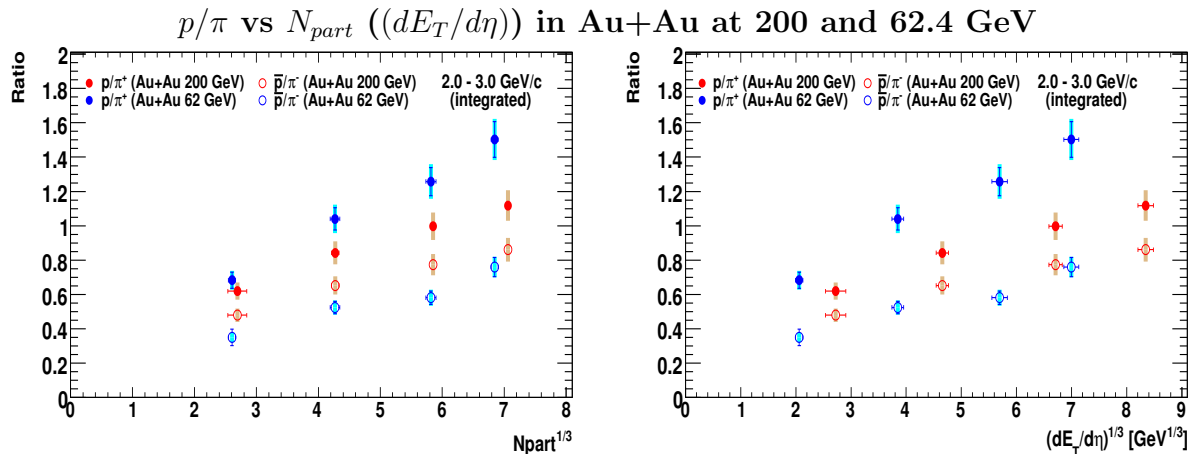


Figure 4.22: p/π ratios as a function of $N_{part}^{1/3}$ (left) ($dE_T/d\eta$) $^{1/3}$ (right) and for different p_T regions (Au+Au at 200 GeV and 62.4 GeV).

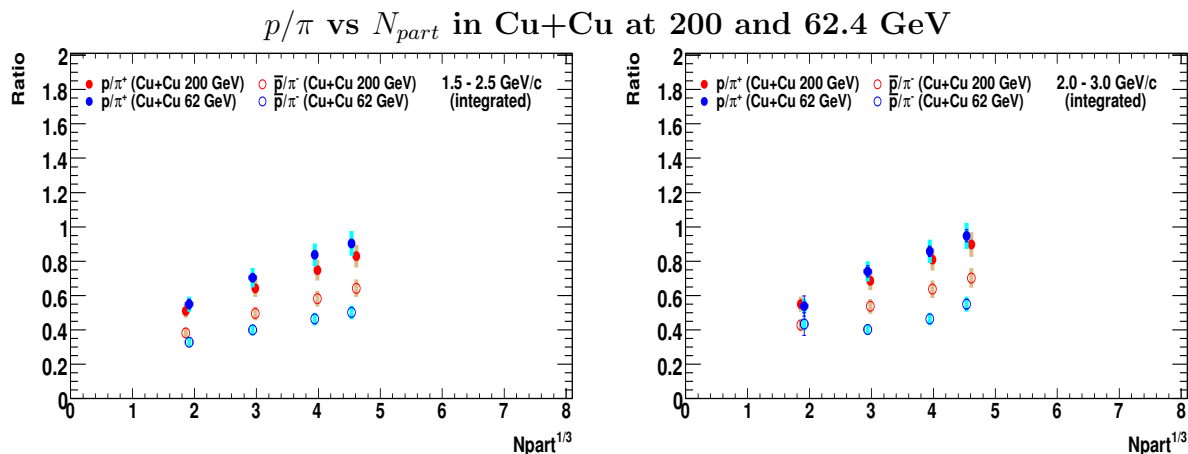


Figure 4.23: Left/Middle: p/π ratios as a function of $N_{part}^{1/3}$ for different p_T regions (Cu+Cu at 200 GeV and 62.4 GeV).

However the N_{part} scaling does not work between different collision energies 200 and 62.4 GeV in Au+Au collisions. Instead, \bar{p}/π^- ratio is scaled with transverse energy density $dE_T/d\eta$. p/π^+ ratio is still not scaled even in this case. Larger yield of proton at 62.4 GeV indicates that baryon transport process is not small at lower energy.

4.4.3 \bar{p}/p ratio vs. p_T

Particle ratio \bar{p}/p is shown as a function of p_T for Minimum Bias, centrality-selected cases in Au+Au and Cu+Cu collisions at $\sqrt{s_{NN}} = 200$ GeV in Figures 4.24 \sim 4.27. Rectangular bands put on data points show systematic errors. The ratios are almost independent of p_T and centrality up to 6 GeV/c in both Au+Au and Cu+Cu, and has a value of 0.7 ± 0.1 at $1 < p_T < 6$ GeV/c.

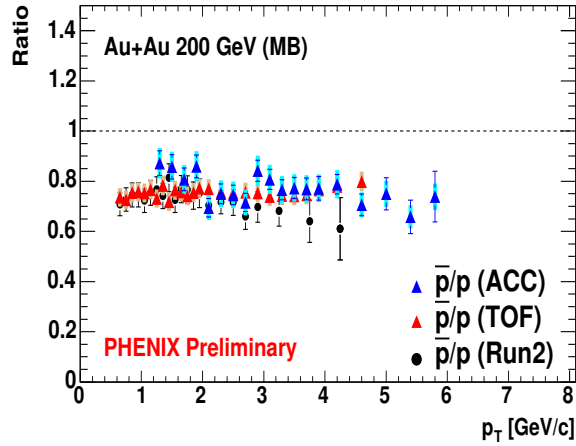


Figure 4.24: \bar{p}/p ratio as a function of p_T in Minimum Bias Au+Au collisions at $\sqrt{s_{NN}} = 200$ GeV.

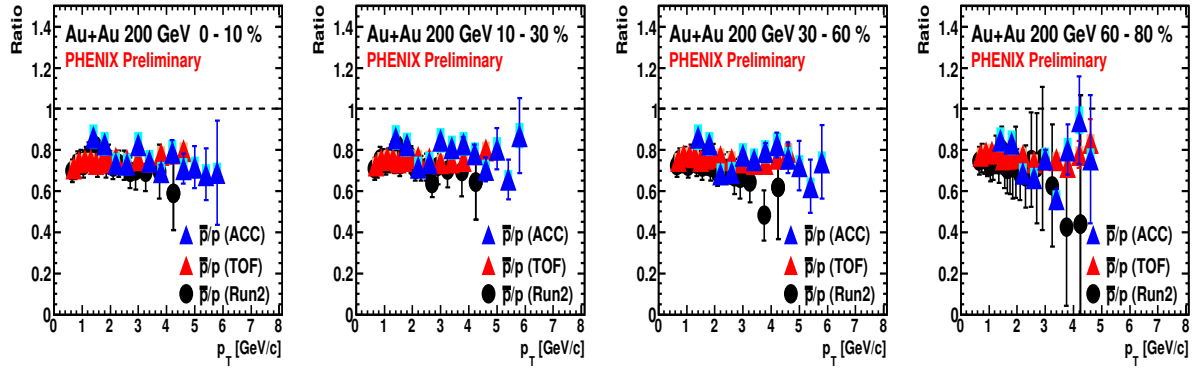


Figure 4.25: \bar{p}/p ratio as a function of p_T for different centralities in Au+Au collisions at $\sqrt{s_{NN}} = 200$ GeV.

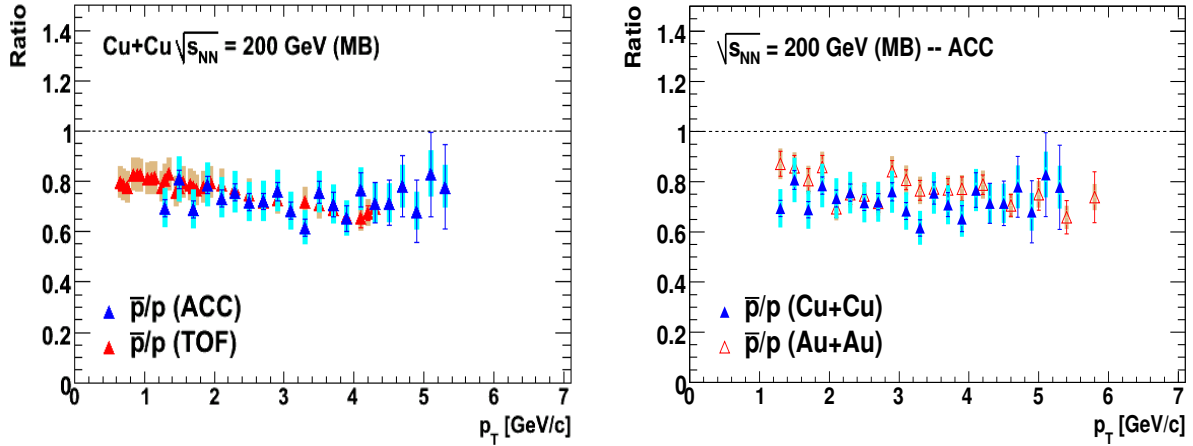


Figure 4.26: Left: \bar{p}/p ratio as a function of p_T in Minimum Bias Cu+Cu collisions at $\sqrt{s_{NN}} = 200$ GeV. Right: \bar{p}/p ratio as a function of p_T in Minimum Bias collisions (Au+Au and Cu+Cu at 200 GeV).

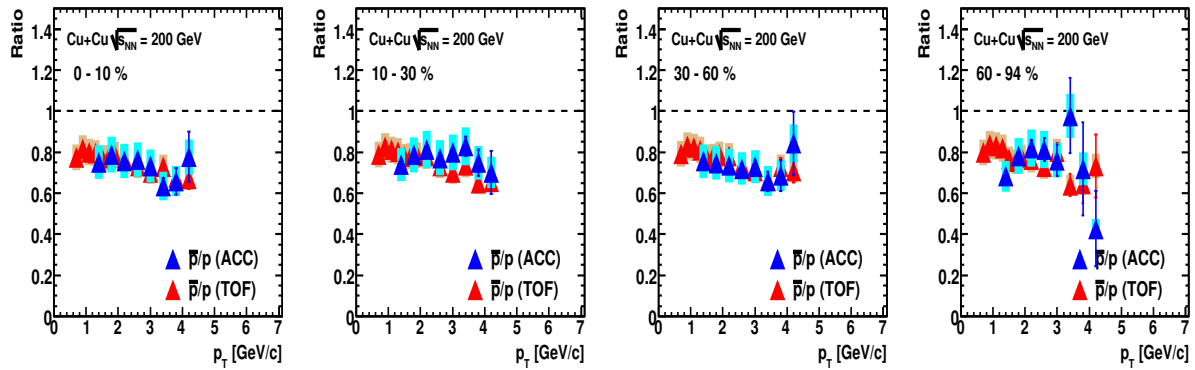


Figure 4.27: \bar{p}/p ratio as a function of p_T for different centralities in Cu+Cu collisions at $\sqrt{s_{NN}} = 200$ GeV.

4.5 Nuclear Modification Factors

It is useful to calculate nuclear modification factors, in order to look at the centrality dependence of p_T spectra in detail. The nuclear modification factors are defined relative to nucleon-nucleon collisions (R_{AA}) or relative to peripheral collisions (R_{CP}).

4.5.1 R_{AA}

Nuclear modification factor R_{AA} is shown for Au+Au and Cu+Cu collisions at $\sqrt{s_{NN}} = 200$ GeV in Figures 4.28 ~ 4.35. R_{AA} is defined as follows:

$$R_{AA}(p_T, y) = \left(\frac{1}{\langle N_{coll} \rangle} \frac{d^2 N^{A+A}}{dp_T dy} \right) / \left(\frac{1}{\sigma_{inel}^{N+N}} \frac{d^2 \sigma^{N+N}}{dp_T dy} \right) \quad (4.3)$$

where $\langle N_{coll} \rangle$ is the average number of binary nucleon-nucleon collisions. The denominator is the spectra in Run5 p+p at 200 GeV. The value of σ_{inel}^{N+N} is taken to be 42 mb. If any nuclear effects are absent, R_{AA} is expected to be unity. We find that (anti)protons are enhanced at 1.5 - 4 GeV/c, while pions and kaons are suppressed, for all centralities. K^* , ϕ R_{AA} from STAR experiment are also shown for comparison [42].

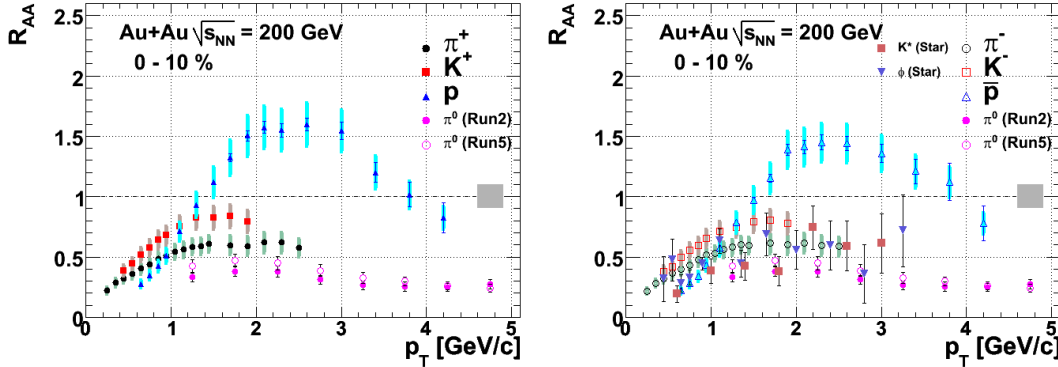


Figure 4.28: R_{AA} ($\pi/K/p$) as a function of p_T in 0-10% Au+Au collisions at 200 GeV.

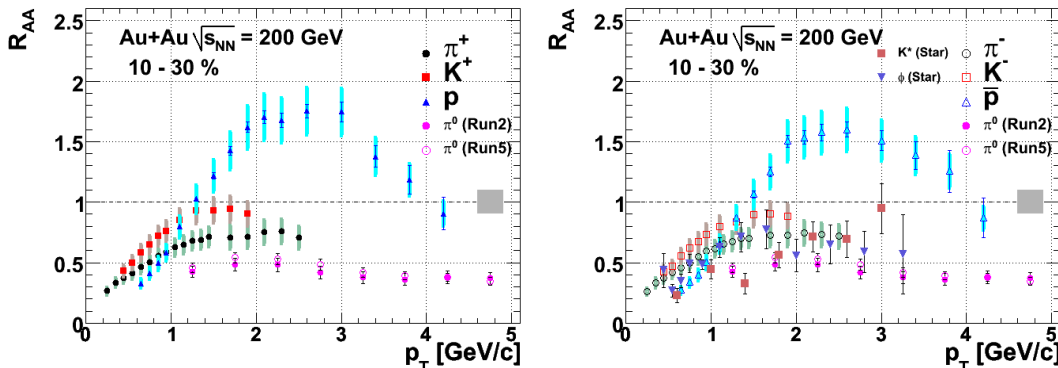


Figure 4.29: R_{AA} ($\pi/K/p$) as a function of p_T in 10-30% Au+Au collisions at 200 GeV.

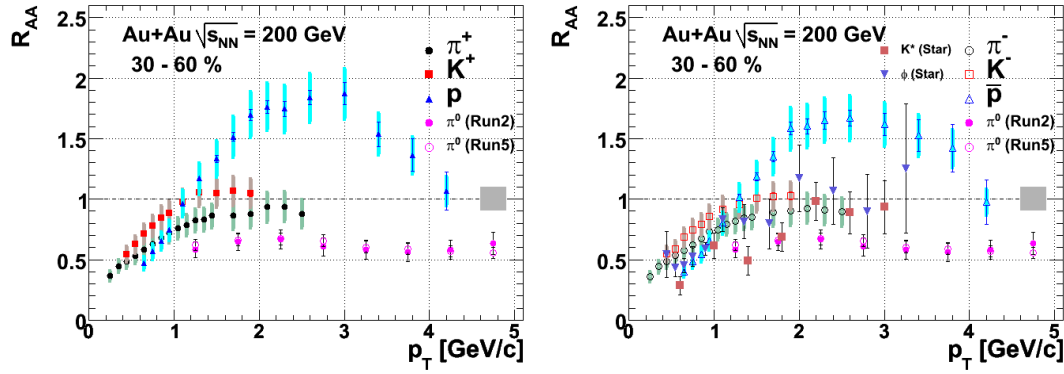


Figure 4.30: $R_{AA} (\pi/K/p)$ as a function of p_T in 30-60% Au+Au collisions at 200 GeV.

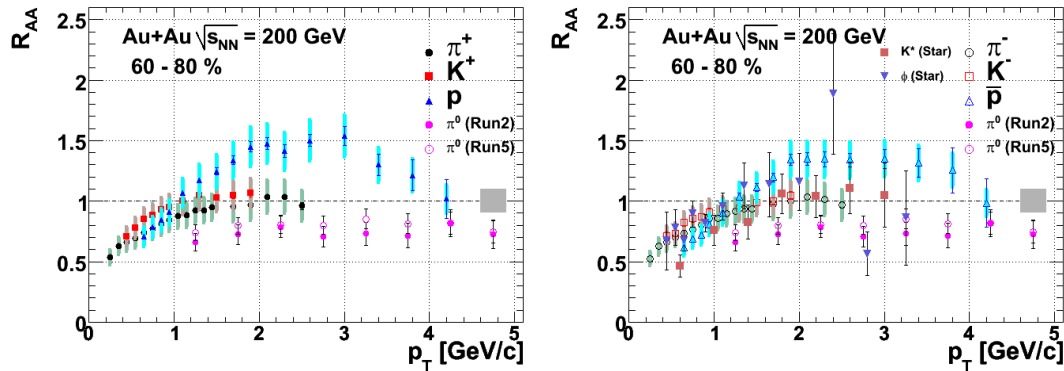


Figure 4.31: $R_{AA} (\pi/K/p)$ as a function of p_T in 60-80% Au+Au collisions at 200 GeV.

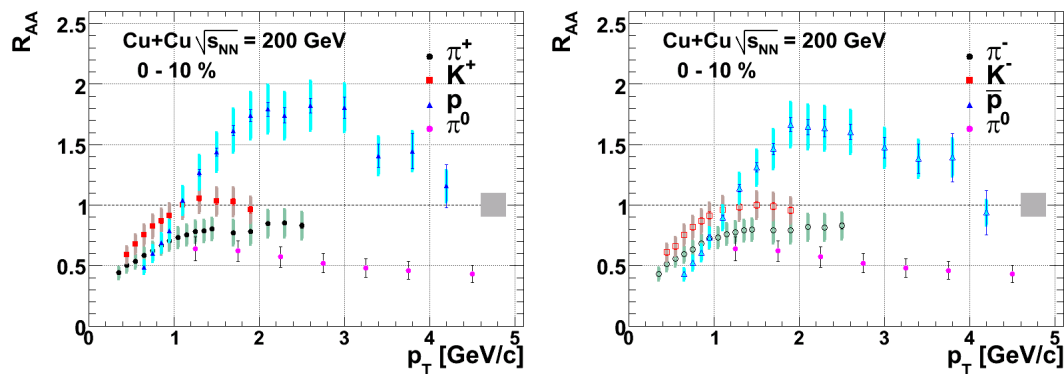


Figure 4.32: $R_{AA} (\pi/K/p)$ as a function of p_T in 0-10% Cu+Cu collisions at 200 GeV.

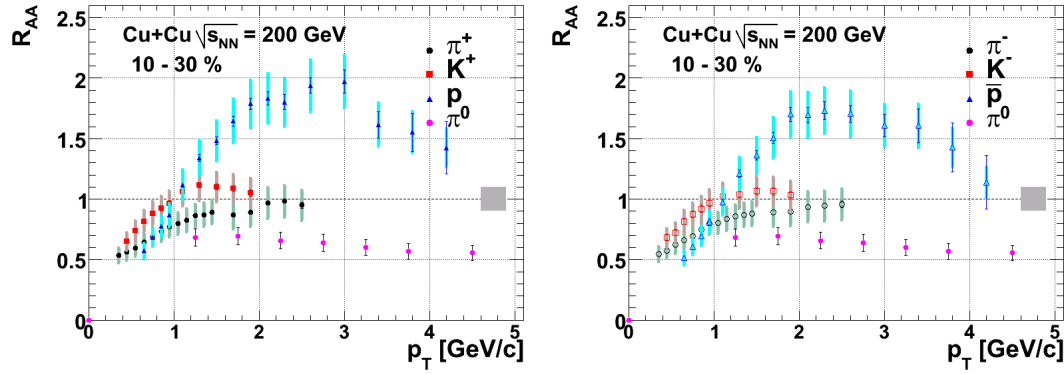


Figure 4.33: R_{AA} ($\pi/K/p$) as a function of p_T in 10-30% Cu+Cu collisions at 200 GeV.

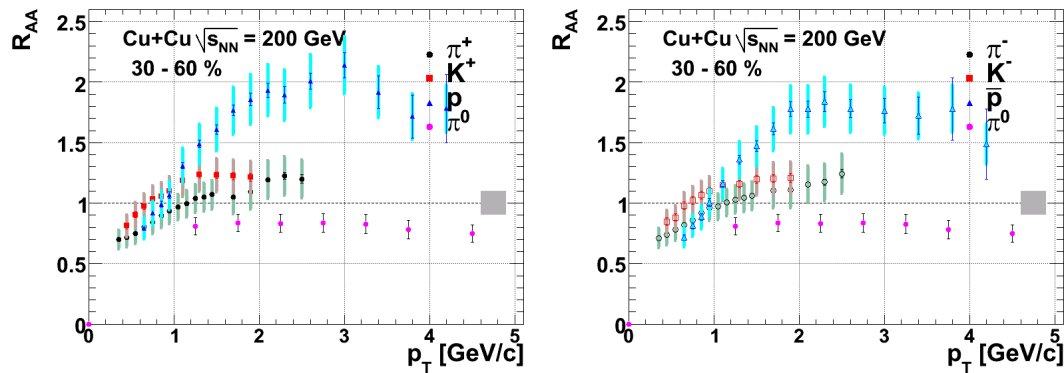


Figure 4.34: R_{AA} ($\pi/K/p$) as a function of p_T in 30-60% Cu+Cu collisions at 200 GeV.

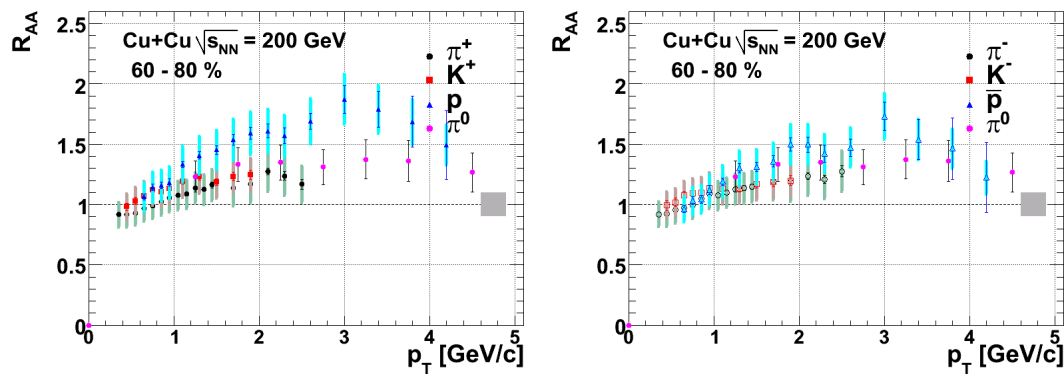


Figure 4.35: R_{AA} ($\pi/K/p$) as a function of p_T in 60-80% Cu+Cu collisions at 200 GeV.

Figure 4.36 shows R_{AA} at $p_T = 2.25 \text{ GeV}/c$ as a function of N_{part} in Au+Au/Cu+Cu collisions at $\sqrt{s_{NN}} = 200 \text{ GeV}$. While a weak suppression is seen for pions, kaons in central, (anti-)protons are clearly enhanced for all centralities. At most peripheral, all particle species (pions, kaons, and (anti)protons) are slightly enhanced (i.e., above unity). This enhancement could be attributed to the Cronin effect (enhancement from multiple scattering) as seen in d+Au collisions. Similar N_{part} dependence of R_{AA} is observed for Au+Au/Cu+Cu. This could be called N_{part} scaling of R_{AA} at the same collision energy as well as p/π ratio. Looking at the difference between Au+Au and Cu+Cu more seriously, R_{AA} of Cu+Cu is slightly larger than that of Au+Au. This relation is similar to that seen in dN/dy comparison.

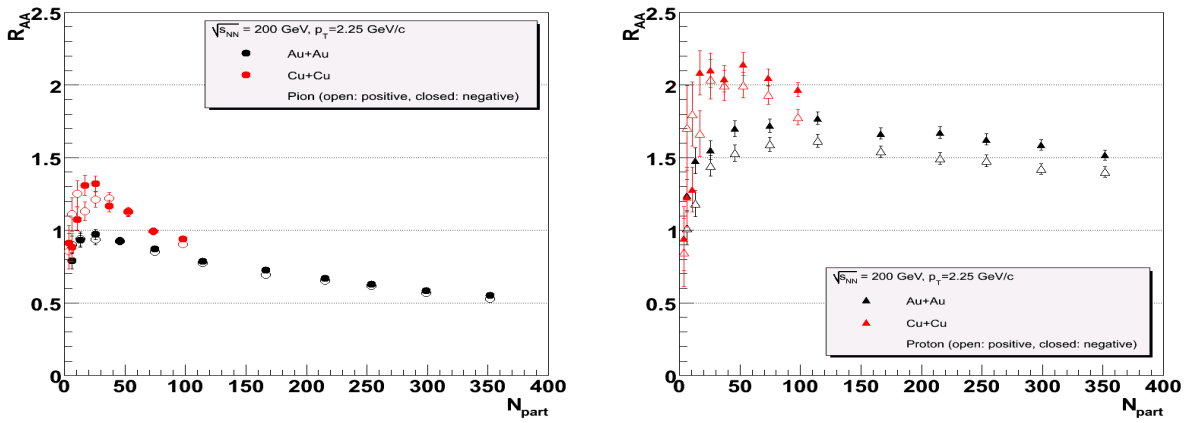


Figure 4.36: R_{AA} for pions (left) and (anti)protons (right) at $p_T = 2.25 \text{ GeV}/c$ as a function of N_{part} in Au+Au/Cu+Cu at $\sqrt{s_{NN}} = 200 \text{ GeV}$. Overall systematic error ($\sim 15\%$) is not included.

4.5.2 R_{CP}

Nuclear modification factor R_{CP} is shown for Au+Au and Cu+Cu collisions at $\sqrt{s_{NN}} = 200 \text{ GeV}$ in Figures 4.37 ~ 4.39. R_{CP} is defined as follows:

$$R_{CP}(p_T, y) = \left(\frac{1}{\langle N_{coll}^{cent} \rangle} \frac{d^2 N^{A+A, cent}}{dp_T dy} \right) / \left(\frac{1}{\langle N_{coll}^{peri} \rangle} \frac{d^2 N^{A+A, peri}}{dp_T dy} \right) \quad (4.4)$$

where $\langle N_{coll} \rangle$ (average number of binary nucleon-nucleon collisions) are taken from the PHENIX Glauber model calculation. The overall systematic error (N_{coll} uncertainties) on R_{CP} is shown as a vertical band. The statistical errors are shown as error bar on each data point. For proton R_{CP} , the statistical errors have been significantly reduced compared to the previous Run2 results by the high statistics data and the introduction of ACC. The result shows a stronger suppression for pions than protons in the intermediate p_T range (2-4 GeV/c). Over the measured p_T range,

we do not observe a difference in R_{CP} between particles and antiparticles. At higher p_T we observe an approaching trend of proton R_{CP} into pion R_{CP} . Figure 4.38 shows pion and proton R_{CP} including K_s^0 and Λ particles. K_s^0 is suppressed as pions, but Λ is less suppressed at intermediate p_T . R_{CP} results can be grouped into baryon's and meson's groups. The grouping of R_{CP} according to the number of constituent quarks could be attributed to quark recombination picture at hadronization. Figure 4.39 shows pion and proton R_{CP} including K^* and ϕ particles. The centrality dependence is seen in the magnitude of R_{CP} . In central, pions are more suppressed than in peripheral. The magnitude relation between pions and (anti)protons does not change in any centrality bin. K^* and ϕ R_{CP} shows similar magnitude as pion R_{CP} . So mesons can be grouped even though K^* and ϕ have relatively large mass (892 MeV for K^* , 1020 MeV for ϕ).

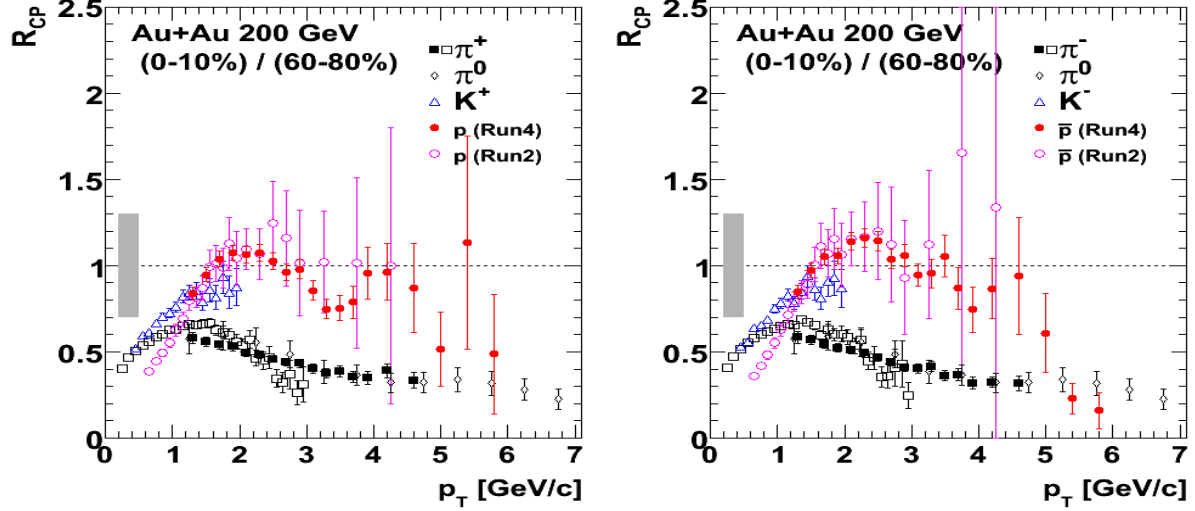


Figure 4.37: R_{CP} (0-10% / 60-80%) for $\pi/K/p$ as a function of p_T in Au+Au collisions at $\sqrt{s_{NN}} = 200$ GeV. The Run2 proton R_{CP} is also plotted.

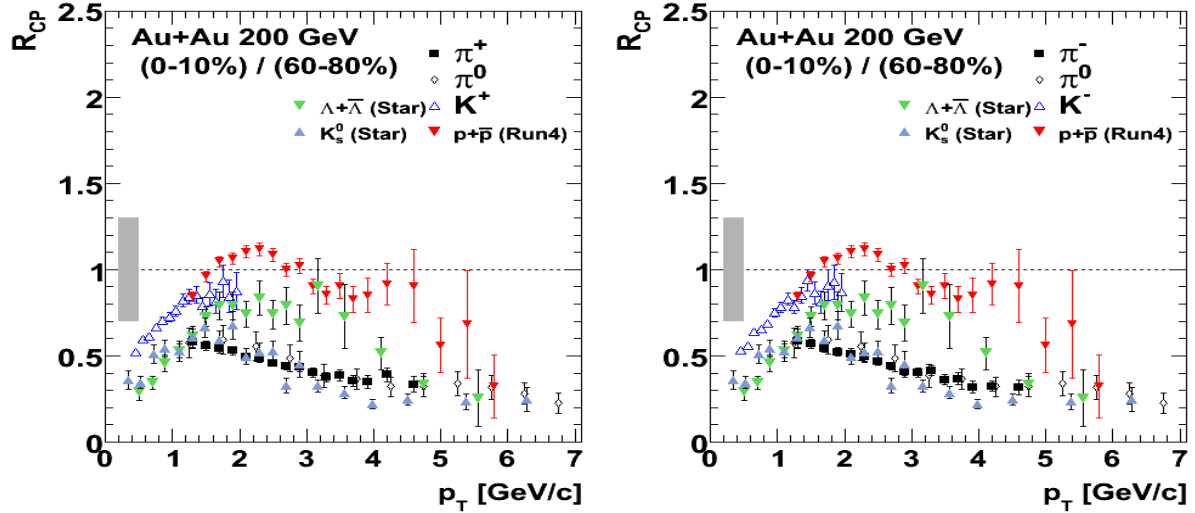


Figure 4.38: R_{CP} (0-10% / 60-80%) for $\pi/K/p$ as a function of p_T in Au+Au collisions at $\sqrt{s_{NN}} = 200$ GeV. K_s^0 , Λ R_{CP} from STAR experiment are also shown [41].

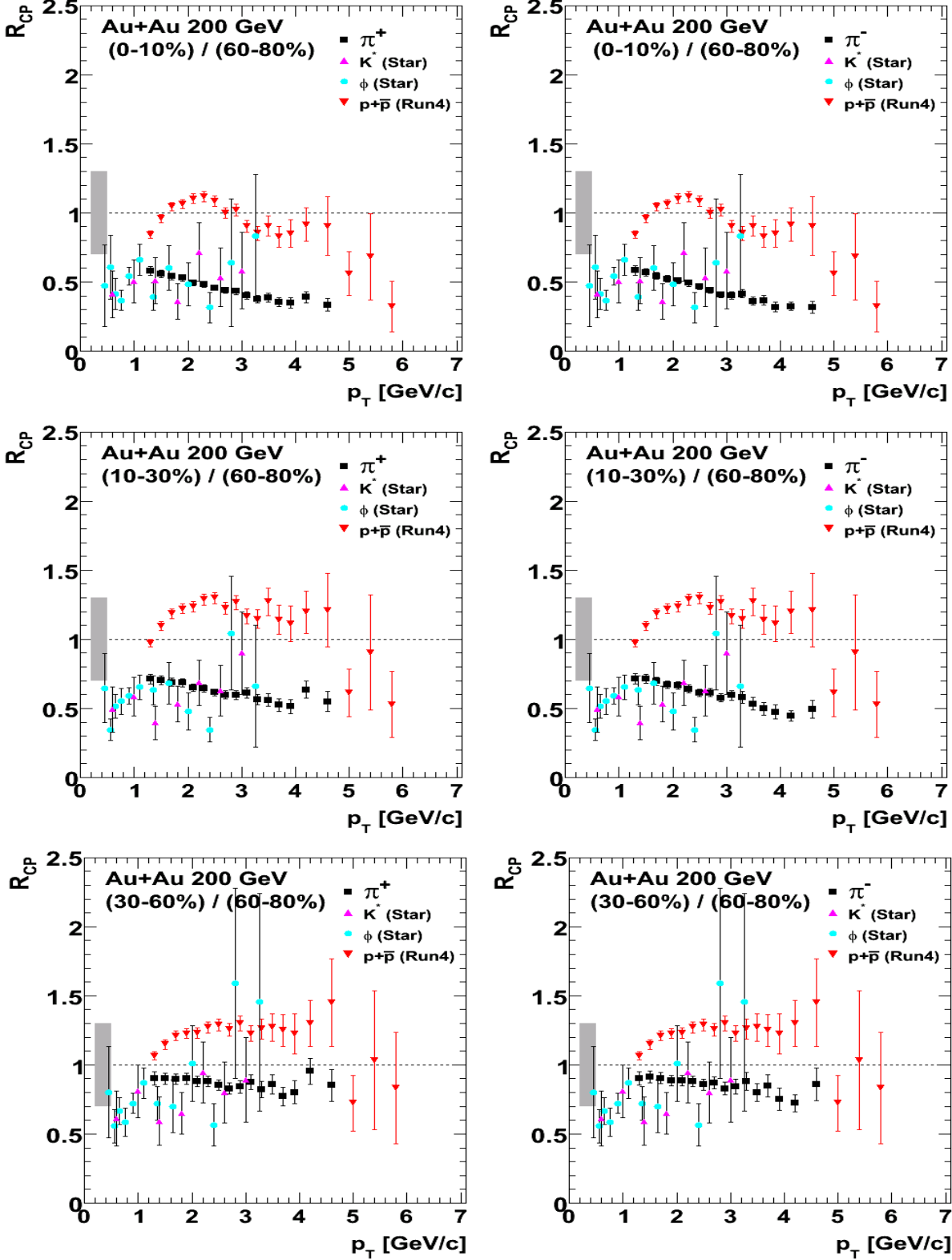


Figure 4.39: R_{CP} for pions, kaons, and (anti)protons as a function of p_T in Au+Au collisions at $\sqrt{s_{NN}} = 200$ GeV. The centrality selection is 0-10%/60-80%, 10-30%/60-80%, 30-60%/60-80% from top to bottom. K^* , ϕ R_{CP} from STAR experiment are also shown for comparison [42].

Chapter 5

Discussions

In this chapter, we discuss freeze-out properties and hadron production at intermediate p_T (2-5 GeV/c), especially (anti)proton production, in relativistic heavy ion collisions at RHIC. Statistical model and blast-wave model are used to extract chemical/kinetic freeze-out properties. Also we compare the obtained particle ratios with quark recombination models, PYTHIA calculations.

5.1 Freeze-out Properties

Bulk properties of heavy ion collisions are originated from soft hadrons with transverse momentum $p_T \lesssim 2$ GeV/c. Soft hadrons are decoupled from the collision area at late stage of the space-time evolution. A concept of freeze-out is useful for characterizing bulk properties. Freeze-out is defined by a space-time hypersurface, where the mean free path of hadrons becomes larger than the typical scale of the expanding system. So local thermal equilibrium is no longer maintained due to the lack of interactions between hadrons.

As first observed at AGS, SPS, and confirmed at RHIC, the shapes and the normalizations of the hadron momentum spectra reflect two different stages of the collision [43]. The freeze-out can be separated into two stages as follows:

- Chemical freeze-out: ratios of particle abundances are fixed because inelastic scatterings cease. In other words, chemical composition of emitting particles is frozen after hadronization.
- Kinetic freeze-out: kinetic equilibrium is no longer maintained. Until this freeze-out, the spectral shapes are affected by hadronic scatterings.

The freeze-out properties such as temperatures, chemical potentials, radial flow velocity can be extracted from hadron yield or spectral shape. These are parameterizations to reproduce the data based on models.

5.1.1 Chemical Freeze-out – Statistical Model Fit

As shown in Figure 4.15, dN/dy of $\pi/K/p$ as a function of N_{part} in different collision systems. A fast increase with system volume is observed reaching a saturation at about ~ 100 participants. We can see that dN/dy is roughly scaled with N_{part} between Au+Au and Cu+Cu at the same $\sqrt{s_{NN}}$. Assuming a simple proportionality between the system volume and the number of participants, one can say that bulk yields are controlled by the system volume. Strictly speaking, peripheral Au+Au values are slightly lower than those in Cu+Cu. This may be caused by the difference of geometrical overlap shapes between the two systems. The shape of the overlapped region in peripheral Au+Au is more deformed. The number of nucleon-nucleon collisions per nucleon is larger than in Cu+Cu than in peripheral Au+Au. This could be one of the reasons. Ratios of dN/dy (Au+Au, Cu+Cu) are almost flat as a function of N_{part} within the experimental uncertainty. This means that a factorization of energy and system volume dependences can be done.

Figure 5.1 shows antibaryon-to-baryon ratios as a function of collision energy. In 62.4 GeV Au+Au collisions, \bar{p}/p ratio is about 0.5 and follows the smooth curve from SPS to RHIC. It is consistent with the preliminary $\bar{\Lambda}/\Lambda$ ratio measured by STAR.

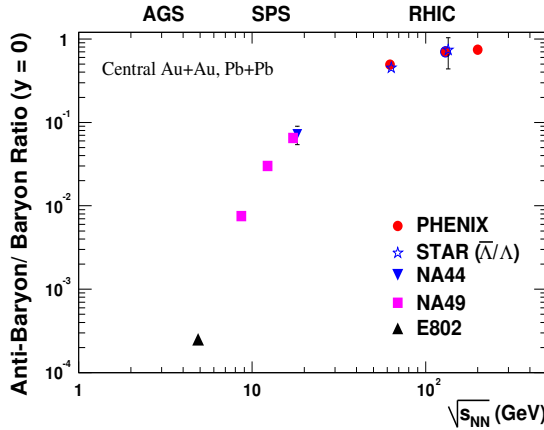


Figure 5.1: Beam energy dependence of antibaryon-to-baryon ratios from AGS to RHIC.

It is well known that total hadron yields and ratios can be described by a purely statistical model. The statistical model approach is established by analyses of particle ratios in high energy heavy ion collisions in GSI-SIS to CERN-SPS energy and elementary collisions ($e^+ + e^-$, $p + p$, and $p + \bar{p}$). The hadron yields are given by p_T -integrated yield which is dominated by low- p_T particles. In statistical model, the measured hadron yields and their ratios are controlled by chemical potentials and chemical freeze-out temperature.

We adopt a grand canonical ensemble for a chemical freeze-out model [44]. In the model, the density of a particle species i is given by:

$$\rho_i = \gamma_s^{(s+\bar{s})_i} \frac{g_i}{2\pi^2} T_{ch}^3 \left(\frac{m_i}{T_{ch}}\right)^2 K_2\left(\frac{m_i}{T_{ch}}\right) \exp\left(\frac{Q_i \mu_q}{T_{ch}}\right) \exp\left(\frac{S_i \mu_s}{T_{ch}}\right) \quad (5.1)$$

where T_{ch} is chemical freeze-out temperature, γ_s is strangeness saturation factor, μ_q is chemical potentials for $u/\bar{u}/d/\bar{d}$ quarks, and μ_s is for s/\bar{s} quarks. m_i is mass of particle species i , g_i is number of spin-isospin degree of freedom. Q_i and S_i are net numbers of valence u/d quarks and s quark of particle species i , respectively. K_2 is the second-order modified Bessel function. Note that we use the Boltzmann approximation for all hadrons except for pions, where the Bose distribution is applied. The resonance decay to lower mass hadrons after chemical freeze-out is also taken into account. Known resonances up to mass of $1.7 \text{ GeV}/c^2$ are included. Since the data are taken in mid-rapidity region, therefore we do not apply any conservation laws.

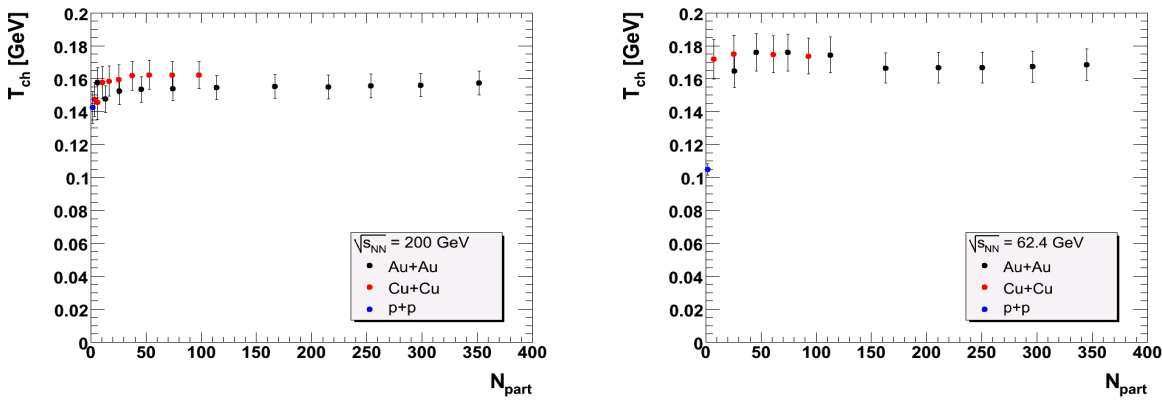


Figure 5.2: Chemical freeze-out temperature T_{ch} as a function of N_{part} in Au+Au/Cu+Cu/p+p collisions at $\sqrt{s_{NN}} = 200 \text{ GeV}$ (left) and 62.4 GeV (right).

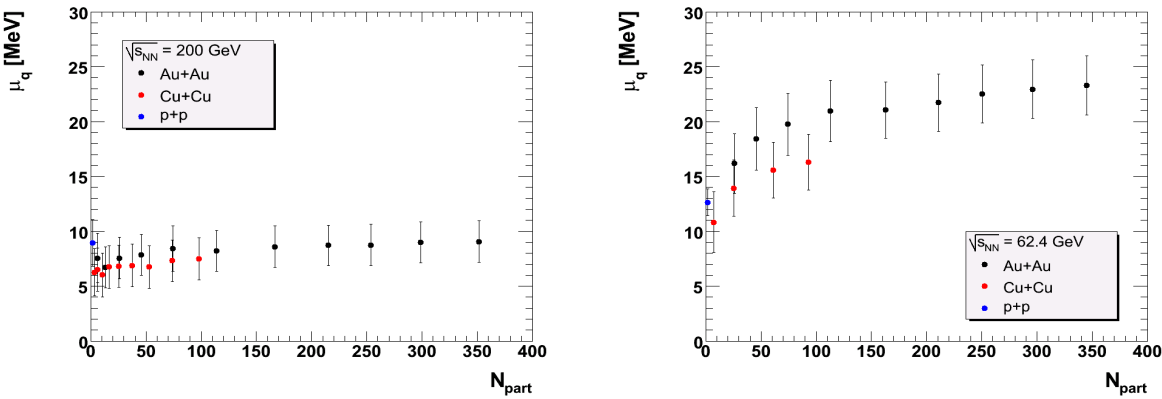


Figure 5.3: Chemical potential μ_q a function of N_{part} in Au+Au/Cu+Cu/p+p collisions at $\sqrt{s_{NN}} = 200 \text{ GeV}$ (left) and 62.4 GeV (right).

Chemical freeze-out temperature T_{ch} is found to be independent of collision centrality as shown in Figures 5.2 and 5.3. We obtain almost the same $T_{ch} \sim 160$ MeV at $\sqrt{s_{NN}} = 62.4, 200$ GeV. It is universal to both elementary (p+p) and heavy ion collisions (Au+Au, Cu+Cu). Small but finite chemical potential μ_q reflects that net baryon density is small but not zero around mid-rapidity. The chemical potential is larger at 62.4 GeV than at 200 GeV. The centrality dependence of chemical potential μ_q is almost flat at 200 GeV, but at 62.4 GeV it increases with N_{part} . The increase is consistent with larger baryon stopping in central collisions. Between Au+Au and Cu+Cu collision systems, T_{ch}, μ_q are scaled with N_{part} . As well as particle abundances dN/dy, particle ratios and chemical freeze-out properties are controlled just by the system size at the same $\sqrt{s_{NN}}$.

As a conclusion of this section, we can say that hadrons are emitted from a thermal source. It is locally chemically equilibrated. The degree to which chemical equilibrium among hadrons is established provides important constraints on microscopic chemical reaction processes and their timescales. Since strangeness saturation factor γ_s (in Equation 5.1) increases with N_{part} , the degree of chemical equilibrium including strange quarks is more higher in central collision than in peripheral collisions. In this sense, the thermalization may reach up to a certain level even in a small system p+p collisions.

The chemical freeze-out temperature is flat in centrality, and near the critical temperature T_c (~ 170 MeV) predicted from lattice QCD calculation. Hadronic scatterings from hadronization to chemical freeze-out must be negligible because they would result in dropping T_{ch} . So the observed chemical equilibrium cannot have been generated via hadronic scatterings due to the short time duration between chemical freeze-out and hadronization.

Nevertheless the picture of thermal hadron production does not require the existence of parton phase. It is important to understand if and how the thermal properties of the observed hadrons relate to the thermal properties of quarks and gluons in the QGP. We will discuss this topic in Section 5.1.2.

5.1.2 Kinetic Freeze-out – Blast-wave Model Fit

In Section 5.1.1, we discussed chemical freeze-out properties using p_T -integrated yields and their ratios. On the other hand, the spectral shape of p_T spectra also contains information about hadron production mechanisms and final-state interactions between produced hadrons. The measured hadron spectra reflects properties at the stage when hadrons stop interacting. This moment is called kinetic (thermal) freeze-out. In p+p collisions, p_T spectra are well described by m_T -exponential function at low p_T . This is called “ m_T scaling” between different particle species. This means that m_T -exponential slope parameters (or equivalently mean p_T) are the same between particle species. This scaling implies that initial parton distributions dominate the particle production process [45]. However, from previous studies at SPS, m_T scaling does not work in heavy-ion collisions. As shown in Figure 5.4, mean transverse momentum $\langle p_T \rangle$ has a clear mass dependence. $\langle p_T \rangle$ linearly increases with hadron mass. If a thermal source for all hadron species is boosted with the same velocity in radial direction, the expansion should result in such a characteristic mass dependence as observed here. Thus, the observation is consistent with a radial collective flow picture. In central collisions, $\langle p_T \rangle$ for any hadron species is larger than in

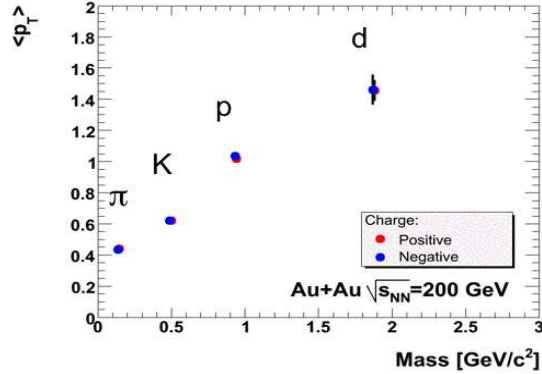


Figure 5.4: Mean transverse momentum $\langle p_T \rangle$ vs. hadron mass in 0-5% (0-20% for d, \bar{d}) central Au+Au collisions at $\sqrt{s_{NN}} = 200$ GeV.

peripheral (see Figure 4.14). Especially the increase of (anti)protons is significant. This means that the radial flow velocity is larger in central collisions. Moreover, N_{part} scaling in $\langle p_T \rangle$ is also observed between Au+Au and Cu+Cu systems as well as particle abundances dN/dy . The next question is: what causes the radial flow. We think now that it is scatterings among constituents in the collision overlap region. The constituents are quarks and gluons before hadronization, then hadrons after hadronization. The scatterings convert density gradients into outward pressure gradients resulting in radial collective flow.

In theoretical model, relativistic hydrodynamic calculations reproduce the data well at low p_T [27]. A separation of thermal motion and collective flow requires a thermal model based on such a hydrodynamic approach. Several models have been developed to reproduce the measured hadron momentum spectra. Such models use concepts borrowed from relativistic hydrodynamics but they do not include the complete time evolution of the system. They contain essential freeze-out features of the hydrodynamic calculation. For this reason, they are called hydro-inspired models. Hydro-inspired models are a very effective parameterization of the final state, that use few parameters with clear physical interpretation.

A so-called blast-wave model is one of them. The blast-wave model originates from the paper [46], where a relativistic formula for particle distribution corresponding to a thermalized and radially expanding system was first given. Assuming (1) longitudinal boost-invariance, (2) cylindrically symmetric systems, (3) freeze-out occurs instantaneously at all radii, (4) the Cooper-Frye formula [47] leads to the following formulation [48]:

$$\frac{dN}{m_T dm_T} \propto \int_0^R r dr m_T I_0\left(\frac{p_T \sinh \rho}{T_{fo}}\right) K_1\left(\frac{m_T \cosh \rho}{T_{fo}}\right) \quad (5.2)$$

$$\beta_T(r) = \beta_s \left(\frac{r}{R}\right)^n \quad (5.3)$$

where $m_T = \sqrt{p_T^2 + m^2}$, $\rho(r) = \tanh^{-1} \beta_T(r)$. The velocity profile in radial direction should be fixed since the variation can affect the absolute yield at extrapolated high p_T . We have tested different velocity profiles with changing n values as follows:

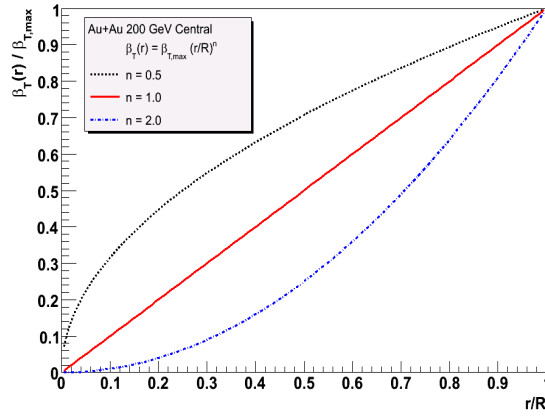


Figure 5.5: Velocity profile $\beta_T(r)/\beta_{T,\max}$ in radial direction for different n .

Table 5.1: $\chi^2/\text{n.d.f.}$ (n.d.f = 46) values for combinations of n and centrality range in 200 GeV Au+Au collisions. $\beta_T(r) = \beta_s(\frac{r}{R})^n$.

	n=0.5	n=1.0	n=2.0
Central	5.3	2.8	3.7
Mid-central	3.5	1.6	1.9
Peripheral	3.4	2.8	1.8

We found that $n = 1.0$ is a reasonable number. Also this is consistent with results of full hydrodynamic calculations [27]. In the following analysis, n is set to be 1.0 (linear velocity profile). The blast-wave model does not predict the absolute normalizations of the spectra, hence extra parameters are required to normalize each spectra. This part is now done by the statistical model described in Section 5.1.1.

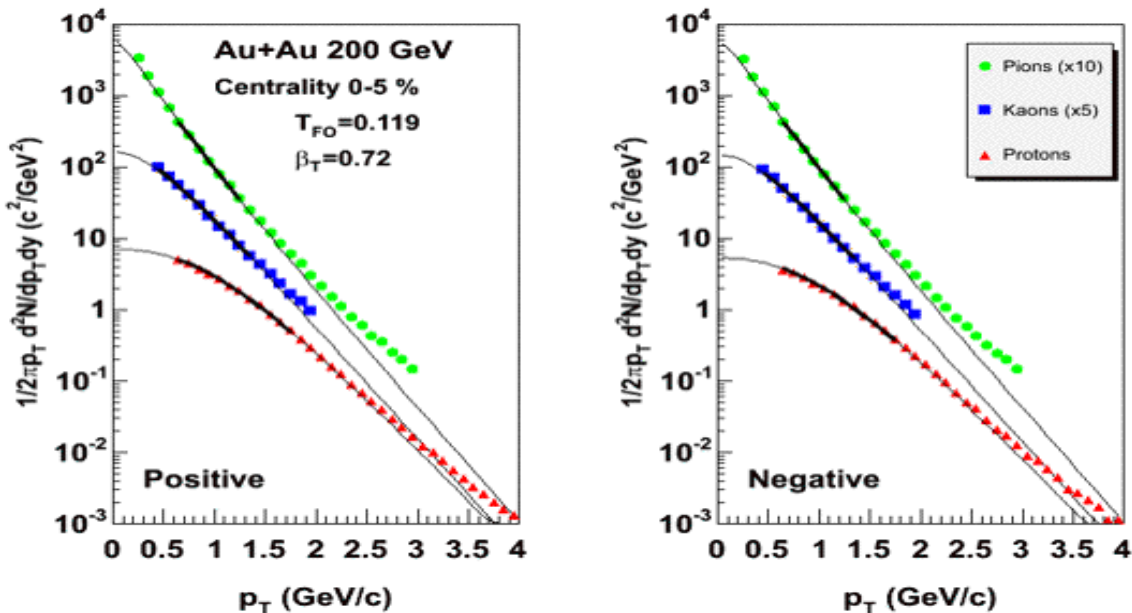


Figure 5.6: p_T spectra for $\pi/K/p$ in Au+Au collisions at $\sqrt{s_{NN}} = 200$ GeV with Blast-wave fitting result (see text for detail).

The measured p_T spectra are fitted with the above function for $\pi/K/p$ simultaneously (see Figure 5.6). The transverse flow velocity and kinetic freeze-out temperature are extracted. From previous studies [49], kinematics of resonance decays results in very steeply dropping daughter pion spectra and raise considerably the total pion yield at low- p_T region (<0.5 GeV/c). To minimize the contribution from resonance decays, we apply tight p_T cuts in the fitting (π : 0.6-

$1.2 \text{ GeV}/c$ K: $0.4\text{-}1.4 \text{ GeV}/c$, p,\bar{p} : $0.6\text{-}1.7 \text{ GeV}/c$). The high- p_T cut off is set to be $m_T - m < 1.0 \text{ GeV}/c^2$ for rejecting hard component of spectra.

To study the parameter correlations, we make a grid of (T_{fo}, β_T) pairs and then perform a χ^2 minimization for each particle type. We observe that the parameter T_{fo} and β_T are anti-correlated as shown in Figure 5.7, since the spectra can be made flatter by increasing either the temperature or the transverse flow. Different particles have different sensitivity to the parameters. For example, heavier particles are more sensitive to the radial flow velocity than to the kinetic freeze-out temperature. This ambiguity in $T_{fo}\text{-}\beta_T$ can be removed by fitting spectra simultaneously for different mass particles and searching for overlap region in $T_{fo}\text{-}\beta_T$ plane. The contours of six particle species overlap at a single common point within 3σ level.

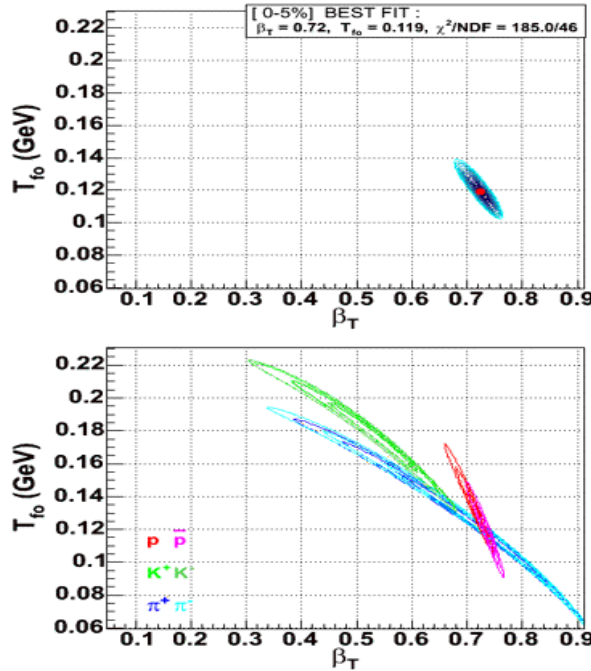


Figure 5.7: χ^2 contour map as a function of T_{fo} and β_T for $\pi/K/p$ in Au+Au collisions at $\sqrt{s_{NN}} = 200 \text{ GeV}$ (top: combined, bottom: separate for $\pi/K/p$).

The extracted parameters are shown in Figures 5.8 and 5.9. The kinetic freeze-out temperature T_{fo} and flow velocity $\langle\beta_T\rangle$ depend on collision centrality. In more central collisions, freeze-out occurs at lower temperature and with larger radial flow than in peripheral collisions. In central Au+Au collisions, T_{fo} is about $\sim 120 \text{ MeV}$, $\langle\beta_T\rangle$ is about $\sim 0.5c$. As expected, the kinetic freeze-out temperature is lower than chemical freeze-out temperature. This provides an evidence for further expansion in the duration from chemical to kinetic freeze-out, driving the system to lower temperature.

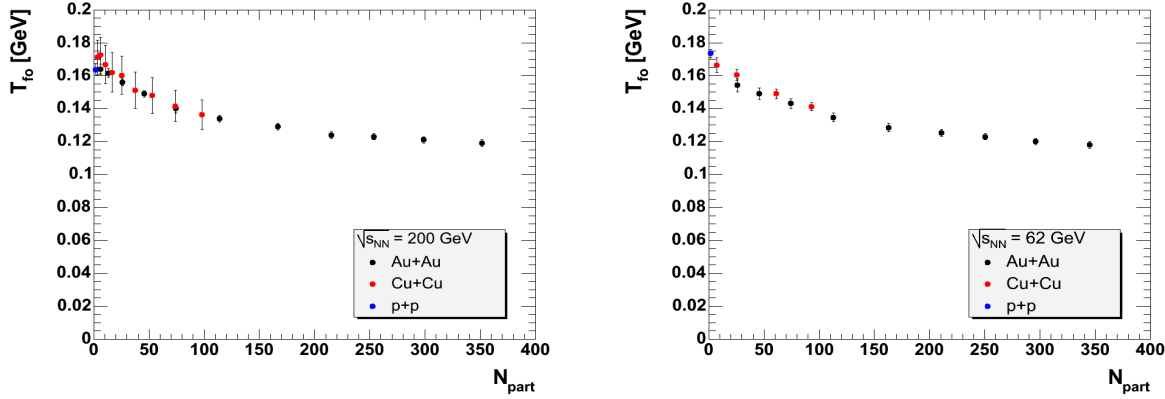


Figure 5.8: Transverse flow velocity as a function of N_{part} in Au+Au/Cu+Cu/p+p collisions at $\sqrt{s_{NN}} = 200$ GeV (left) and 62.4 GeV (right).

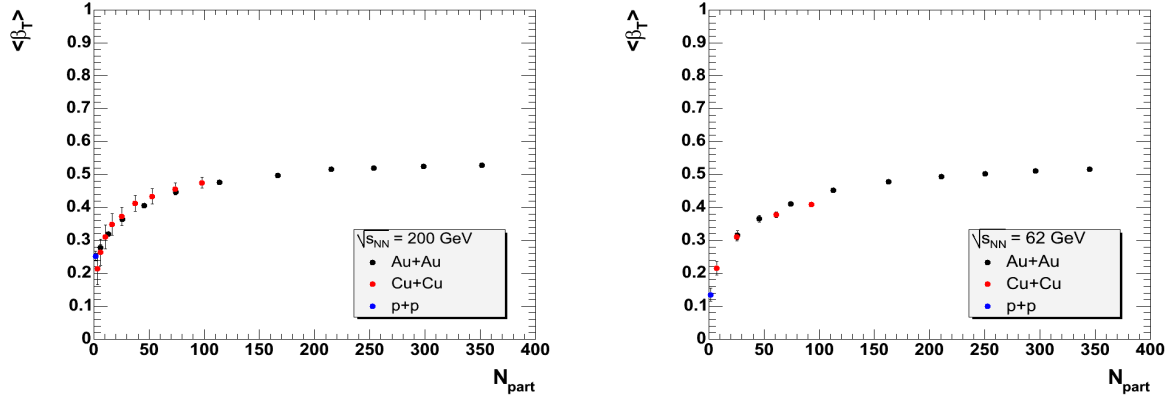


Figure 5.9: Kinetic freeze-out temperature as a function of N_{part} in Au+Au/Cu+Cu/p+p collisions at $\sqrt{s_{NN}} = 200$ GeV (left) and 62.4 GeV (right).

We can see N_{part} scaling again, which is of T_{fo} and $\langle \beta_T \rangle$ between Au+Au and Cu+Cu systems. And we obtain almost same T_{fo} and $\langle \beta_T \rangle$ at $\sqrt{s_{NN}} = 62.4, 200$ GeV. On the other hand, a finite transverse flow is observed even in p+p. Is thermal behavior expected in a small system p+p? There may be no established mechanism which makes local thermal equilibrium possible in p+p collisions. This kind of discussion is similar to that in chemical freeze-out. So, the degree of thermalization in small system is another and important topic. Here we assume local thermal equilibrium in heavy ion collisions which is a larger system.

To study the relation between the freeze-out time and system size, we compare the freeze-out parameters with a simple adiabatic expansion model (ideal gas ; $P = (1/3)\epsilon$, P : pressure, ϵ : energy density). This model includes longitudinal expansion with the velocity of light and radial expansion with the extracted flow velocity β_T . With thermodynamics relations, we obtain

$$s \propto T^3 \quad (5.4)$$

where s is the entropy density, T is the temperature. The conservation of total entropy is

$$s(t)V(t) = s(t_0)V(t_0) \quad (5.5)$$

$$V(t) = t\pi(R_0 + \beta_T t)^2 \quad (5.6)$$

t_0 is a given initial time. R_0 is the radius of the overlap region. $T_0 = T(t_0)$. Then, we obtain the time dependence of temperature

$$T(t) = T_0 \left(\frac{t_0(R_0 + \beta_T t_0)^2}{t(R_0 + \beta_T t)^2} \right)^{1/3} \quad (5.7)$$

Since the system size increases with time, the mean free path $L(t)$ increases with time. We define a freeze-out time t_{fo} when $L(t)$ is equal to radial size $R(t)$. In this case, t_{fo} is 1-parameter function, which is determined by the most central freeze-out parameters.

$$L(t) = \frac{V(t)}{\alpha N_p \sigma} = \frac{t\pi(R_0 + \beta_T t)^2}{\alpha N_p \sigma} \quad (5.8)$$

$$R(t) = R_0 + \beta_T t \quad (5.9)$$

where α is a proportionality coefficient for the total number of particles, N_p is the number of nucleon participants, and σ is the cross section. From a $L(t) = R(t)$ relation, we obtain

$$t_{fo} = (\sqrt{R_0^2 + 4\beta_T K N_p} - R_0)/2\beta_T \quad (5.10)$$

where $K (= \alpha\sigma/\pi)$ is a free parameter which is determined by a centrality bin. Substituting t_{fo} to Equation 5.7, we have the freeze-out temperature T_{fo} . Figure 5.10 (left) shows temperature as a function of time with a common fixed freeze-out time (10 fm/c). Because the freeze-out temperature is lower in central than in peripheral, the magnitude relation does not change even reversing in time. The peripheral temperature is higher than central one at any time. We scale temperature at $\tau = 1$ fm/c with Bjorken energy density $\epsilon_{Bj}\tau$ (see Figure 1.5) and a $\epsilon_{Bj} \propto T^4$ relation. The most central freeze-out time is fixed at 10 fm/c. As shown in Figure 5.10 (right), the central temperature is higher than peripheral one as expected. Then, we compare the model prediction with other centrality bins. This simple model reproduces the result well (see Figure 5.11). In summary, the centrality dependence of freeze-out temperature is explained only by the change of the system size (N_{part}), resulting in a N_{part} scaling. The difference of freeze-out temperatures between chemical and kinetic freeze-out's shows a finite expansion time at hadronic stage. The expansion time is more longer in central than in peripheral.

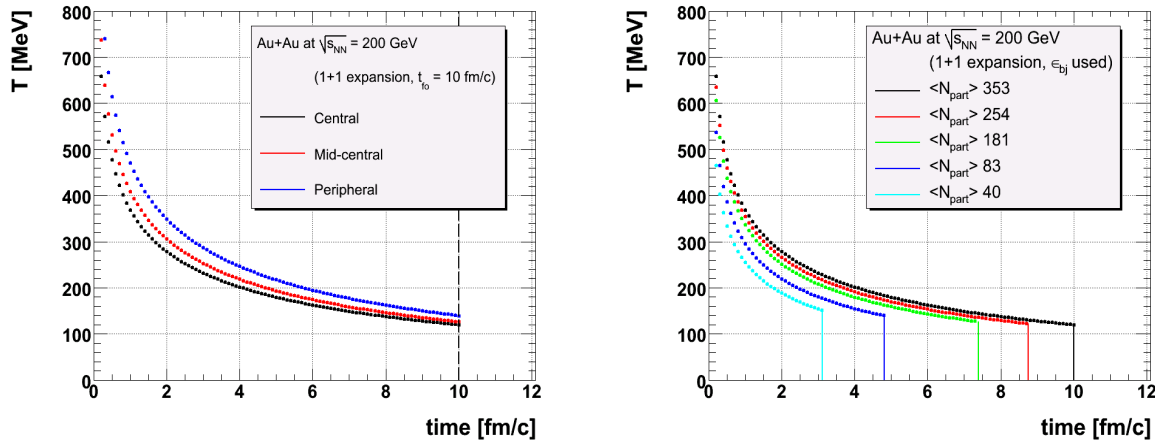


Figure 5.10: Left: Temperature as a function of time with a common fixed freeze-out time (10 fm/c). Right: Temperature as a function of time with scaled temperatures at $t = 1$ fm/c.

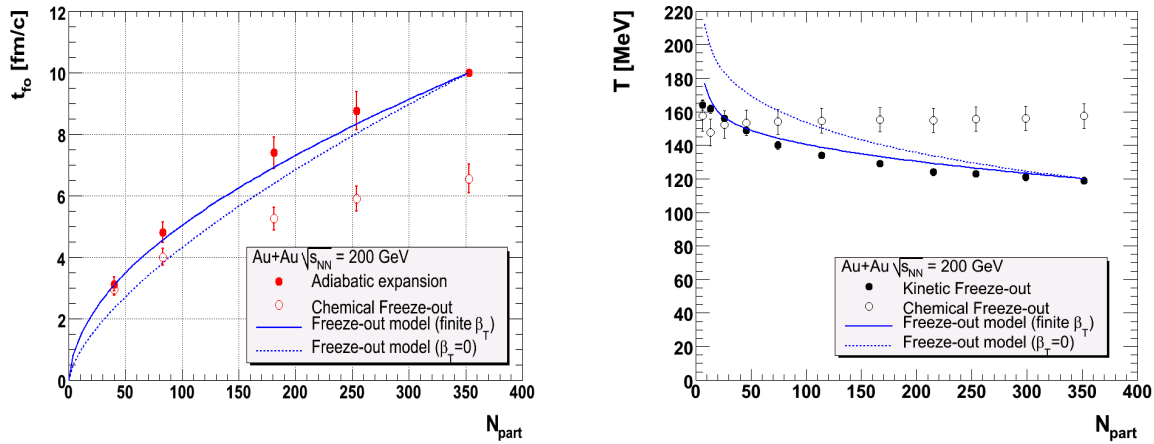


Figure 5.11: Freeze-out time (left) and temperature (right) as a function of N_{part} .

We emphasized N_{part} scaling between Au+Au and Cu+Cu systems several times. It is observed in hadron abundances (dN/dy) and chemical/kinetic freeze-out properties. We can say that the number of participants N_{part} , representing the system size, is a key parameter to explain bulk properties of the collision system. For the positive correlation of $N_{part}^{1/3}$ and system size, results of HBT radii measurements can be referred [50]. Geometrical shape of the overlapped region does not affect the properties. In short, Cu+Cu looks like peripheral Au+Au. And peripheral Au+Au/Cu+Cu approaches p+p.

In this sense, the next question is: “Is there another key parameter for bulk properties?” An important observable is v_2 (elliptic flow coefficient). We test the scaling of v_2 between different collision systems below. Figure 5.12 (left) shows v_2 as a function of N_{part} for different p_T for charged hadrons in Au+Au/Cu+Cu at $\sqrt{s_{NN}} = 200$ GeV. v_2 does not look scaled by N_{part} in the region $N_{part} \sim 80$. In non-central heavy-ion collisions, the initial overlap zone between the colliding nuclei is spatially deformed. If the constituents produced in the reaction zone rescatter efficiently, this spatial anisotropy gets transferred to momentum space. The initial spatial eccentricity should rather be an appropriate variable. The eccentricity is calculated within a Glauber model, assuming the minor axis of the overlap region to be along the impact parameter vector. Actually v_2 looks scaled by this eccentricity shown in Figure 5.12 (right). It is also reported that v_2 is scaled by participant eccentricity, which accounts for nucleon position fluctuations in the colliding nuclei [51].

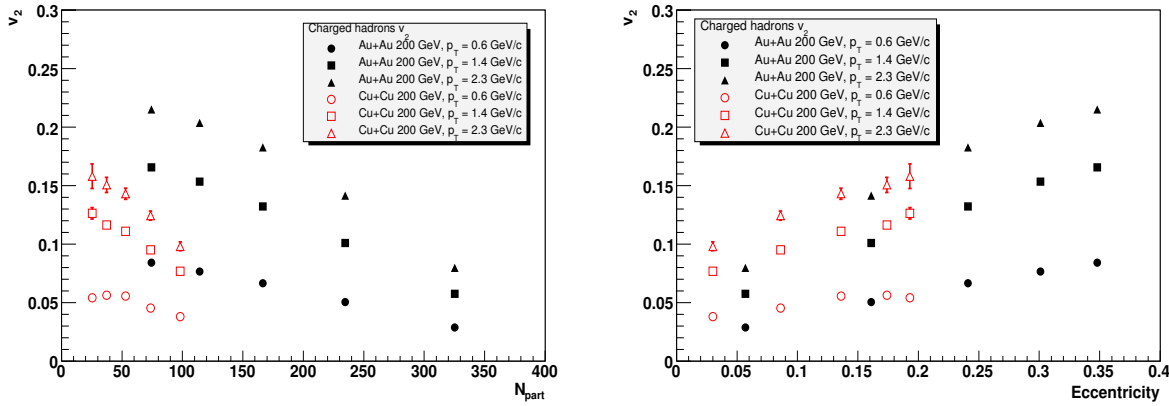


Figure 5.12: v_2 as a function of N_{part} (left) and eccentricity (right) for different p_T for charged hadrons in Au+Au/Cu+Cu at $\sqrt{s_{NN}} = 200$ GeV [22].

In summary, soft components show a similarity in chemical/kinetic freeze-out properties between $\sqrt{s_{NN}} = 200$ GeV and 62.4 GeV. Only baryon chemical potential shows the difference due to the difference of baryon number transport. This difference affects the normalization of p_T spectra. It does not affect the spectral shape anyway. Freeze-out properties are almost same when comparing them at same N_{part} between Au+Au and Cu+Cu.

At significantly larger p_T the thermal picture begins to give way to hard power-law component and the slopes can no longer be interpreted in a collective flow picture. Next we look at this switching region from soft to hard hadron production using a two-component model (see Section 5.2.2).

5.2 Hadron Production at Intermediate p_T

5.2.1 Proton and Antiproton Enhancement

The p_T dependence of particle ratios provides more insights to the hadron production. Especially p/π ratio is focused on in this section in terms of the baryon enhancement. Fig. 5.13 shows p/π^+ (\bar{p}/π^-) ratios as a function of p_T for different centralities in Au+Au and Cu+Cu collisions at $\sqrt{s_{NN}} = 200$ GeV. The p/π ratios in the intermediate p_T range (2-5 GeV/c) show a clear centrality dependence, higher relative proton production in more central collisions. In central collisions, the p/π ratio shows that approximately equal amounts of protons and pions are produced in the momentum range of $p_T = 2-4$ GeV/c. This is significantly higher than the results in elementary collisions (p+p, $e^+ + e^-$) or pQCD calculations, $p/\pi \sim 0.2$ [52, 53]. In the most peripheral collisions, the values are consistent with p+p values. A definite turnover is observed for all centrality classes. The peak position is at 2-3 GeV/c, independent of centrality. Beyond the peak, the ratios are falling toward the values in p+p collisions. The observed behavior indicates a transition from soft to hard hadron production at intermediate p_T . At least, the large baryon enhancement at intermediate p_T indicates that the dominant source of hadron production in this p_T range is not jet fragmentation.

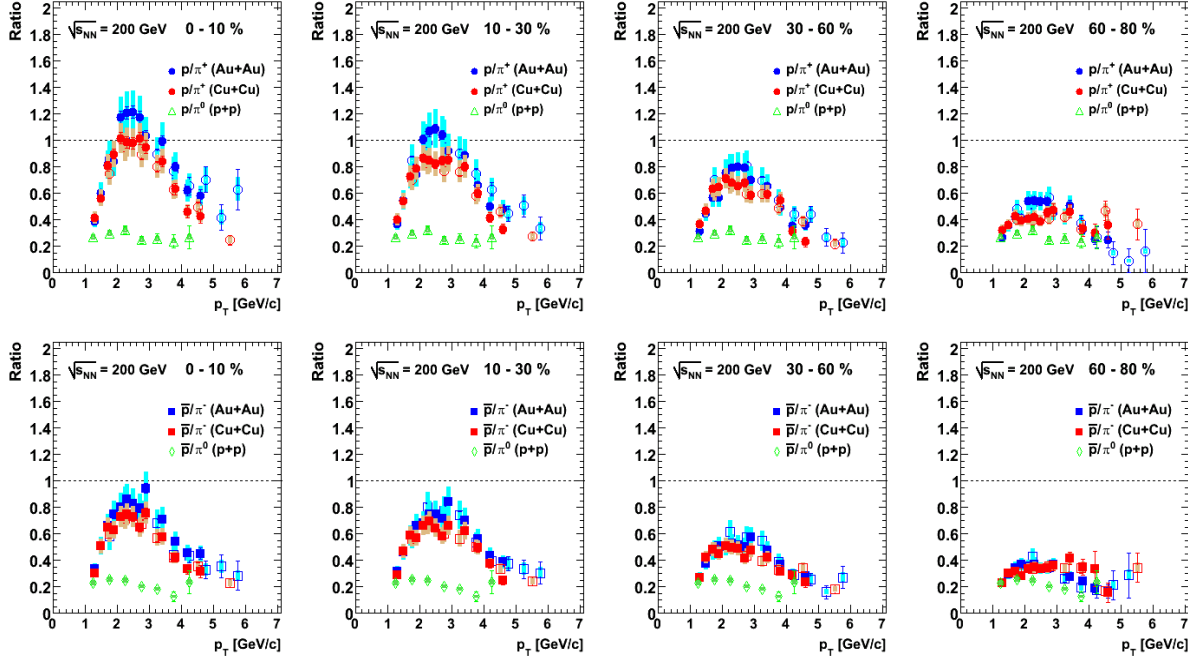


Figure 5.13: p/π^+ (top) and \bar{p}/π^- (bottom) ratios as a function of p_T for different centralities in Au+Au/Cu+Cu/p+p collisions at $\sqrt{s_{NN}} = 200$ GeV.

The baryon enhancement is also observed in nuclear modification factors (R_{AA} , R_{CP}) (see Section 4.5). If jet fragmentation dominates for the hadron production in intermediate p_T region and parton energy loss in the created matter is the same between quarks and gluons, one should expect similar values of R_{CP} for pions and protons. But we do not see such a behavior of R_{CP} . This means that soft hadron production like radial flow effect may still be significant even at this p_T . However at higher p_T we observe an approaching trend of proton R_{CP} into pion R_{CP} . The observed behavior indicates a transition from soft to hard hadron production (jet fragmentation with energy loss) at intermediate p_T .

The lower energy data provides an important information on the baryon production and transport at mid-rapidity. Figure 5.14 shows the p/π^+ (\bar{p}/π^-) ratios as a function of p_T in Au+Au and Cu+Cu collisions at $\sqrt{s_{NN}} = 62.4$ GeV. The ratios show a peak structure around 2-3 GeV/c and a centrality dependence as seen at $\sqrt{s_{NN}} = 200$ GeV. Comparing to the 200 GeV data, the 62.4 GeV data shows a larger proton contribution at intermediate p_T , while there is a less antiproton contribution. These observations are related to the following points: (1) larger difference between the slopes of spectra from thermal emission and jet fragmentation at 62.4 GeV than that at 200 GeV [54]. The p_T spectra at 62.4 GeV is steeper than that at 200 GeV. The steepness reflects the difference in initial jet production at the two collision energies, (2) larger baryon chemical potential at 62.4 GeV than that at 200 GeV, (3) stronger transport of baryon number from the incoming beams to midrapidity at lower energy. In order to separate baryon number transport from the baryon enhancement, antiproton is a good probe to study the baryon enhancement than proton which is more affected by baryon number transport process.

Another thing to be taken into account is $p-\bar{p}$ annihilation in hadron gas at late collision stage. In the limiting case that thermal motion ($T \sim 120$ MeV) is dominant without collective flow, the relative momentum between particles is ~ 500 MeV ($\beta \sim 0.4$). The experimental $p-\bar{p}$ annihilation cross section is ~ 100 mb at $p = 500$ MeV [55]. On the other hand, proton number density in hadron gas (central collision) is estimated as follows: proton yield at mid-rapidity dN^p/dy is ~ 18 , and the freeze-out volume V_{fo} is $\sim 1.1 \times 10^3$ fm 3 at $\tau = 10$ fm/c (see Section 5.1.2), so the proton number density is $n^p = (dN^p/dy)/V_{fo} = \sim 1.7 \times 10^{-2}$ fm $^{-3}$. The mean free path λ for annihilation is ~ 5.9 fm. The duration time of hadron gas Δt is estimated to be ~ 4 fm/c. From these numbers, the survival rate of antiprotons is $\exp(-\beta\Delta t/\lambda) \sim 0.76$. This rate reduces the \bar{p}/p ratio with $\sim 10\%$ for $\bar{p}/p = 0.7$. With higher p_T , the annihilation cross section is very small.

Proton and antiproton enhancement at intermediate p_T is observed in all collision systems. The p_T dependence in Cu+Cu is similar to that in Au+Au. Figure 5.15 (left) shows p/π^+ (\bar{p}/π^-) ratio as a function of $N_{part}^{1/3}$ at $p_T = 2-3$ GeV/c in Au+Au/Cu+Cu collisions at $\sqrt{s_{NN}} = 200$ GeV. Even though the overlapped region of colliding nuclei has a different geometrical shape for the same number of participating nucleons N_{part} , the data shows similar system size dependences in both systems. This could be called N_{part} scaling on p/π ratio at the same collision energy. The

N_{part} scaling is also observed at lower energy $\sqrt{s_{NN}} = 62.4$ GeV between Au+Au/Cu+Cu (see Section 4.4.2). On the other hand, the N_{part} scaling is not observed between different energies 62.4 GeV and 200 GeV in Au+Au. Instead, transverse energy per unit pseudo-rapidity ($dE_T/d\eta$) is useful for such scaling between different collision energies as shown in Figure 5.15 (right). Indeed \bar{p}/π^- ratio is scaled with $dE_T/d\eta$ ($(dE_T/d\eta)^{1/3}$ used for comparison), but p/π^+ is not scaled. Proton yield at 62.4 GeV is larger than that at 200 GeV. This shows that proton production at 62.4 GeV is partly from baryon number transport, not only proton-antiproton pair production. In conclusion, N_{part} , representing the initial system size, is a control parameter for the baryon enhancement. Transverse energy density $dE_T/d\eta$ is a connection key between different collision energies.

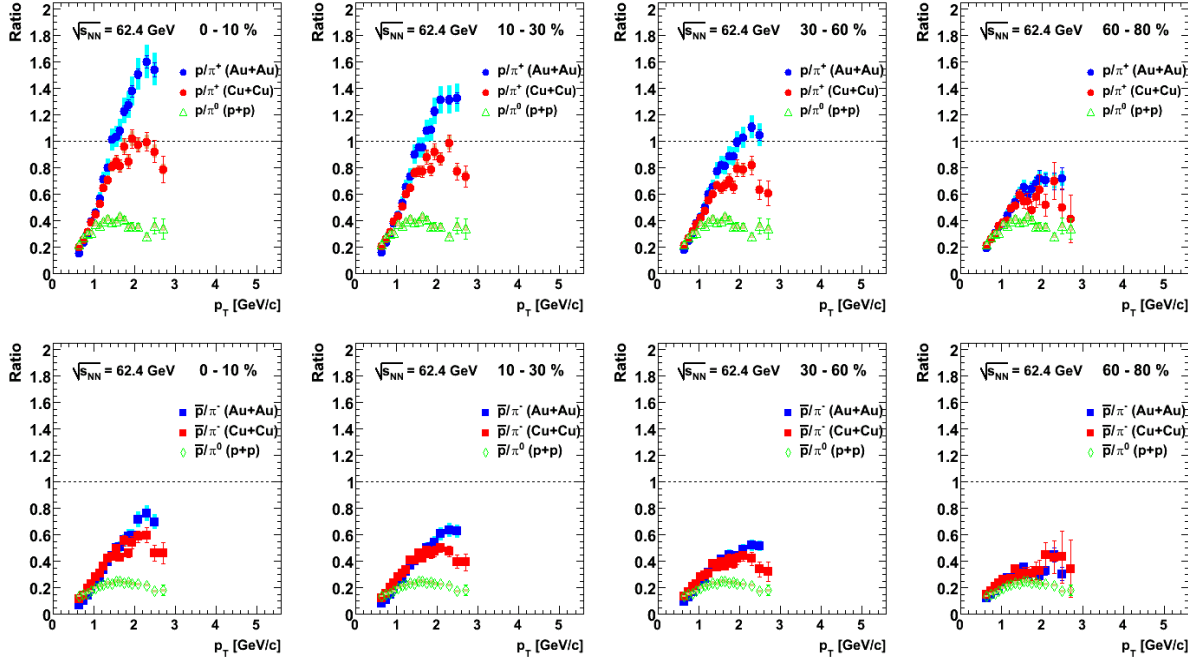


Figure 5.14: p/π^+ (top) and \bar{p}/π^- (bottom) ratios as a function of p_T for different centralities in Au+Au/Cu+Cu/p+p collisions at $\sqrt{s_{NN}} = 62.4$ GeV.

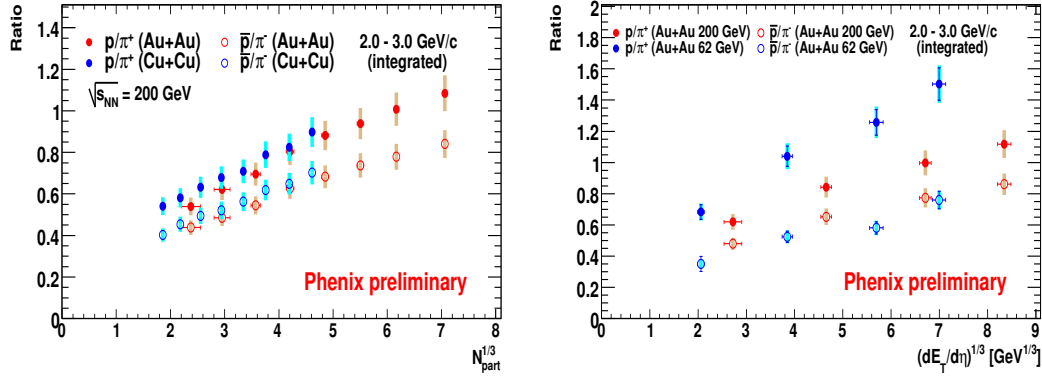


Figure 5.15: Left; p/π ratio as a function of $N_{part}^{1/3}$ for 2-3 GeV/c in Au+Au/Cu+Cu at $\sqrt{s_{NN}} = 200$ GeV. Right; p/π ratio as a function of $(dE_T/d\eta)^{1/3}$ for 2-3 GeV/c in Au+Au at $\sqrt{s_{NN}} = 62.4/200$ GeV.

5.2.2 Two-component Model

As mentioned in Section 5.1.2, low- p_T spectra is described well by hydrodynamical calculations. To extract freeze-out properties, a hydro-inspired model called Blast-wave was used. It is expected that such a hydrodynamic picture will break down at high p_T where partonic cross sections are small and the mean free path is long, meaning that hard partons cannot be brought to thermal equilibrium. In this region, initial hard scattering and jet fragmentation should dominate. Since radial collective flow pushes particles into higher p_T , soft hadrons would be visible at relatively high p_T . We think that a two-component model including both soft and hard hadron production processes is a natural way to describe the hadron production at intermediate p_T . Using the following two-component model, we try to separate soft and hard components for pions and (anti)protons, and to explain the baryon enhancement.

Decomposition of p_T Spectra

The soft and hard components are defined below:

Soft: The soft component uses the result from Blast-wave fit at low p_T . The blast-wave model describes thermal distributions with radial flow. Extrapolation of the thermal distributions to higher p_T is not unrealistic.

$$\frac{dN}{p_T dp_T} \Big|_{soft} = A \int_0^R r dr m_T I_0\left(\frac{p_T \sinh \rho}{T_{fo}}\right) K_1\left(\frac{m_T \cosh \rho}{T_{fo}}\right) \quad (5.11)$$

Hard: The hard component is the p+p spectra normalized by the number of nucleon-nucleon collisions N_{coll} with p_T -independent constant suppression factor. The p+p spectra includes jet fragmentation following initial hard scattering. NLO pQCD or PYTHIA calculations have still ambiguity of fragmentation function especially on baryon spectra. We use our p+p spectra measured in PHENIX as hard component. We assume that each jet event in a single heavy ion collision is independent, thus it is proportional to N_{coll} . The constant suppression factor represents jet quenching effect. At high p_T (> 5 GeV/c), π^0 and charged hadrons R_{AA} show similar suppression and flat p_T dependence. A constant fractional energy loss and a power-law spectrum imply that $R_{AA} = \text{constant}$ as observed.

$$\frac{dN}{p_T dp_T} \Big|_{hard} = R_{AA} \times N_{coll} \times \frac{dN}{p_T dp_T} \Big|_{p+p} \quad (5.12)$$

These two components are added as a two-component description of the spectra.

$$\frac{dN}{p_T dp_T} \Big|_{sum} = \frac{dN}{p_T dp_T} \Big|_{soft} + \frac{dN}{p_T dp_T} \Big|_{hard} \quad (5.13)$$

To avoid double counting between soft and hard components, we introduce a cut-off $p_T = 2$ GeV/c. If we consider feedback of energy lost by jet quenching, we should add the energy loss back to the system. It is found to be about 2% of the total energy in central Au+Au collisions [56]. Hence we safely neglect this feedback effect.

Figures 5.16, 5.17 show comparisons of the two-component description with the data for pions and (anti)protons. The two-component model can successfully describe the spectra for both particle species in Au+Au collisions at $\sqrt{s_{NN}} = 200$ GeV for all centralities. Apparently, there is a large difference between the slopes of the soft and hard spectra. This indicates that there is a rather narrow p_T interval (1-2 GeV/c) in which the dominant hadron production mechanism changes from boosted thermal emission to jets fragmentation with energy loss.

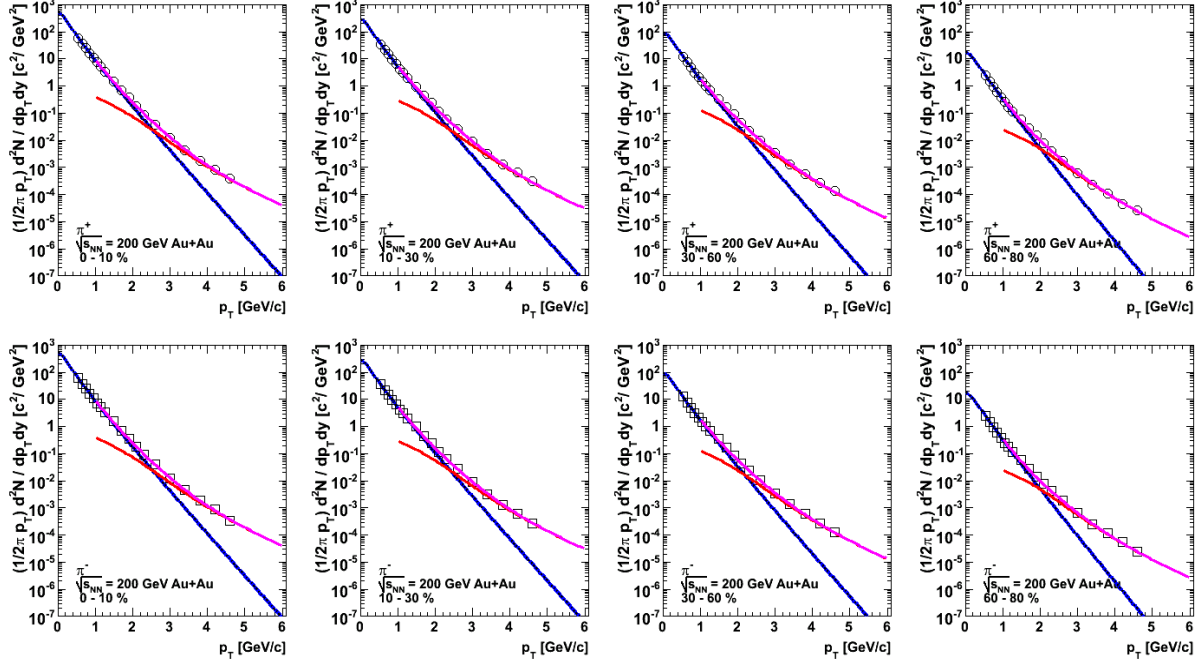


Figure 5.16: p_T spectra for pions in Au+Au collisions at $\sqrt{s_{NN}} = 200$ GeV with lines (blue: soft, red: hard, magenta: soft+hard).

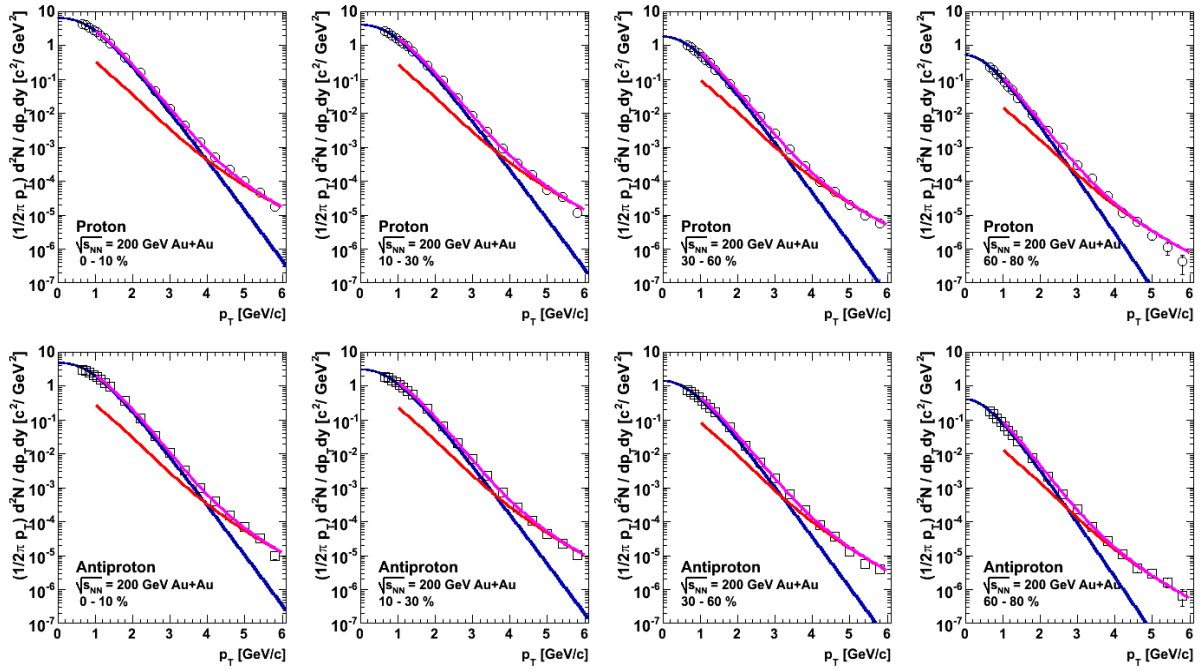


Figure 5.17: p_T spectra for (anti)protons in Au+Au collisions at $\sqrt{s_{NN}} = 200$ GeV with lines (blue: soft, red: hard, magenta: soft+hard).

The extracted R_{AA} is plotted in Figure 5.18. The charged pion R_{AA} is consistent with π^0 's one as expected. The (anti)proton R_{AA} is slightly higher than pion R_{AA} . This suggests the difference of energy loss in the medium between quarks and gluons. Since pions and (anti)protons reflect different sensitivities to quarks and gluons in jet fragmentation process. We will be back to this discussion in Section 5.2.4.

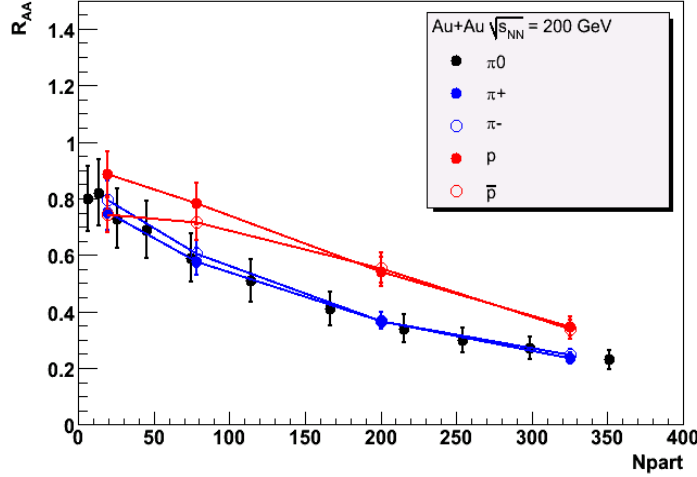


Figure 5.18: Extracted R_{AA} from the 2-component model as a function of N_{part} in 200 GeV Au+Au collisions.

Here we introduce one more assumption. If the constant suppression factor R_{AA} is the same for pions and protons, how well the spectra are reproduced? In this case, the factor is taken from π^0 's R_{AA} results ($p_T > 5$ GeV/c). The same factor is applied for both pions and (anti)protons. The comparisons are shown in Figures 5.19 and 5.20. The pion spectra is well reproduced again as expected. On the other hand, the (anti)proton spectra show residual component around $p_T = 4$ GeV/c. This residual indicates another component such as soft-hard recombination process if our assumption is correct.

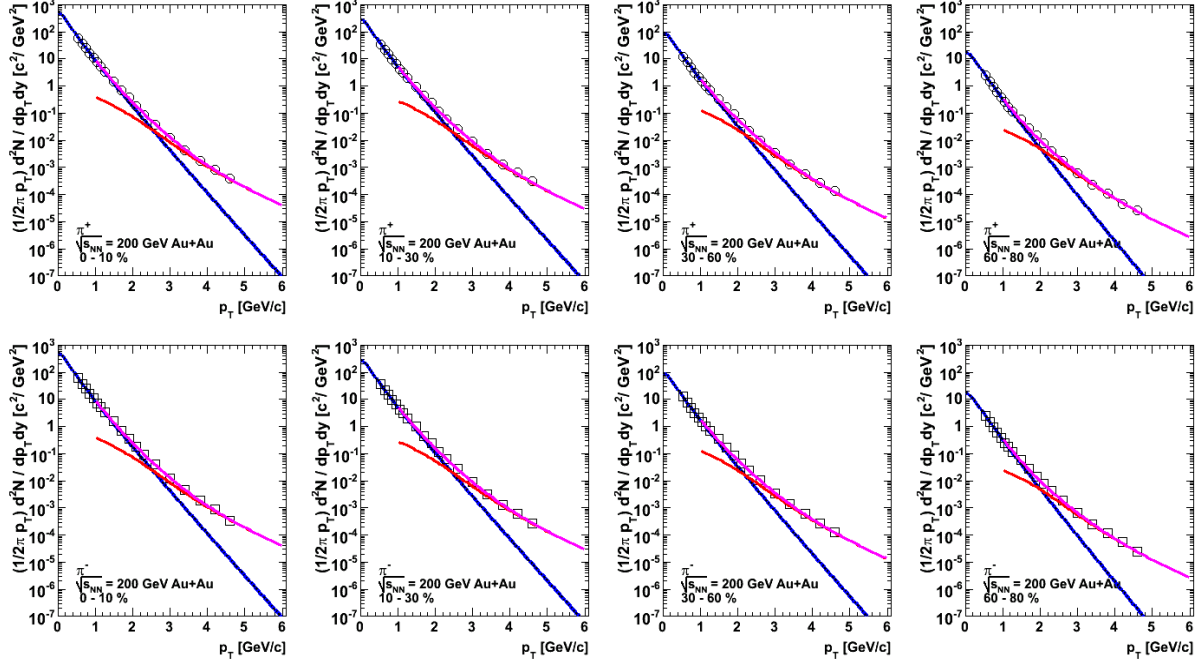


Figure 5.19: p_T spectra for pions in Au+Au collisions at $\sqrt{s_{NN}} = 200$ GeV with lines (blue: soft, red: hard with fixed R_{AA} , magenta: soft+hard).

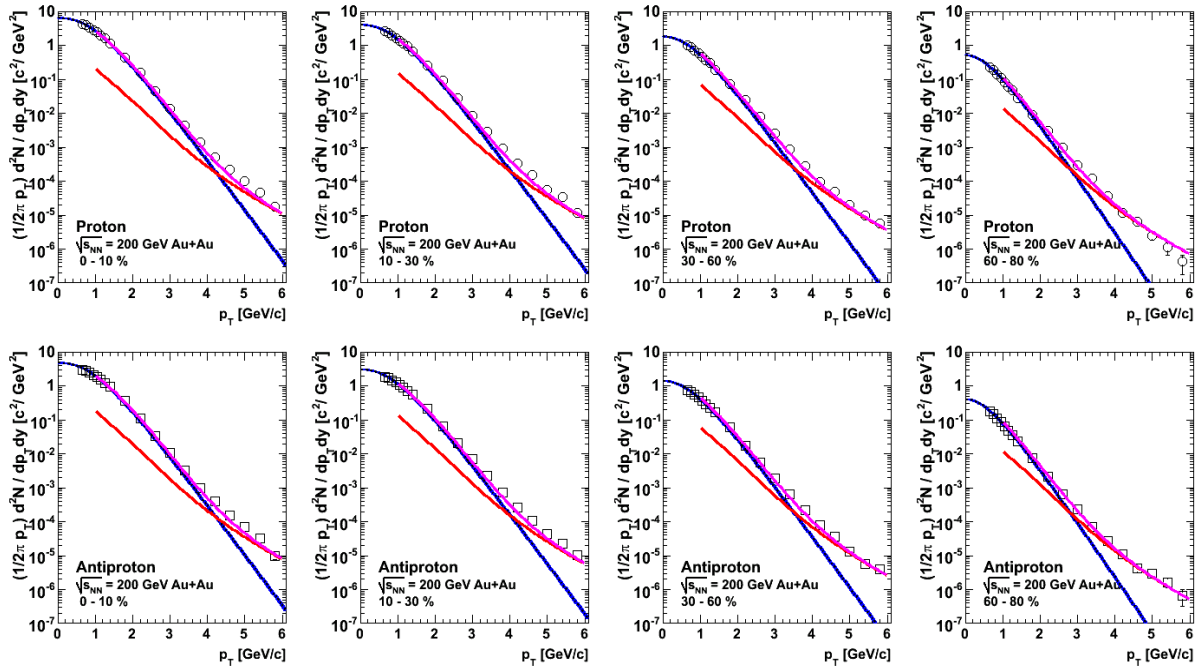


Figure 5.20: p_T spectra for (anti)protons in Au+Au collisions at $\sqrt{s_{NN}} = 200$ GeV with lines (blue: soft, red: hard with fixed R_{AA} , magenta: soft+hard).

Table 5.2: $\chi^2/\text{n.d.f.}$ (n.d.f = 12) for comparisons of 2-component model and data for different centralities in 200 GeV Au+Au collisions. Only statistical error is used.

	0-10%	10-30%	30-60%	60-80%
π^+	1.6	2.0	2.1	2.3
π^-	1.6	1.7	2.1	2.3
p	1.8	2.7	3.0	2.8
\bar{p}	1.9	2.9	3.0	2.6

Table 5.3: $\chi^2/\text{n.d.f.}$ (n.d.f = 12) for comparisons of 2-component model (R_{AA} fixed with π^0) and data for different centralities in 200 GeV Au+Au collisions. Only statistical error is used.

	0-10%	10-30%	30-60%	60-80%
π^+	1.6	2.0	2.1	2.3
π^-	1.6	1.7	2.1	2.3
p	2.1	3.0	3.1	2.8
\bar{p}	2.1	3.3	2.8	2.4

The $\chi^2/\text{n.d.f.}$ (n.d.f. = 12) are summarized in Tables 5.2.2 and 5.2.2. The case of (anti)proton with fixed $\pi^0 R_{AA}$ is somewhat worse than others.

Fraction of Soft/Hard Components

Using our two-component model, we can estimate the fraction of soft and hard components in the measured p_T spectra as shown in Figures 5.2.2 and 5.22. Both soft and hard components are necessary to reproduce the hadron spectra at intermediate p_T (2-5 GeV/c). We can define a crossing point p_T at which soft and hard yields are equal. The crossing point depends on hadron species as shown in Figure 5.25. It moves toward high p_T with higher mass because of radial flow push. It also depends on collision centrality. It is higher in central with the same reason. The soft component has a significant fraction at intermediate p_T . At a given p_T , we have relatively-hard pions and relatively-soft (anti)protons.

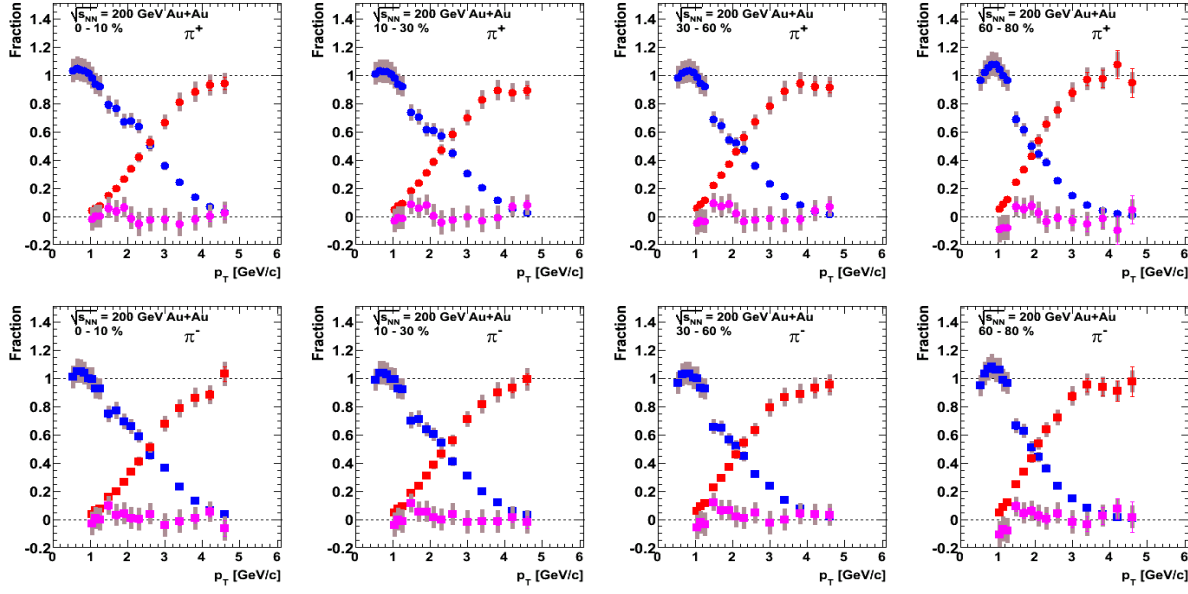


Figure 5.21: Fraction of soft (blue) and hard (red) components for π^+ (top) and π^- (bottom) as a function of p_T in Au+Au collisions at $\sqrt{s_{NN}} = 200$ GeV. The residual fraction is plotted in magenta.

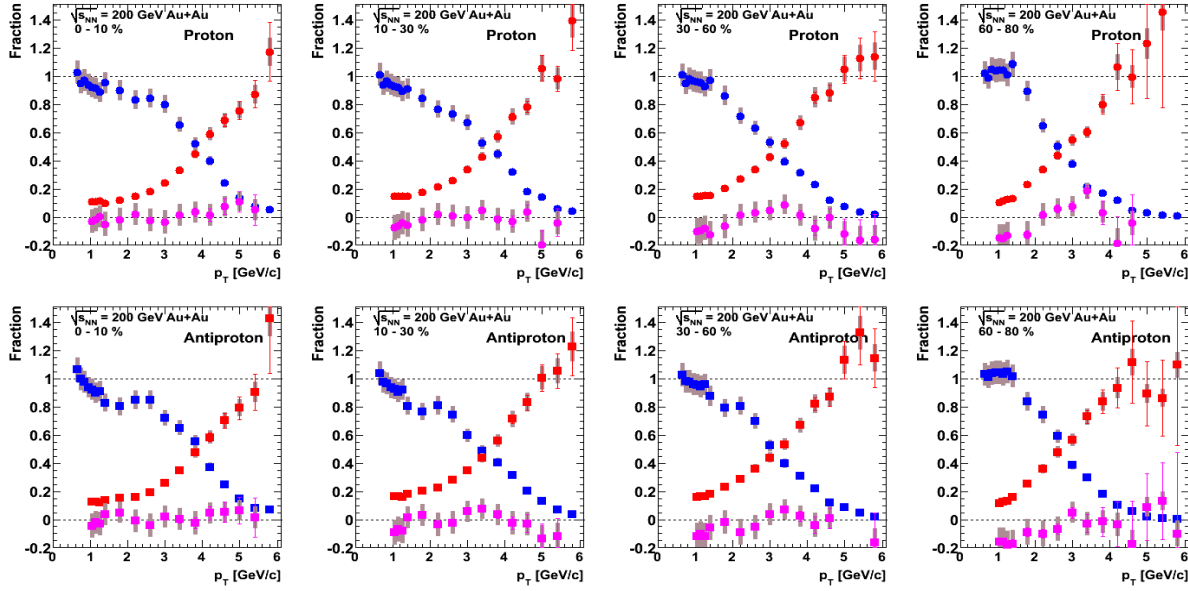


Figure 5.22: Fraction of soft (blue) and hard (red) components for protons (top) and antiprotons (bottom) as a function of p_T in Au+Au collisions at $\sqrt{s_{NN}} = 200$ GeV. The residual fraction is plotted in magenta.

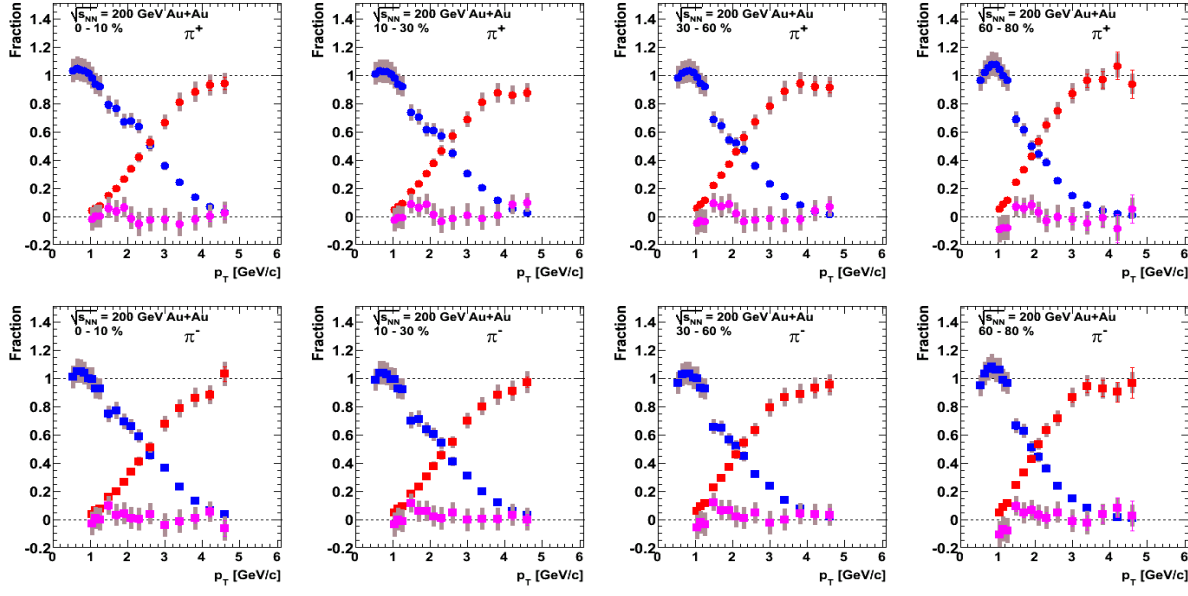


Figure 5.23: Fraction (R_{AA} fixed with π^0 's one) of soft (blue) and hard (red) components for π^+ (top) and π^- (bottom) as a function of p_T in Au+Au collisions at $\sqrt{s_{NN}} = 200$ GeV. The residual fraction is plotted in magenta.

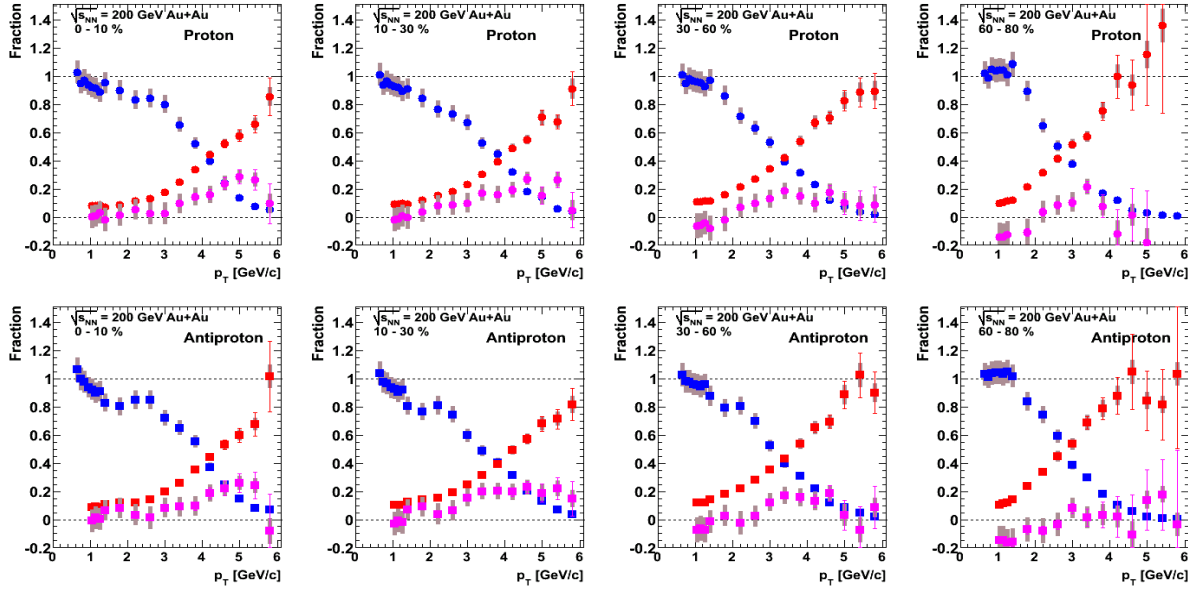


Figure 5.24: Fraction (R_{AA} fixed with π^0 's one) of soft (blue) and hard (red) components for protons (top) and antiprotons (bottom) as a function of p_T in Au+Au collisions at $\sqrt{s_{NN}} = 200$ GeV. The residual fraction is plotted in magenta.

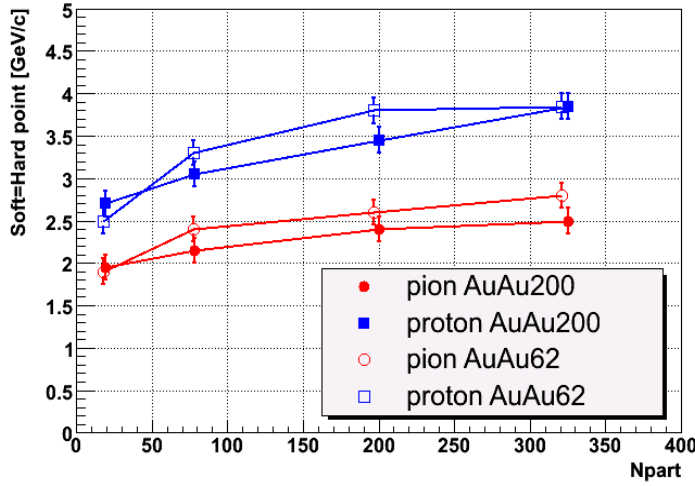


Figure 5.25: Crossing point as a function of N_{part} in Au+Au collisions at $\sqrt{s_{NN}} = 200/62.4$ GeV.

Soft/Hard Separation in Particle Ratios

Particle ratios at low p_T are described by a statistical model (see Section 5.1.1). On the other hand, at high p_T , we expect particle ratios are determined by jet fragmentation which would be universal. How about at intermediate p_T ? We can describe particle ratios by using our two-component model. Figure 5.26 shows p/π^+ (\bar{p}/π^-) ratios with several estimated curves (blast-wave fitting, p+p experimental data, PYTHIA p+p calculation) for (anti)proton soft/hard fractions. The denominator is pions from the data.

$$\frac{p_{data}}{\pi_{data}} = \frac{p_{soft} + p_{hard}}{\pi_{data}} \quad (5.14)$$

We find that radial flow effect, which is represented by blast-wave, could be one of the explanations of the baryon enhancement. Since there is some difference above 2 GeV/c, so other contributions such as jet fragmentation are needed. Hard p/π ratios (data subtracted by blast-wave) are also plotted in the same figure. Figure 5.27 shows \bar{p}/p ratio as a function of p_T . As in p/π ratio, hard \bar{p}/p is estimated. The hard ratios (p/π , \bar{p}/p) are consistent with the values in p+p collisions and PYTHIA calculations.

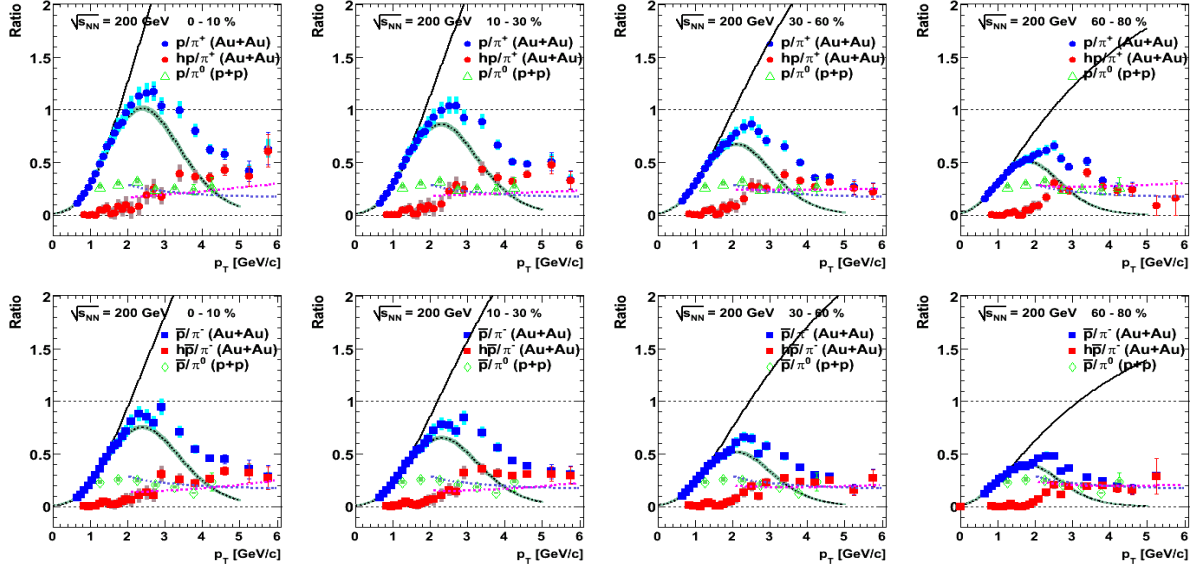


Figure 5.26: p/π^+ (top) and \bar{p}/π^- (bottom) ratios as a function of p_T in Au+Au collisions at $\sqrt{s_{NN}} = 200$ GeV. Blue points are the data. Red points are the estimated ratio (hard component). Black line: blast-wave p/π ratios, black dashed line: blast-wave p divided by π data, magenta dashed line: the scaled $p+p$, cyan dashed line: PYTHIA (see text).

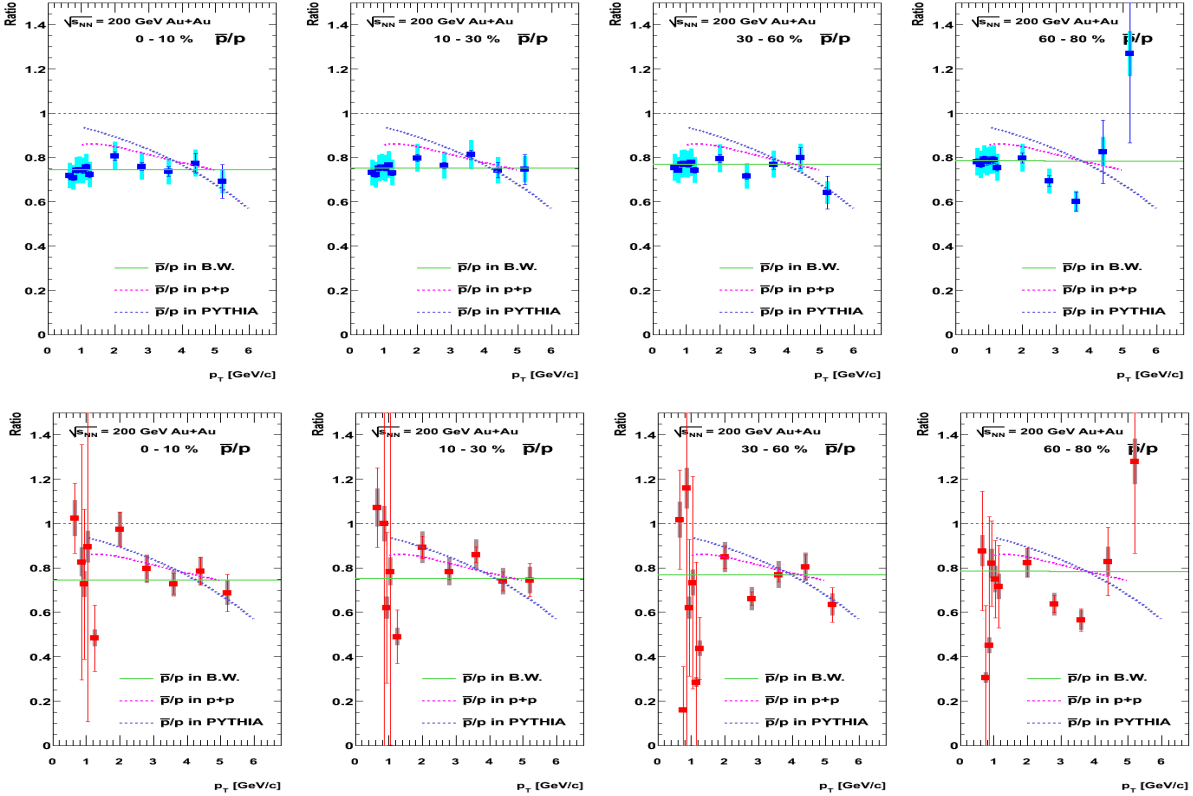


Figure 5.27: \bar{p}/p ratio as a function of p_T in Au+Au collisions at $\sqrt{s_{NN}} = 200$ GeV. Blue points are the data. Red points are the estimated ratio (hard component) (see text).

Soft/Hard Separation in Particle Yield

Figures 5.28 and 5.29 show particle yield dN/dy (soft/hard/sum) divided by $0.5 N_{part}$ as a function of N_{part} for each lower-side p_T cutoff value. Both soft and hard yields are not scaled with N_{part} , i.e. not showing flat N_{part} dependence. Soft yields monotonically increase with N_{part} . Hard yields also increase with N_{part} up to mid-central, but decrease in most central. This decrease is due to jet suppression which is more significant in central collisions. The monotonic increase of summed dN/dy at low p_T with N_{part} is caused just by soft component, not by inclusion of hard component. In right panels ($p_T > 4$ GeV/c), the main contribution for pions is hard component suffered by jet quenching effect, while (anti)protons still show significant soft component in its yield. As we know, it is due to radial flow effect. The larger value of (anti)proton R_{AA} around $p_T = 4$ GeV/c simply comes from radial flow, not absence of jet quenching (see Section 4.5).

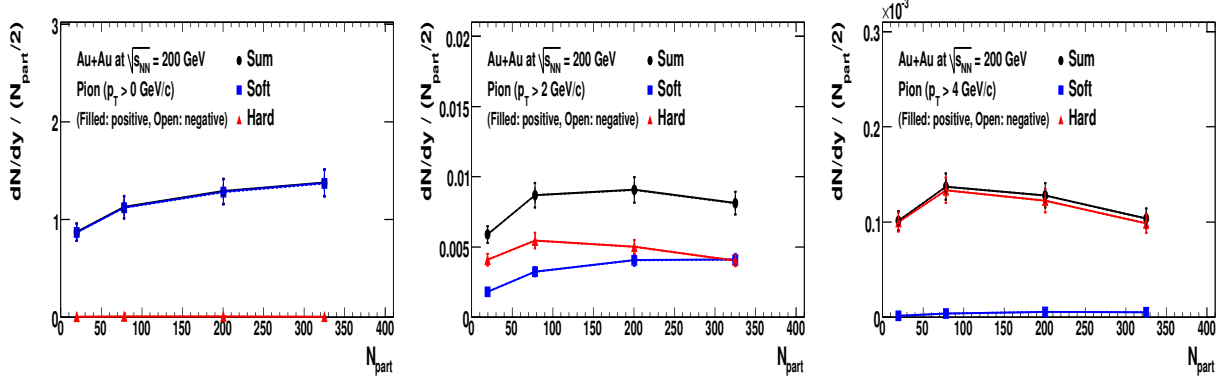


Figure 5.28: Particle yield dN/dy divided by $0.5 N_{part}$ for charged pions as a function of N_{part} in Au+Au collisions at $\sqrt{s_{NN}} = 200$ GeV (p_T cut: 0, 2, 4 GeV/c from left to right).

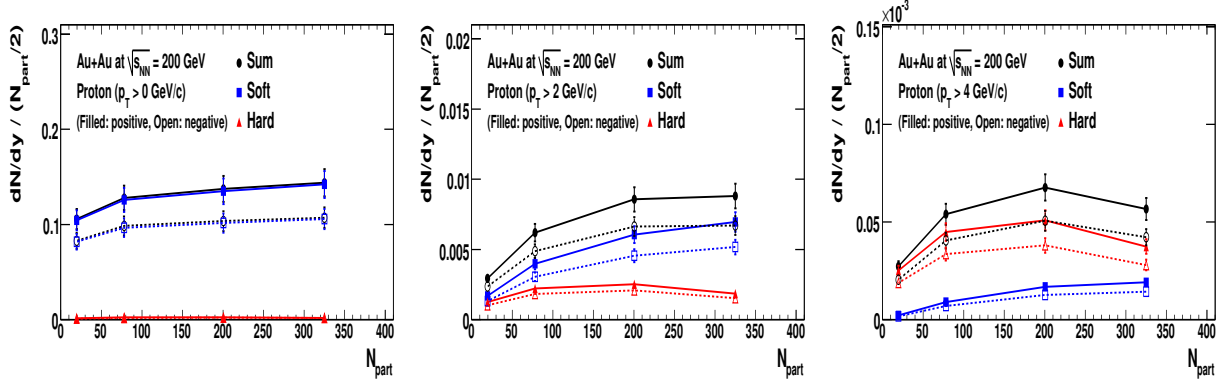


Figure 5.29: Particle yield dN/dy divided by $0.5 N_{part}$ for (anti)protons as a function of N_{part} in Au+Au collisions at $\sqrt{s_{NN}} = 200$ GeV (p_T cut: 0, 2, 4 GeV/c from left to right).

Soft/Hard Separation in Elliptic Flow

Figures 5.30 and 5.31 show v_2 (soft/hard/sum) as a function of p_T for different centralities. v_2 is defined as the second Fourier coefficient of particle emission in azimuthal direction.

$$\frac{dN}{d\phi} = N_0(1 + 2v_2 \cos(2(\phi - \Phi_{RP}))) \quad (5.15)$$

where ϕ is the azimuthal angle of emitted particles, Φ_{RP} is the azimuthal angle of the reaction plane. We think that measured v_2 is the average of soft v_2 and hard v_2 with the corresponding fractions to the total yield.

$$v_2^{sum} = f^{soft}v_2^{soft} + f^{hard}v_2^{hard} \quad (5.16)$$

Soft v_2 (v_2^{soft}) is a purely hydrodynamic contribution, which is now described by blast-wave parameterization [57].

$$v_2 = \frac{\int_0^{2\pi} d\phi \cos(2\phi) I_2(\frac{p_T \sinh \rho}{T_{fo}}) K_1(\frac{m_T \cosh \rho}{T_{fo}})}{\int_0^{2\pi} d\phi I_0(\frac{p_T \sinh \rho}{T_{fo}}) K_1(\frac{m_T \cosh \rho}{T_{fo}})} \quad (5.17)$$

Hard v_2 (v_2^{hard}) is caused by the difference of jet quenching effect between in-plane and out-of-plane (azimuthal dependence of the partonic energy loss). Since we know the fractions of soft and hard components (f^{soft} , f^{hard}) (see Figure and 5.22), we can extract v_2^{hard} from these information. The estimated v_2^{hard} shows a finite value at high p_T as expected.

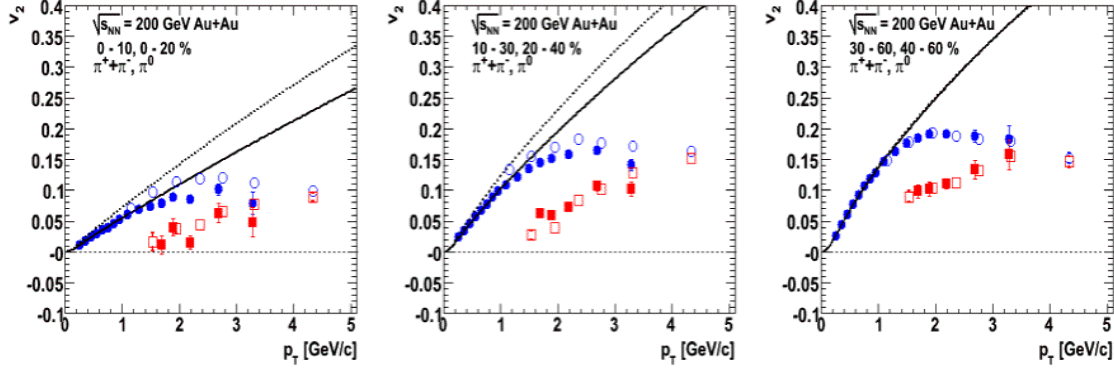


Figure 5.30: v_2 (blue) for $\pi^{+/-}$ (filled), π^0 (open) as a function of p_T in Au+Au collisions at $\sqrt{s_{NN}} = 200$ GeV [58, 59]. The curves are blast-wave fitting results. The red points are estimated hard v_2 .

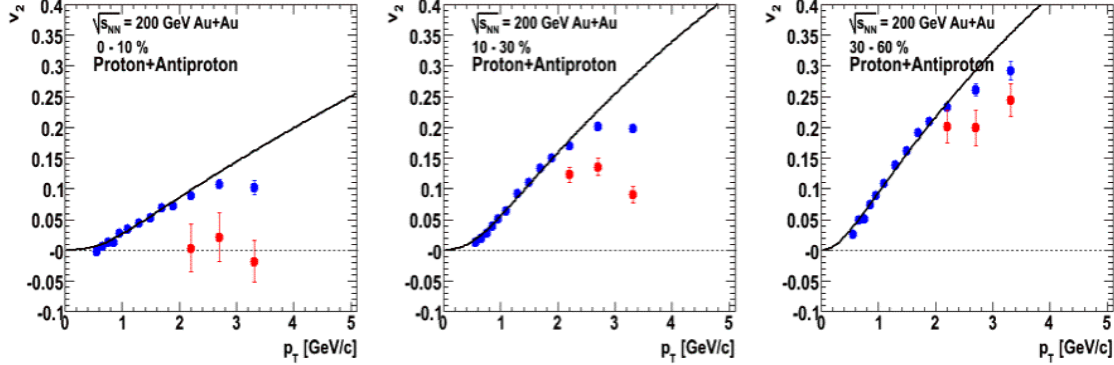


Figure 5.31: v_2 (blue) for p, \bar{p} as a function of p_T in Au+Au collisions at $\sqrt{s_{NN}} = 200$ GeV [59]. The curves are blast-wave fitting results. The red points are estimated hard v_2 .

Summary of Two-component Model

Using a simple two-component model including soft and hard hadron components, we can reproduce the measured p_T spectra for pions and protons, and identify crossover region from soft to hard hadron production at intermediate p_T . We estimate the relative fraction of soft and hard components. Here soft component is thermal emission with collective radial flow. Hard component is jet fragmentation with quenching effect. Soft and hard components become of equal size in this p_T region (2-4 GeV/c). The crossing point depends on collision centrality. It is shifted to higher p_T in more central collisions due to radial flow effect. In terms of soft production, radial flow effect is significant in central Au+Au collisions compared to smaller systems (see Section 5.1.2). This effect pushes heavier particles like protons to higher p_T . The contribution of soft component is comparable to that of hard component even at high p_T ($\lesssim 5$ GeV/c). We think that the baryon enhancement at intermediate p_T can be attributed to radial flow effect.

5.2.3 Quark Recombination Picture

Quark recombination was proposed as one of hadron production mechanisms. The baryon enhancement and the constituent quark number scaling of v_2 at intermediate p_T are explained by quark recombination models. Since the quark number scaling of v_2 is very indicative, quark recombination process is thought to be a possible hadron production mechanism. Recombination of thermal quarks is a usual way which explained by thermal models. In addition to this process, there is another recombination process where one of the recombining quarks originates from jet fragmentation, and the other quark is from thermal source. Hadrons from such recombination are not accounted for in our two-component model.

Theoretical model calculations for p/π ratios [28] are compared to the experimental data in Figure 5.32. These models are similar in that they subscribe to a recombination process of quarks, but they have different implementations. Quark recombination models qualitatively describe the observed ratios at intermediate p_T , but in general underpredict the results at high p_T .

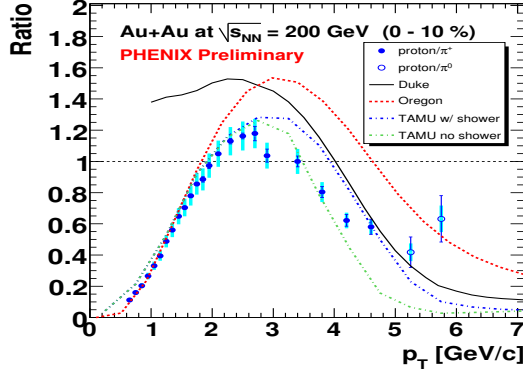


Figure 5.32: p/π^+ ratio in Au+Au collisions at $\sqrt{s_{NN}} = 200$ GeV. Curves show some model predictions [28].

Separation of radial flow between quark and hadronic phases is an important point. In a simple recombination picture, hadronic and partonic radial flow effects cannot be separated. The blast-wave parameterization of radial flow also works for partonic phase. The following equations are a blast-wave parameterization for mesons and baryons [60].

$$\frac{dN_M}{m_T dm_T} \propto \int_0^R r dr m_T I_0\left(\frac{p_T \sinh \rho}{T_{fo}}\right) \times \int \mathcal{D}x_i |\phi_M(x_1, x_2)|^2 K_1\left(\frac{\cosh \rho}{T_{fo}} [\sqrt{m^2 + x_1^2 p_T^2} + \sqrt{m^2 + x_2^2 p_T^2}]\right) \quad (5.18)$$

$$\frac{dN_B}{m_T dm_T} \propto \int_0^R r dr m_T I_0\left(\frac{p_T \sinh \rho}{T_{fo}}\right) \times \int \mathcal{D}x_i |\phi_B(x_1, x_2, x_3)|^2 K_1\left(\frac{\cosh \rho}{T_{fo}} [\sqrt{m^2 + x_1^2 p_T^2} + \sqrt{m^2 + x_2^2 p_T^2} + \sqrt{m^2 + x_3^2 p_T^2}]\right) \quad (5.19)$$

Indeed, if we take x_i (momentum fraction of quark i) with equal weight, these equations are consistent with Equation 5.2.

As mentioned in Section 5.1.2, there is the difference of temperatures of chemical and kinetic freeze-outs. This is an evidence for further expansion at hadronic phase. Even if quark phase is created before hadronization, final-state hadronic scattering should be taken into account.

5.2.4 Jet Fragmentation and Jet Quenching

At high p_T , even if partons propagating through the medium have a large energy loss, the leading parton is expected to punch out of the medium before fragmentation. Thus, we expect: (1) same suppression factor for different hadrons, because a parton losing energy does not know the type of hadrons which will be eventually created, and (2) particle ratios of hadrons above some p_T threshold to be universal. (Fragmentation functions are independent of the process. If jet fragmentation occurs in the medium, there may be some modification of the fragmentation functions.) When we compare hard component to expectation from p+p spectra or pQCD calculations, soft component such as hydrodynamic contribution should be subtracted as performed in Section 5.2.2.

A fundamental question for the jet quenching mechanism is whether there is a difference between gluon jets and quark jets. Since gluons in QCD have stronger interaction than quarks, larger energy loss of gluon jets is expected than that of quark jets. Identified hadrons at high p_T provide a sensitivity to the difference between quark and gluon fragmentation. Proton and pion production at high p_T is expected to have significant contributions from quark fragmentation while antiprotons are mostly from gluon fragmentation [61]. Therefore, \bar{p}/p and \bar{p}/π ratios are sensitive to the possible color charge dependence of energy loss. Figure 5.34 shows the fraction of quark and gluon jets in p+p jet events. This is estimated by PYTHIA (LO-pQCD based event generator, version 6) calculation [62]. We notice that quark jet is dominant at high p_T than gluon jet. At 62.4 GeV, the quark-jet dominant region is lower than at 200 GeV. By changing collision energy $\sqrt{s_{NN}}$, we expect to see the difference of quark and gluon jet contribution at the same p_T .

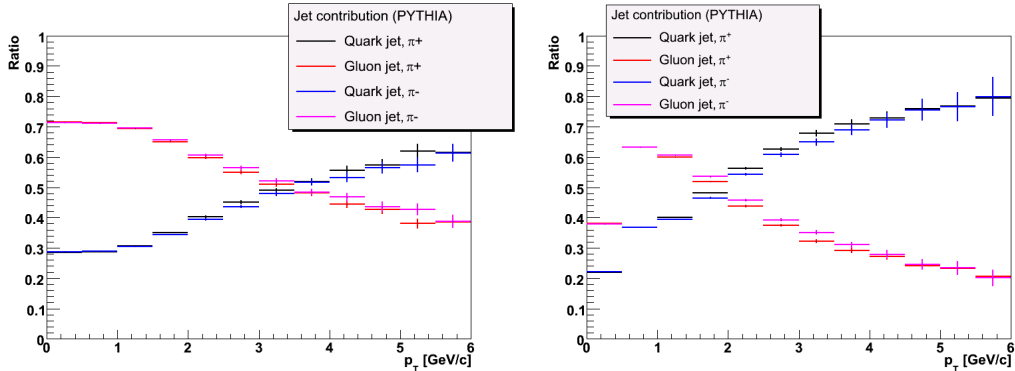


Figure 5.33: Quark and gluon jet contributions for pions as a function of p_T in PYTHIA p+p jet events at $\sqrt{s_{NN}} = 200$ GeV (left) and 62.4 GeV (right).

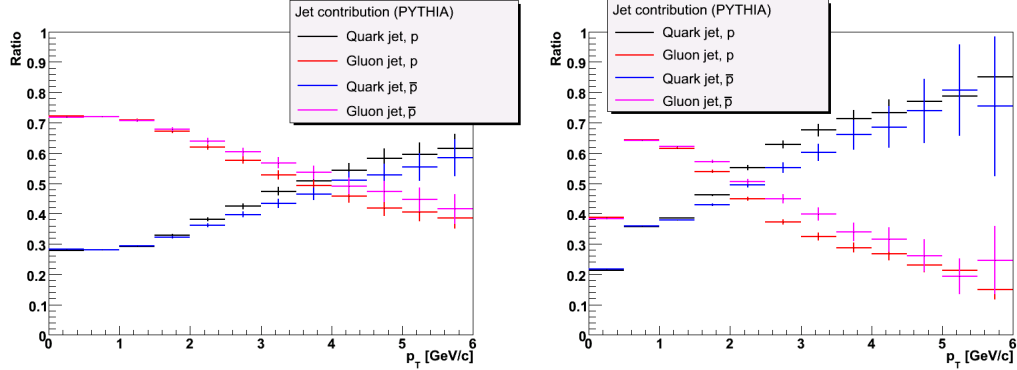


Figure 5.34: Quark and gluon jet contributions for (anti)protons as a function of p_T in PYTHIA p+p jet events at $\sqrt{s_{NN}} = 200$ GeV (left) and 62.4 GeV (right).

p/π^+ and \bar{p}/π^- ratios from PYTHIA are almost constant at high p_T (see Figures 5.35 and 5.36). As shown in Figure 5.13, p/π (\bar{p}/π) ratios in central Au+Au/Cu+Cu collisions at $\sqrt{s_{NN}} = 200$ GeV approach the values in p+p collisions at high $p_T \gtrsim 5$ GeV/c. And R_{CP} shows similar suppression for pions and (anti)protons (see Section 4.5.2), though they have different sensitivities to quark and gluon jets. The results indicate that hard-scattered partons (quarks and gluons) have similar energy loss when traversing the nuclear medium, and parton fragmentation function does not change.

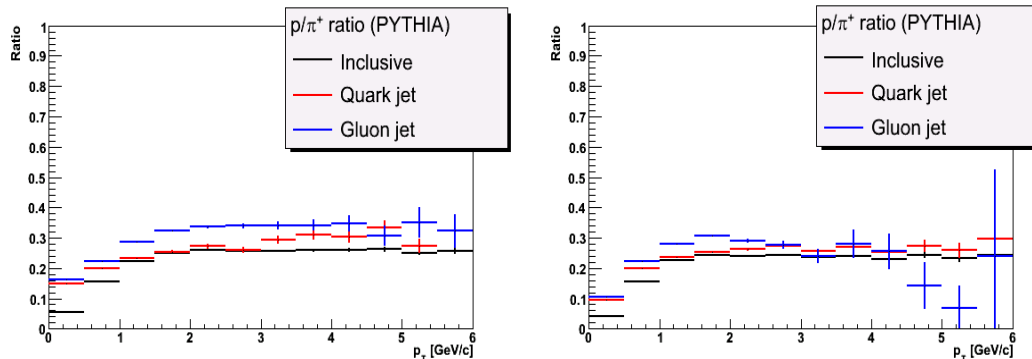


Figure 5.35: p/π^+ ratio as a function of p_T in PYTHIA p+p collisions at $\sqrt{s_{NN}} = 200$ GeV (left) and 62.4 GeV (right).

In quark fragmentation, a leading hadron is more likely to be a particle rather than an anti-particle, and there is no such preference in gluon jet. A decrease of \bar{p}/p ratio with p_T would then indicate a significant quark jet contribution to the baryon production. A pQCD-based calculation shows a significant effect from energy loss on \bar{p}/p ratio due to the large energy loss of gluons in the medium [61]. In contrast, the measured ratio does not show such a clear decreasing trend (see Figure 5.37 (left)). The \bar{p}/p ratios show almost flat p_T dependence and are independent of

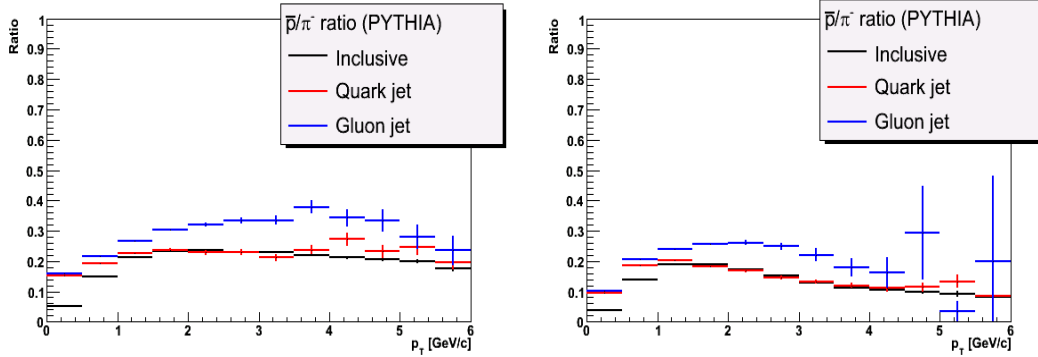


Figure 5.36: \bar{p}/π^- ratio as a function of p_T in PYTHIA p+p collisions at $\sqrt{s_{NN}} = 200$ GeV (left) and 62.4 GeV (right).

centrality at $\sqrt{s_{NN}} = 200$ GeV (see Section 4.4.3). The soft component would lead to a lower \bar{p}/p ratio for peripheral Au+Au relative to central Au+Au since radial flow strength is lower in peripheral. However such a centrality dependence is not observed.

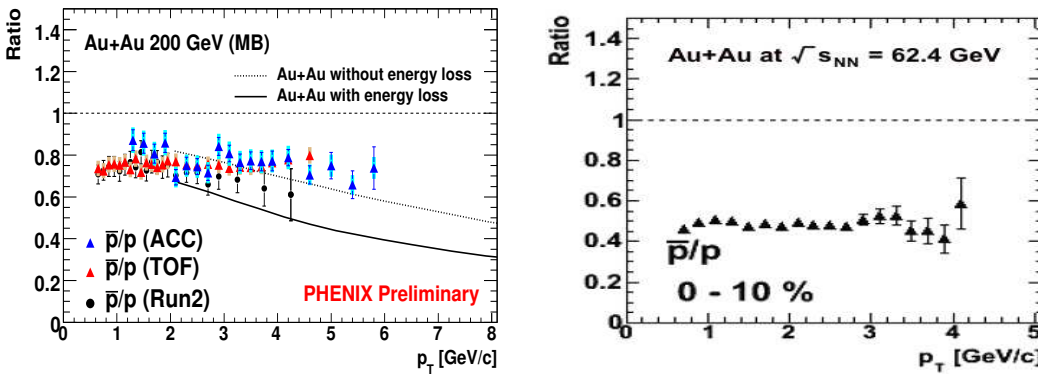


Figure 5.37: Left: \bar{p}/p ratio as a function of p_T in minimum bias Au+Au collisions at $\sqrt{s_{NN}} = 200$ GeV. Curves are the predictions from a jet quenching model [61]. Right: \bar{p}/p ratio as a function of p_T in Au+Au collisions at $\sqrt{s_{NN}} = 62.4$ GeV.

The decreasing trend in \bar{p}/p ratio is expected to be observed at $\sqrt{s_{NN}} = 62.4$ GeV. It is known from lower beam energies, where quark fragmentation is more dominant, that the \bar{p}/π and \bar{p}/p ratios are very small [63]. As shown in Figure 5.38 (data) and 5.39 (PYTHIA), the flat \bar{p}/p ratio of ~ 0.6 in 62.4 GeV p+p collisions is likely dominated by gluon fragmentation. The 62.4 GeV Au+Au data also shows flat p_T dependence in \bar{p}/p (see Figure 5.37 (right)). If we obtain enough statistics, we will confirm whether particle ratios are the same between Au+Au and p+p at high p_T .

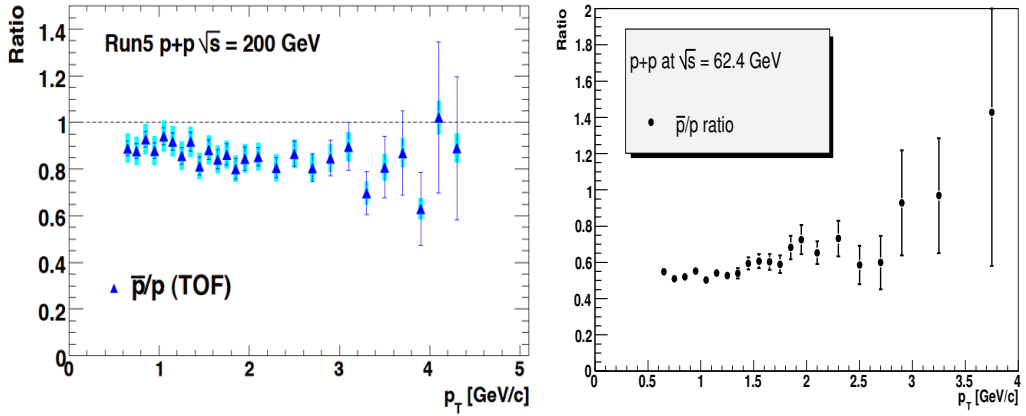


Figure 5.38: Left: \bar{p}/p ratio as a function of p_T in minimum bias p+p collisions at $\sqrt{s} = 200$ GeV. Blue band is systematic errors. Right: \bar{p}/p ratio as a function of p_T in minimum bias p+p collisions at $\sqrt{s} = 62.4$ GeV.

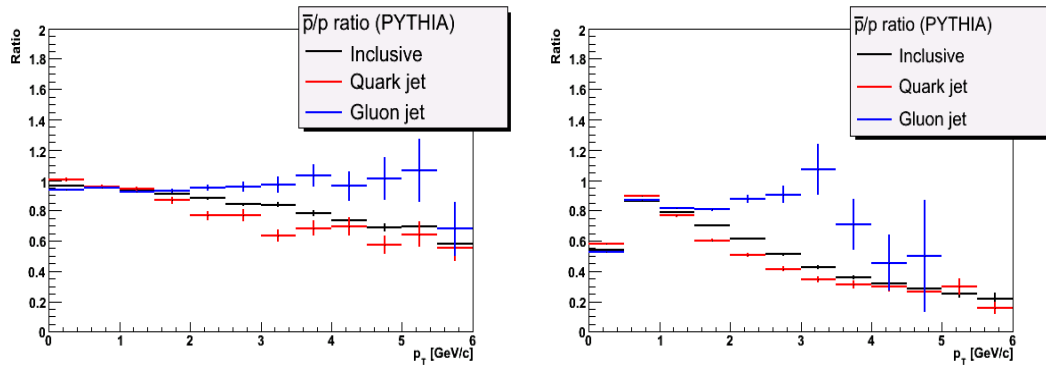


Figure 5.39: \bar{p}/p ratio as a function of p_T in PYTHIA p+p collisions at $\sqrt{s_{NN}} = 200$ GeV (left) and 62.4 GeV (right).

Chapter 6

Conclusions

We have performed a systematic study of proton and antiproton spectra in Au+Au, Cu+Cu, p+p collisions at $\sqrt{s_{NN}} = 62.4/200$ GeV. The data set taken in the PHENIX experiment allows us to study energy dependence and system size dependence of the baryon enhancement in relativistic heavy ion collisions. We present identified charged hadron p_T spectra ($\pi/K/p$ and their antiparticles), particle ratios, nuclear modification factors, chemical/kinetic freeze-out properties and their scaling properties between different collision systems. The spectra are measured at mid-rapidity ($|\eta| < 0.35$) over the range of $0.5 < p_T < 6$ GeV/c with particle identification by time-of-flight and threshold-type Cherenkov light emission methods. The p_T range of charged hadron identification has been extended by the high statistics data. Also the particle identification capability at high p_T has been enhanced by introducing an Aerogel Cherenkov counter in PHENIX. The identified hadron production can be studied up to 5 GeV/c for charged pions, and 7 GeV/c for (anti)protons.

In all collision systems (Au+Au, Cu+Cu), we confirm the baryon enhancement at intermediate p_T (2-5 GeV/c). In terms of binary collision scaling, protons and antiprotons are enhanced, while pions are suppressed at intermediate p_T . We observe a turnover of p/π ratios at $p_T = 2\text{-}3$ GeV/c, indicating a transition from soft to hard hadron production. We find that the baryon enhancement and freeze-out properties (freeze-out temperature, transverse flow velocity) are scaled with the number of participant nucleons N_{part} , which is corresponding to the system volume, between Au+Au and Cu+Cu collisions at the same collision energy $\sqrt{s_{NN}} = 200/62.4$ GeV even though the overlapped collision zone has a different shape. The system volume is a control parameter. Comparing to the 200 GeV data, the 62.4 GeV data shows a slightly larger proton contribution at intermediate p_T , while there is a less antiproton contribution. At lower energy 62.4 GeV, proton production seems to be more affected by baryon number transport process. Therefore antiproton would be a good indicator of the baryon enhancement. Instead of N_{part} scaling, transverse energy density $dE_T/d\eta$ scaling of \bar{p}/π^- is also workable between different collision energies.

Using a simple two-component model including soft and hard hadron components, we can reproduce the measured p_T spectra for pions and protons, and identify crossover region from soft to hard hadron production at intermediate p_T . We estimate the relative fraction of soft and hard components. Here soft component is thermal emission with collective radial flow. Hard component is jet fragmentation with quenching effect. Soft and hard components become of equal size in this p_T region (2-4 GeV/c). The crossing point depends on collision centrality. It is shifted to higher p_T in more central collisions due to radial flow effect. In terms of soft production, radial flow effect is significant in central Au+Au collisions compared to smaller systems. This effect pushes heavier particles like protons to higher p_T . The contribution of soft component is comparable to that of hard component even at high p_T ($\lesssim 5$ GeV/c). We think that the baryon enhancement at intermediate p_T can be attributed to radial flow effect. This is thought to be one of unique properties of hadron production in relativistic heavy ion collisions. The next question is what the relation of hadronic and partonic radial flow is. The difference of freeze-out temperatures between chemical and kinetic freeze-out's shows a finite lifetime of hadronic stage.

We also discuss the relation between this radial flow picture and quark recombination picture. In a simple recombination picture, hadronic and partonic radial flow effects cannot be separated. Since the constituent quark number scaling of elliptic flow v_2 is very indicative, quark recombination process is thought to be a possible hadron production mechanism.

At high $p_T \gtrsim 5$ GeV/c, p/π (\bar{p}/π) ratios in central Au+Au collisions approach the values in p+p collisions. And R_{CP} shows similar suppression for pions and (anti)protons, though they have different sensitivities to quark and gluon jets. The results indicate that hard-scattered partons (quarks and gluons) have similar energy loss when traversing the nuclear medium, and parton fragmentation function does not change.

Appendix A

Kinematic Variables

Here, we introduce kinematic variables used in the thesis. For a particle which has the momentum $\mathbf{p} = (p_x, p_y, p_z)$ and mass m , we define the following variables. The beam line is taken as z-axis. Transverse momentum p_T and transverse mass m_T and total energy E are:

$$p_T = \sqrt{p_x^2 + p_y^2}, \quad m_T = \sqrt{p_T^2 + m^2}, \quad E = \sqrt{\mathbf{p}^2 + m^2}. \quad (\text{A.1})$$

Rapidity y is:

$$y = \frac{1}{2} \ln \frac{E + p_z}{E - p_z}. \quad (\text{A.2})$$

The rapidity y is invariant under Lorentz transformation. In the relativistic limit ($p \gg m$), pseudo-rapidity η is equivalent to y :

$$\eta = -\ln(\tan(\frac{\theta}{2})) \sim y. \quad (\text{A.3})$$

Differential particle yield is described with Lorentz invariant yield:

$$E \frac{d^3N}{dp^3} = E \frac{1}{2\pi p_T} \frac{d^2N}{dp_T dp_z} = \frac{1}{2\pi p_T} \frac{d^2N}{dp_T dy} \quad (\text{A.4})$$

where N is the number of counted particles per event. Particle yield dN/dy is the integrated one over p_T .

Bibliography

- [1] C. Bernard et al., Phys. Rev. D 71 (2005) 034504.
- [2] Fodor Z et al., J. High Energy Phys. JHEP04 (2004) 050.
- [3] Allton C R et al., Phys. Rev. D 66 (2002) 074507.
- [4] Cleymans J et al., Phys. Rev. C 60 (1999) 054908.
- [5] Braun-Munzinger P et al., J. Phys. G: Nucl. Part. Phys. 28 (2002) 1971.
- [6] Karsch F et al., Phys. Lett. B 478 (2000) 447.
- [7] Nagamiya S, Nucl. Phys. A 488 (1988) 3c-30c.
- [8] BRAHMS Collaboration, Phys. Rev. Lett. 93 (2004) 102301.
- [9] PHOBOS Collaboration, Phys. Rev. Lett. 91 (2003) 052303.
- [10] J.D. Bjorken, Phys. Rev. D 27 (1983) 140.
- [11] PHENIX Collaboration, Nucl. Phys. A 757 (2005) 184.
- [12] PHENIX Collaboration, Phys. Rev. C 71 (2005) 034908.
- [13] PHENIX Collaboration, Phys. Rev. C 75 (2007) 024909.
- [14] STAR Collaboration, Phys. Rev. Lett. 91 (2003) 072304.
- [15] PHENIX Collaboration, Phys. Rev. Lett. 91 (2003) 072303.
- [16] STAR Collaboration, J. Phys. G 30 (2004) S963-S968.
- [17] PHENIX Collaboration, Phys. Lett. B 649 (2007) 359-369.
- [18] M. Kaneta et al. nucl-th/0405068.
- [19] PHENIX Collaboration, Phys. Rev. C 69 (2004) 034909.
- [20] S. Sakai, PhD thesis (University of Tsukuba, 2007).

- [21] PHENIX Collaboration, Phys. Rev. Lett. 91 (2003) 182301.
- [22] PHENIX Collaboration, Phys. Rev. Lett. 98 (2007) 162301.
- [23] PHENIX Collaboration, Phys. Rev. C 69 (2004) 034910; PHENIX Collaboration, Phys. Rev. Lett. 91 (2003) 072301; PHENIX Collaboration, Phys. Rev. C 69 (2004) 034909.
- [24] STAR Collaboration, Phys. Rev. Lett. 92 (2004) 052302.
- [25] PHENIX Collaboration, Phys. Rev. Lett. 91 (2003) 072303.
- [26] PHENIX Collaboration, Phys. Rev. C 74 (2006) 024904.
- [27] T. Hirano et al., Phys. Rev. C 69 (2004) 034908; P.F. Kolb et al., Quark gluon plasma (nucl-th/0305084); P. Huovinen, Quark gluon plasma (nucl-th/0305064).
- [28] R.J. Fries et al., Phys. Rev. C 68 (2003) 044902; R.C. Hwa et al., Phys. Rev. C 70 (2004) 024905; V. Greco et al., Phys. Rev. C 68 (2003) 034904.
- [29] I. Vitev et al., Phys. Rev. C 65 (2002) 041902; S.E. Vance et al., Phys. Lett. B 443 (1998) 45.
- [30] T. Falter et al., Phys. Lett. B 594 (2004) 61.
- [31] M. Harrison et al., Nucl. Instrum. Methods A 499 (2003) 235.
- [32] <http://www.agssrhichome.bnl.gov/RHIC/Runs/>.
- [33] C. Adler et al., Nucl. Instrum. Methods A 470 (2001) 488.
- [34] PHENIX internal analysis notes : 286, 383, 384, 469.
- [35] NA49 Collaboration, Eur. Phys. J. C 2 (1998) 383.
- [36] PHENIX internal analysis notes : 290, 387, 395.
- [37] PHENIX internal analysis note : 187.
- [38] PHENIX internal analysis note : 119.
- [39] PHENIX internal analysis note : 469.
- [40] STAR Collaboration, Phys. Rev. C 75, (2007) 064901.
- [41] STAR Collaboration, Phys. Rev. Lett. 92 (2004) 052302.
- [42] STAR Collaboration, Phys. Lett. B 612 (2005) 181, Phys. Rev. C 71 (2005) 064902.

- [43] Stachel J, Nucl. Phys. A 654 (1999) 119c; Heinz U et al., Nucl. Phys. A 702 (2002) 269c; Braun-Munzinger P et al., Phys. Lett. B 518 (2001) 41.
- [44] J. Sollfrank et al., Phys. Rev. C 59 (1999) 1637; N. Xu et al., Nucl. Phys. A 698 (2002) 306c.
- [45] J. Schaffner-Bielich et al., Nucl. Phys. A 705 (2002) 494.
- [46] P.J. Siemens et al., Phys. Rev. Lett. 42 (1979) 880.
- [47] F. Cooper et al., Phys. Rev. D 10 (1974) 186.
- [48] E. Schnedermann et al., Phys. Rev. C 48 (1993) 2462.
- [49] A. Kiyomichi, PhD thesis (University of Tsukuba, 2005).
- [50] A. Enokizono, Quark Matter 2006 presentation (2006).
- [51] PHOBOS Collaboration, Nucl. Phys. A 774 (2006) 523.
- [52] B. Alper et al., Nucl. Phys. B 100 (1975) 237.
- [53] P. Abreu et al., Eur. Phys. J. C 17 (2000) 207.
- [54] V. Greco et al., Phys. Rev. C 71 (2005) 041901.
- [55] D. Cline et al., Phys. Rev. Lett. 27 (1971) 71; W. Bruckner et al., Z. Phys. A - Atomic Nuclei 335 (1990) 217.
- [56] T. Hirano et al., Phys. Rev. C 69 (2004) 034908.
- [57] P. Huovinen et al., Phys. Lett. B 503 (2001) 58.
- [58] K. Miki, PHENIX preliminary data.
- [59] H. Masui, PHENIX preliminary data, PhD thesis (University of Tsukuba, 2007).
- [60] R.J. Fries et al., Phys. Rev. C 68 (2003) 044902.
- [61] X.N. Wang, Phys. Rev. C 58 (1998) 2321; I. Vitev et al., Nucl. Phys. A 715 (2003) 779.
- [62] T. Sjostrand et al., <http://www.hep.lu.se/~torbjorn/Pythia.html>.
- [63] P.B. Straub et al., Phys. Rev. D 45 (1992) 3030.